Analysis of Rainfall Induced Slope Disaster and Development of Early Warning System based on IoT

劉, 炎

https://hdl.handle.net/2324/5068203

出版情報：Kyushu University, 2022, 博士（工学）, 課程博士
バージョン：
権利関係：

Analysis of Rainfall Induced Slope Disaster and Development of Early Warning System based on IoT

Liu Yan

July 2022

Dedicated to my parents and wife

Analysis of Rainfall Induced Slope Disaster and Development of Early Warning System based on IoT

A Dissertation Submitted
In Partial Fulfillment of the Requirements
For the Degree of
Doctor of Engineering

By

Yan Liu

Graduate School of Engineering, Kyushu University, Fukuoka, Japan

July, 2022

DEPARTMENT OF CIVIL AND STRUCTURAL ENGINEERING

GRADUATE SCHOOL OF ENGINEERING

KYUSHU UNIVERSITY

Fukuoka, Japan

CERTIFICATE

The undersigned hereby certify that they have read and recommended to the Graduate School of Engineering for the acceptance of this thesis entitled, " ***Analysis of Rainfall Induced Slope Disaster and Development of Early Warning System based on IoT***" by **Yan Liu** in partial fulfillment of the requirements for the degree of **Doctor of Engineering.**

Dated: July, 2022

Thesis Supervisor:

Prof. Hemanta Hazarika, Dr. Eng

Examining Committee:

Prof. Yasuhiro Mitani

Prof. Haruichi Kanaya

Prof. Yasuhide Fukumoto

ABSTRACT

With changing global weather conditions, the occurrences of unpredictable heavy rainfall have increased, and with them, rainfall-induced landslide disasters have become more common. It was reported the number of rainfall-induced landslides in Japan has increased by 50% compared to the last 10 years. Rainfall-induced landslides pose a huge threat to lives and properties, therefore, many researchers have been devoted to analyzing the stability of slopes and mitigating such disaster problems. By comparing different methods, such as hard type, numerical simulation, and monitoring methods, it was found that the application of Early Warning System (EWS) based on real-time data and slope stability assessment is a practical approach to mitigating such disasters. In analyzing slope stability, existing studies ignore potential deep and shallow slope failure modes induced by continuous rainfall. In developing EWS, research has found that the current EWS is high cost, not sustainable and lacks an open architecture for development and modification by authorities at the local level.

To reveal the slope failure mechanism and assess the stability of the slope under continuous rainfall, the factor of safety (F_s) under different soil parameters and rainfall infiltration conditions was determined considering both shallow and deep failure modes.

In order to develop a practical EWS considering SDGs, a low-cost and sustainable EWS is presented that integrates the Internet of Things (IoT) and a solar-powered integrated platform for data collection, transmission and analysis. A series of model tests were conducted to check the feasibility of the EWS and research proposed effective evaluation indices from various precursor phenomena of slope failure based on motion analysis and interpolation analysis.

For the stability analysis of the slope, Transient Rainfall Infiltration and Grid-Based Regional Slope-Stability (TRIGRS) model was used to analyze the shallow slope failure and upper bound analysis was used to obtain the critical safety state of deep slope failure mode. For the development of EWS, all the sensors used in this system, such as soil moisture sensor, pore water pressure sensor and 9-axis accelerometer, are low cost and portable. Based on the principle of rainwater infiltration and movement of soil particles, important warning indices were established in the system. Three stages were proposed to give landslide risk classification. For the model test, this study considered two influencing parameters: initial moisture content and rainfall intensity. This research revealed the infiltration process of the sandy slope, recorded the soil movement by motion analysis, and extended the limited experimental data to a global analysis by interpolation methods.

The main contributions of each chapter in the dissertation are as follows:

Chapter 1 presents the background, methodology, objective, and original contributions of this study. It highlights the threat that rainfall-related disasters pose to the social economy and the lives of residents. It compares current approaches to disaster mitigation and suggests that EWS is an effective and appropriate approach. This chapter presents the improvement points of current IoT-based EWS and highlights the important role they play in disaster mitigation.

Chapter 2 reveals the potential forms of slope failure under rainfall conditions. For shallow failure conditions, TRIGRS model was used for stability analysis. For deep failure mode, upper bound limit analysis was used. A series of illustrations presented the Fs of slope under different soil parameters and rainwater infiltration conditions. The results imply that F_s decreases significantly due to the influence of rainfall infiltration, while the effect of suction in an unsaturated state can improve the stability. Furthermore, the safety assessment results can be used as important indicators for early warning work.

Chapter 3 presents the composition of the EWS in detail, including the software aspects for receiving, transmitting, and processing data. The hardware aspect includes sensors, communication devices, Wi-Fi router, and solar battery system etc. This chapter also presents the monitoring process, risk determination, and timing of signal transmission. This part of the thesis forms the basis for experimental verification and field application.

Chapter 4 presents the performance of the EWS during model tests. It presents the test conditions, sensor arrangement, and model test setup. It shows in detail the development trend of soil moisture content, pore water pressure, deflection angle, and real-time F_s in each test. It defines key warning indices and divides the risk levels according to the principle of the EWS. The proposed landslide risk classification divides the whole process into three stages: Initial Monitoring State, Alert State, and Triggering State to issue alerts at various stages. The accurate testing results conducted on sandy slopes enable us to identify the risk stages, send warning signals, and predict potential movements to send early warnings so that people near the danger zones have enough time to escape and isolate the area.

Chapter 5 provides the study of the experimental data from the motion analysis and interpolation method. Two groups with different rainfall intensities and initial moisture contents were considered. The motion analysis is based on computer vision-based monitoring technology, which can track extremely small displacement, particle trajectories and velocity. Results provided an indication of the potential trajectory and movement characteristics when a landslide occurs in reality. The interpolation method was used to predict the intermediate data for training the EWS model for a wide range of meteorological conditions. It also helps predict the sensor data for blind areas where sensors could not be placed. Accurate interpolation results can help the EWS provide potential risk levels for larger areas and more rainfall conditions.

Chapter 6 summarizes all the contributions and results of this research. In this chapter, the possibility of further development of EWS with more functions and application scenarios is presented. It also proposed that IoT and edge AI can be coupled so that the whole process can achieve the goals of full automation. The application of Low Power Wide Area (LWPA) in EWS was introduced and some sites were considered for EWS deployment in the future.

ACKNOWLEDGMENTS

I remember opening my eyes one morning last year and asking myself that it's been two years in Japan, and what I've contributed. After thinking for a while, I asked myself a second question: how could I conduct research so that it has some positive effects on the world. In the following year, I have been centered on this lofty but practical goal, trying to avoid a disaster, save a life and even reduce some economic losses. Regrettably, I only did some tiny work. But I am lucky enough to get the support and assistance from many professors, researchers and engineering experts. Without their assistance, it’s completely impossible to finish this thesis.

First of all, I would like to express my sincere gratitude to my supervisor Prof. Hemanta Hazarika, who provides me a chance to study at Kyushu University, supports my research, and he always spares no effort to help me solve the problem and gives me enough resources to complete my research. In addition, he also tries to educate me on the right working attitude, thinking approaches and personal qualities. Without him, this thesis would not exist.

I would like to be indebted to Prof. Haruichi Kanaya (Kyushu University) for his great assistance in my research. He participates in the whole process of EWS development and teaches me a lot regarding the connection of sensors, the selection of solar battery systems and basic knowledge of the Internet of Things. In addition, he also gives important comments on this thesis.

I would like to give my great thanks to Prof. Yasuhiro Mitani (Kyushu University) for his important suggestions on the framework of this thesis and the presentation of my defense. I also give my sincere thanks to Prof. Yasuhide Fukumoto (Kyushu University) for his efforts in reviewing my thesis and providing meaningful suggestions.

I also want to thank Mr. Osamu Takiguchi (ALSENS Inc) for his help in EWS improvement and thank associate professor Kazuaki Tanaka (Kyushu Institute of

Technology) and Mr. Keisuke Yamashita (CMN Co. Ltd) for their great efforts in LPWA application.

I would like to give my sincere gratitude to Prof. Yasuhide Fukumoto (Kyushu University) and Dr. Nguyen Thi Hoai Linh (Kyushu University) for their huge support of the interpolation analysis. I also want to thank Dr. Masanori Murai (Shimizu Corporation) for his help in EWS deployment and Dr. Yoshifumi Kochi (K’s Lab) for help in the geological investigation.

I would like to show my appreciation to our secretary Mike Murayama who helps me deal with lots of complicated affairs in these years, and all members of Prof. Hazarika lab (especially Dr. Divyesh Rohit), all the collaborators of my research.

In addition, thanks to my master supervisor Dr. Yi He (Southwest Jiaotong University) for the selfless guidance and Sichuan Science and Technology Program (Grant No. 2021YFS0320) by Prof. Hazarika and Southwest Jiaotong University: Seismic instability mechanism and stability evaluation of soil rock mixture slope in deep canyon area on the southeast edge of Qinghai Tibet Plateau.

I would like to give my deepest sincere gratitude to the scholarship CSC.

I would like to be grateful to my parents for their love, encouragement and sacrifice.

I would like to thank the three years of living in Japan, which improved my reflections on life and led me to be broad and liberal enough.

Finally, I would like to owe a debt to my wife Zhang Cheng, for her three years of company, encouragement and great dedication.

TABLES OF CONTENTS

LIST OF FIGURES

LIST OF TABLES

NOMENCLATURE

β	Angle of slope
φ'	Effective Soil friction angle
c'	Effective cohesion
c_{app}	Apparent cohesion caused by negative porewater pressure
γ	Soil unit weight,
γ_w	Unit weight of groundwater,
w	Soil moisture content
u_a	Pore air pressure,
u_w	Pore water pressure
q	Vertical specific discharge
k_s	Saturated hydraulic conductivity
r_{u}	Coefficient of pore water pressure
ω	Rotational angular acceleration
D_s	Energy dissipation with effects of matric suction
D_c	Energy dissipation without porewater pressure
W_{r}	Rate of external work by soil weight component
W_{uw}	External work by pore water pressure component
Z_{w}	Depth from the wetting front to the ground
H	Slope height
a	Inverse of the air entry pressure
n	Pore size distribution
k_{s}	Saturated hydraulic conductivity
$\Delta\varphi$	Variation in friction angle
D_{50}	Mean grain size
U_{c}	Uniformity coefficient
Gs	Specific gravity
e	Void ratio
$\rho_{\max}$	Max dry density
$\rho_{\min}$	Min dry density
W_L	Liquid limit

W_p	Plastic limit

ABBREVIATIONS

EWS	Early Warning System
IoT	Internet of Thing
LPWA	Low Power Wide Area
FEM	Finite Element Method
SPH	Smoothed-Particle Hydrodynamic
DDA	Discontinuous Deformation Analysis
HBP	Herschel-Bulkley-Papanastasiou
SWCC	Soil Water Characteristic Curve
PIV	Particle Image Velocimetry
F_s	Factor of Safety
GIS	Geographic information system
GNSS	Global Navigation Satellite System
I-D	Intensity- Duration
MEMS	Microelectromechanical systems
NB-IoT	Narrowband IoT
LTE	Long-Term Evolution
S1,S2,S3,S4,S5,S6	Soil moisture sensor 1-6
M1,M2,M3,M4	9-axis acceleration sensor 1-4
P1,P2,P3	Porewater pressure sensor 1-3
AMeDAS	Automated Meteorological Data Acquisition System
DNN	Deep Neural Network
FL	Federated Learning
N_s	Stability factor
TRIGRS	Transient Rainfall Infiltration and Grid-Based Regional Slope-Stability

CHAPTER 1

1. INTRODUCTION

1.1 Background of the study

Currently, with changing global weather conditions, the occurrences of unpredictable and unprecedented heavy rainfall have increased, and rainfall-induced landslide disasters have also become frequent. **Fig 1.1** shows that there were around 4000 rainfall-induced landslides occurred from 2004 to 2016 and Asia accounts for 75% of global rainfall-induced landslides, and East Asia is the most affected area (Froude and Petley, 2018). Japan is located in the East Asian monsoon region, with mountainous landforms and extremely complex geological conditions, which makes it extremely prone to landslide disasters. In recent years, Japan is suffering a growing risk of natural disasters due to frequent rainfall, which occurs almost every year during the rainy and typhoon seasons. Landslide, debris flow and slope failure are the most widespread geological hazards that pose significant threats to human lives and properties. According to a 2020 Japanese government report (Reported by Ministry of Land, Infrastructure, Transport and Tourism, Japan, 2020), there is a 50% rise in landslide disasters compared to the previous 10 years and it was estimated that the number of days with daily rainfall exceeding 200mm in the future will double compared to the current situation. **Table 1.1** shows the typical sediment disasters in Japan in the past decade. It can be seen clearly that many people lost their lives or still missing in rainfall-induced disasters. As **Fig 1.1**

(c) and **Table 1.1** show, Kyushu Island has always been the most severely affected area by rainfall and it caused heavy rainfall disasters almost every year. For example in **Fig 1.2**, during Northern Kyushu Torrential Rainfall Disaster in July 2017, localized and torrential rainfall caused massive landslides, debris flows, and flooding of rivers, resulting in devastating damage to a lot of areas of Fukuoka and Oita prefectures of Kyushu, Japan (Hazarika et al. 2020). The disaster caused 34 people dead including 4 people still missing. Another extreme rainfall event occurred in the Kyushu region in 2020, it caused 82 people died and 4 people missing, which is even more serious than the disaster in 2017. **Fig 1.2** shows the real shots of the scene after two heavy rainfall. It can be clearly seen that the rainfall has caused huge disasters.

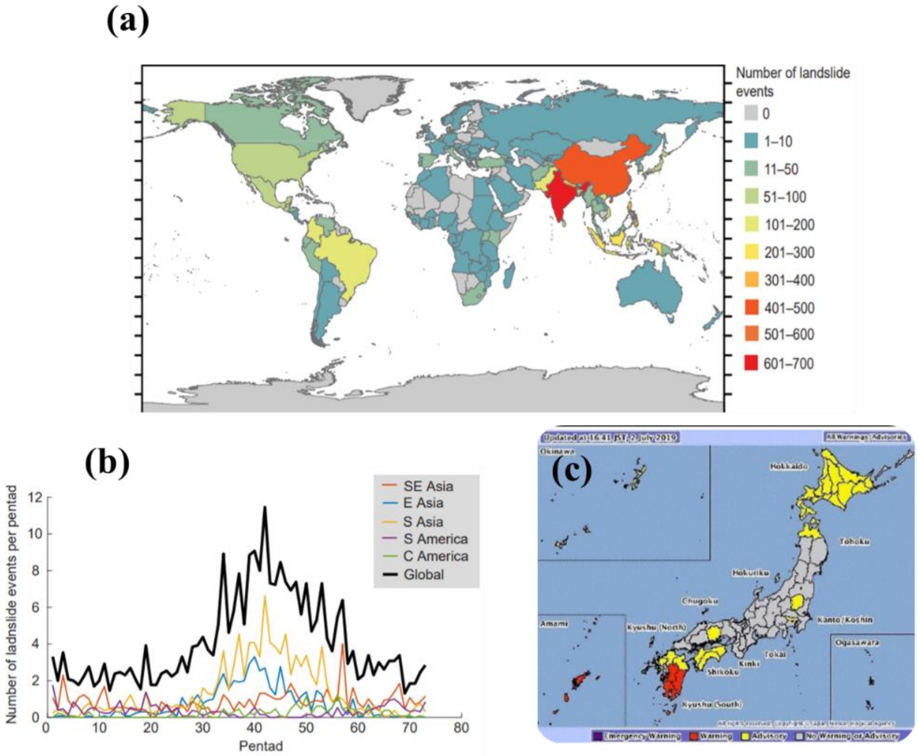

Fig 1.1 Statistics of landslides around the world and in Japan (source: Froude and Petley, 2018): (a) Global map of rainfall-induced landslide from 2004-2016; (b) Mean number of rainfall-induced landslide every 5 days; (c) Landslide distribution map of Japan (source: online)

Table 1.1 Sediment disasters in Japan in recent 10 years

Date	Prefecture	Cause	Death (Missing)
Sep. 2011	Wakayama, Nara and Mie Prefectures	Typhoon No. 12	72 (16)
Aug. 2014	Hiroshima prefecture	Torrential rain	75
Sep. 2015	Kanto and Tohoku regions	Torrential rain	8
Aug. 2017	Iwate prefecture	Typhoon No. 10	20
Jul. 2017	Fukuoka Prefecture, Oita Prefecture	Torrential rain	34 (4)
Jul. 2018	Fukuoka, Saga, Yamaguchi, Hiroshima, Okayama, Hyogo, Kyoto, Ehime, Kochi, etc.	Torrential rain	220 (11)
Oct. 2019	Kanto and Tohoku regions	Typhoon No. 19	66 (13)
Jul. 2020	Kyushu regions	Torrential rain	82 (4)

Therefore, appropriate measures by the national and local governments that manage critical infrastructure for early detection of failure have been widely mentioned to ensure the safety of the public as well as contribute significantly to disaster prevention and mitigation projects, thereby protecting the lives and properties (Hazarika et al. 2016; 2020).

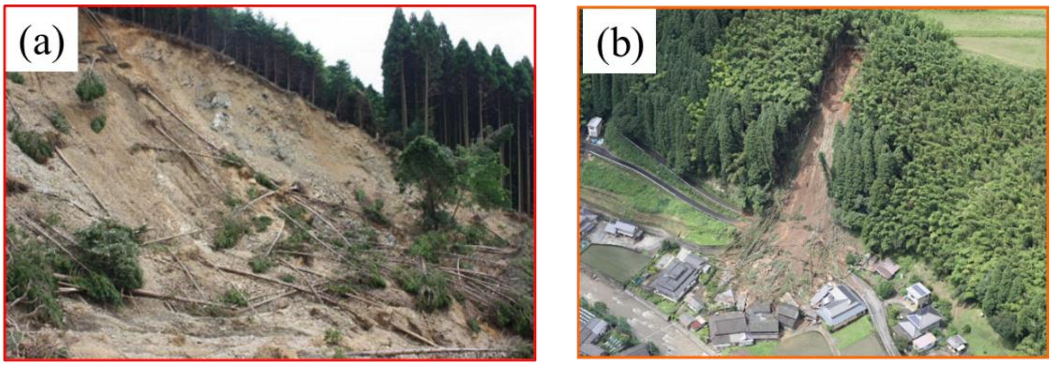

Fig 1.2 Rainfall Induced Disaster Cases in Kyushu, Japan (source: online): (a) Northern Kyushu Torrential Rainfall Disaster in 2017; (b) Extreme Rainfall Event in Kyushu in 2020

1.2 Methods to evaluate the stability of slopes under rainfall

The stability evaluation of slopes under rainfall conditions has been one of the most widely discussed topics in geotechnical engineering. At present, the stability analysis of rainfall-induced slope failure mainly adopts the following three methods: method of software, analytical method and experimental methods.

1.2.1 Evaluate the stability by software

The software method of numerical simulation such as FEM (Finite Element Method), SPH (Smoothed-Particle Hydrodynamic) or DDA (Discontinuous Deformation Analysis) can provide a dynamic failure process without a preset shape or location of slip surface and block movement direction. Any complex slope configuration and soil layer conditions can be simulated in the 2D or 3D form to handle almost all types of failure mechanisms (Berilgen 2007; Griffiths and Marquez 2007; Pinyol et al. 2008; Manenti et al 2019; Su et al 2022). Zhao and You (2020) carried out a 3D two-phase FEM to discuss the stability of the monitoring object under different rainfall effects. It was found that with the continuous rainfall, the slope deformation, and porewater pressure will increase, and it will cause a decrease in the matric suction. Han et al., (2019; 2020) has introduced a HBP based SPH model to simulate the entrainment behavior of debris flow. The dynamic behavior of such disasters has been simulated by SPH scheme, and the Herschel-Bulkley-Papanastasiou (HBP) rheology model was considered in the analysis as well. Guo et al., (2021(a); (b)) considered the effects of matric suction in DDA, and completed the simulation of the SWCC curve, then extended the result of seepage to the analysis of slope stability. Research carried out the seepage simulation on the designated slope, and it expanded the application of the discontinuous deformation method in the unsaturated slope. With the rapid development of computer vision techniques, optical tracking of particles using PIV (Particle Image Velocimetry) and motion analysis is gradually used to conduct real-time monitoring or analysis of failure mechanisms (White et al., 2003; Deng and Haigh, 2022). A large number of scholars continue to optimize the software to improve the precision of captured images (Stanier et al., 2016). research in (Chen et al., 2020) used this technology for the deformation monitoring of an underground structure. Some studies have taken real-time pictures of the monitoring area by building cameras and used computer vision technology to predict and analyze the possibility of landslides (Aggarwal et al 2018). However, this study that only observing the deformation often leads to untimely predictions, which makes it too late to evacuate people. Therefore, a single computer vision technology is not sufficient in the application of early warning systems.

1.2.2 Evaluate the stability by numerical methods

Analytical methods to obtain the factor of safety (F_s) of a slope are based on the theory of limit equilibrium (Vahedifard et al. 2016), slices method (Bishop 1955), slip line theory (Vo and Russell 2017), and limit analysis (He et al. 2019(a)(b); 2022), the sliding surface of the slope is assumed to be a straight line, polyline or logarithmic spirals, which needs to be preset in advance to build the formula. The formula of these methods is mainly based on the balance of soil mechanics or bulk energy. The evaluation of F_s for dry and saturated soil slope has been discussed detailly; when considering fully saturated soil slope, the effect of the pore-water pressure was usually assumed to be coefficient r_u, as introduced by Bishop & Morgenstern (1960). The bigger value of r_u represents more considerable pore-water pressure and a smaller F_s of the slope. While for unsaturated slopes under rainfall conditions, the effects of matric suction should not be ignored. To characterize the shear strength of unsaturated soils, Fredlund et al. (1978) proposed an extended Mohr-Coulomb criterion. And the relationship between the increase of shear strength and matric suction has been studied thoroughly by introducing another material variable, φ_b. Fredlund and Rahardjo (1993) tested on various types of soil, they found that in most cases, φ_b is less than internal friction angle φ.

However, the soil suction was often preset to be a specific value or linearly changes with infiltration depth. While the experimental results show that matric suction tends to change non-linearly along with the infiltration depth (Lu et al, 2012; Bordoni et al, 2015; Dong et al, 2018). Although there is no effective cohesion in silica sand, apparent cohesion (c_{app}) is usually used to emulate the behavior of unsaturated soil, which presents the mobilization of suction stress to shear resistance (Lu and Godt 2008). The value of c_{app} can be defined by soil water retention curve (SWRC) proposed by Mualem (1976) and Van Genuchten (1980). Vahedifard et al. (2016) conducted the stability analysis of unsaturated engineering and natural slopes by combining suction-based effective stress formula with classical limit equilibrium methods. The limit equilibrium method based on the log-helical failure surface proposed in his study involves only two additional hydrodynamic parameters for unsaturated soils. Both parameters are used to describe seepage and effective stress changes in unsaturated soils. The parametric analysis of the study provides stability charts for general use. The effects of infiltration and evaporation on slope stability under four hypothetical soil types are presented. The results show that the apparent cohesion due to suction has a very significant effect on the stability of the slope. In the research of Li et al. (2020;2021), kinematic limit analysis methods are used to estimate the stability of slopes subjected to vertical unsaturated steady flow in the context of 3D rotational failure mechanisms. The shear strength properties of unsaturated soils are revealed. According to the function-function balance equation, the critical cohesive force of the slope under the limit state is calculated and listed in the form of a stable number. Different parameters are graphed in their studies for parametric analysis and practical use in slope design.

Considering the influence of rainfall on the stability of the slope, there are mainly two forms of landslides. The first form is deep-seated slope failure which is mainly due to the saturation or even erosion of the topsoil by rainwater infiltration, such as the Green-Ampt model (Rawls et al., 1983). The topsoil mainly contains the clay layer, weathered soil, tropical residual soil, etc., and the erosion of soil will spread to the whole failure zone, resulting in a rapid and destructive landslide (Gerscovich et al., 2006; Keaton et al. 2014; Huang et al., 2018). Another form of landslide is the occurrence of multiple shallow landslides initiating from slope toe, which usually occur on a sandy slope. It appears with the phenomenon that the slope gradually tends to be saturated from the bottom due to the rise of the groundwater table (Zizioli et al., 2013; Cogan and Gratchev 2019; Wang et al., 2020; Wei et al., 2020).

1.2.3 Evaluate the stability by experimental methods

The experimental method is classic and commonly used, and this method is also the closest to the real landslide disasters. In the preceding experiment studies, various sensors were inserted inside the slope to monitor the soil moisture content, pore-water pressure, slope displacement, etc., and summarize the relevant laws (Chueasamat et al 2018; Cogan and Gratchev 2019; Xie et al.2019). Studies often focus on multiple preconditional, preparatory, and triggering factors, such as rainfall intensity and initial soil moisture content to elucidate the hydrological characteristics, failure forms, and mechanisms under rainfall conditions. Cogan and Gratchev (2019) conducted model tests under different rainfall conditions, and his study considered the rainfall effects of rainfall intensity (40, 70 and 100 mm/h), slope angle (45–55°) and initial soil moisture content (5–12%). Finally, the experiment data was analyed by Intensity-Duration curve and compared with classic results. Xu et al (2022) conducted a series of centrifugal experiments to study the effect of continuous heavy rainfall on the slope stability in the case of cracks after the earthquake. The results are combined with particle image processing and theoretical analysis. This study provides a certain reference for similar engineering geological backgrounds. Huang and Yuin (2010) carried out model experimental analysis on sand slopes, recorded the volume of different shallow landslides, the time of displacement, drew a series of ID curves, and proposed a large number of evaluation expressions. Wang et al (2020) presented the results of a centrifuge test of rainfall-induced instability in a variably saturated slope. This work elucidated the role of rainfall intensity and initial conditions (eg, slope angle, porosity, and soil saturation) on the kinematics of failure onset and after failure. The failure modes, infiltration profiles and deformations were characterized in the initial and post-failure stages. Following the summary, two failure modes are introduced, whose test data are presented in two threshold curves together with literature data to define the critical conditions for slope failure under rainfall infiltration.

However, the experimental method has several shortcomings. One of them is that only a single soil parameter and external influencing factors are considered in each experiment and only a limited number of cases can be obtained, which severely limits the evaluation and application value. Another shortcoming is that there is no risk quantification for the characteristics of the parameter changes monitored by the test, which makes it difficult to quickly grasp the safety of the slope. This study attempts to address the shortcomings of the above analysis methods.

1.3 Approach to landslide disaster reduction

1.3.1 Evaluation of various disaster reduction methods

In order to save human lives and protect properties during rainfall events, many scholars continue to conduct research to mitigate such disasters. Research concluded that methods to mitigate the damage often target the following characteristics: (1) it should have a good reinforcement effect; (2) a good predictability to carry out evacuations before disasters; (3) easy for users to operate without professional skills; (4) cost-effective: making it possible to be widely applied in all countries; (5) sustainable enough to reduce energy dependence and environmental damage. Of all the features, the most crucial is undoubtedly validity and accuracy, which are the premise of all methods. Because wrong or untimely predictions can lead to very serious consequences. Therefore, empirical methods and probabilistic methods, which has been widely used in some areas with a large number of mountains, such as Sichuan in China, Japan, the United States, etc. These methods define thresholds to evaluate the relationship between rainfall intensity and duration time and determine the possibility of landslides (Chang and Chiang 2009; Peruccacci et al., 2017; Saito et al., 2010; Baum and Godt 2010; Capparelli and Tiranti 2010). Due to accuracy limitations, empirical methods and probabilistic methods are only suitable for regional monitoring, it will ignore a lot of the fragile slopes in the mountainous. The prediction results of some professional tools such as geographic information system (GIS), Global Navigation Satellite System (GNSS) and InSAR are more accurate than *I-D* curve method, the cost is much higher and professional technology is needed during the operation (Liao et al., 2010; Tu et al., 2013; Lee et al., 2016, Yang et al., 2019; Piciullo et al., 2020; Dai C et al., 2021). Traditional reinforcement methods such as piling or anchor rods can effectively prevent slope instability (Li et al., 2010; He et al., 2015; Hazarika et al., 2016), but it is very expensive to carry out reinforcement equipment on a large scale in the mountains, making it impossible for even developed countries to afford. To achieve the goal of prediction with easy operation, Early Warning System (EWS) has been used as an effective tool to monitor the stability of slopes in many studies, and it provides a very good platform for predicting landslides. EWS is based on the characteristics of the research object, by collecting relevant data and information, monitoring the changing trend of risk factors, and evaluating the degree of deviation of various risk states. Finally, EWS will send early warning signals to the decision-making level and take pre-control countermeasures in advance. In the comprehensive comparison of various methods, research finds that the methods combined with hardware and software perform better in protection or predictability, which can get a very good balance of accuracy, easy operation, cost-effectiveness, and sustainability. In such methods, the application of the landslide Early Warning System (EWS) is considered to be a practical approach to mitigating disasters (Tu et al., 2013; Lee et al., 2016, Yang et al., 2019; Piciullo et al., 2020; Dai C et al., 2021)

1.3.2 Implemented EWS around the world

Tilt sensor and volumetric water content sensor were used by Uchimura et al. (2009) and installed on a real slope in Kobe City, Japan. But the whole system does not have the advantage of sustainability because of the high energy consumption of sensors. Dikshit et al. (2017) developed EWS using tilt sensors in Himalayan regions and determined tilt angle thresholds of the slope empirically. However, if only the deformation recorded from the tilt sensor is considered to forecast the occurrence of a landslide, the early warning work cannot be timely enough for prepare some evacuation work or transfer property, personnel, etc. Research in (Chen et al., 2020) used IoT-based monitoring technology for the deformation monitoring of an underground structure. It’s mainly about computer vision-based sensors for the tilt monitoring, but only monitoring the deformation makes the result of prediction is not timely enough as well. Therefore, the Internet of Things technology of computer vision can be used as an auxiliary significance for monitoring. Gian et al. (2017) proposed an EWS consisting of six sensor nodes and one precipitation station In Vietnam, but the prediction work relied on the monitoring data to conduct the numerical simulations and the indicators (pore water pressure, water content and tilt angle) were not quantified to find the rules in their work. Another problem is that their developed EWS cost so much, making it quite difficult to afford on a large scale and hard to find so many professional operators to run the system. Research from Abraham et al (2020) shows that, in order to improve the efficiency of EWS and to evaluate the thresholds of the monitoring data, the research used Microelectromechanical systems (MEMS)-based tilt sensors and volumetric water content sensors to monitor slopes in the Himalayas. Internet of Things (IoT) based networks used wireless modules to communicate between individual sensors and data loggers and from data loggers to internet databases. The slopes were continuously monitored during the three monsoon seasons (from 2017 to 2019) and the sensor data were compared with field observations and rainfall data for evaluation. The study explored the relationship between slope change, volumetric soil moisture content, and rainfall, with records demonstrating the importance of considering long-term rainfall conditions rather than immediate rainfall events when developing rainfall thresholds for the region. Although the technological innovation is outstanding and the sustainability is strong, the cost is still high and the operation is more complicated. Through the above EWS in different regions, as **Table 1.2** shows, The above mentioned EWS have in general the following shortcomings: (1) Relying on a single tilt sensor or image sensor leads to the untimely early warning, such as EWS in Japan and China; (2) The development cost is still high and most of the mentioned EWS above perform high power consumption; (3) These EWS mainly use systems that are industrially manufactured, therefore, it is not possible for the users to modify or upgrade the hardware or software architecture by themselves. These are all significant defects, the large-scale launch of EWS and making it suitable for more application scenarios and monitoring requirements, these deficiencies need to be overcome. Currently, by the comparison of the mentioned EWS, it is found that the early warning system based on the Internet of Things has the greatest advantages in controlling costs, improving sustainability, and balancing accuracy. In addition, the IoT-based operating platform usually provides open architecture of both hardward and software aspects and makes it much more feasible for users to conduct development work. Therefore, this study will focus on IoT-based EWS for the monitoring of landslides.

Table 1.2 Current EWS that applied in different countries

Countries where implemented	Feature	Shortcomings
Japan (Uchimura et al., 2009)	Tilt sensors and moisture content sensors were used in the system	Only considers two sensors and the prediction is not timely; Not sustainable from the view of energy consumption
India (Dikshit et al., 2017)	Sensor data such as rainfall, moisture, pore water pressure and ground movement is wirelessly collected	High-cost of sensors and high energy consumption. System does not have open architecture, therefore indigenous development and modification is not possible
China (Chen et al., 2020)	Computer vision–based sensors for the tilt monitoring	Prediction is not timely enough and the system is not sustainable
Vietam (Gian et al., 2017)	Wireless communication system with six types of sensors	Relies on numerical simulation, system is financially not sustainable.
Germany / Colombia (Abraham et al., 2020)	IoT-based sensor network for communities based on open-source hardware and software	High cost of setup and high energy consumption

1.4 Current EWS based on IoT

In recent years, research found that the application of wireless Early Warning System (EWS) based on Internet of Things (IoT) is considered an effective approach to disaster reduction (Giri et al., 2018; Karunarathne et al., 2020; Gamperl et al., 2021; Liu et al., 2021). IoT is a booming technology platform that seamlessly connects smart devices, research objects, and transmission machines through the Internet (Kanaya et al., 2013; 2021). Compared with above methods, the wireless Early Warning System based on IoT has obvious advantages. Research from (Shi et al., 2015) showed that EWS based on IoT can provide real-time data monitoring, transmission and storage, which allows remote analysis and gives timely warning. Lee et al. (2017) found that power consumption of sensors, transmission machines and routers during system operation is not high, which ensures long endurance of monitoring. EWS based on IoT can also quickly adapt to various sensors, which makes it easy for users to update connected sensors in time according to different requirements (Mois et al., 2017). In addition, prediction method that combines computer vision with IoT has gradually become a hot topic pursued by researchers. Computer vision technology can extract meaningful information from digital images and videos, and this information can be used to assess risks, take action or provide opinions, etc. Currently, research in (Chen et al., 2020) used this technology for the deformation monitoring of an underground structure. Some studies have taken real-time pictures of the monitoring area by building cameras and used computer vision technology to predict and analyze the possibility of landslides (Aggarwal et al 2018). However, this study that only observing the deformation often leads to untimely predictions, which makes it too late to evacuate people. Therefore, a single computer vision technology is not sufficient in the application of early warning systems.

1.4.1 Sensors used in the system

Regarding IoT-based EWS with different sensors, research in (Ramesh, 2014; Karunarathne et al, 2020) has been introduced in great detail and comprehensively. This study organizes their research and lists these common sensors below:

Capacitance type soil moisture sensors: It is used to monitor the moisture content or volumetric moisture content in the slope by converting the resistance signal into the moisture content sensor.

Pore water pressure sensor: it is always used in rainy seasons. The rainwater will speard in the pores of the soil, which forms a negative pressure and looses the soil strength. Therefore, if research wants to measure the groundwater table by pore water pressure, pore water pressure sensor should be considered.

Strain gauges: it measures the relative movement of the soil layer, which is done by connecting to the Deep Earth Probe. The deflection of the Earth Probe needs to be detected every 0.5 mm deep. Therefore, the experiments used strain gauges with different resistances of 100X, 350X and 1000X.

High-precision inclinometers are more useful in research. For example, inclinometers are used to measure the movement of soil layers, whether it is very slow wriggling or sudden violent movements, and can accurately measure the results.

Geophones: it is often used to analyze deflection, which requires measurement frequencies near 250 Hz due to the unique characteristics of landslides. At the same time, we should collect the corresponding measurement values in time to control the resolution within 0.1 Hz.

Rain gauges: Rain infiltrating the slope may cause changes in soil suction and positive pore pressure, increasing the likelihood of landslide rock and soil shear strength lower if the depth of the main groundwater table or soil unit weight increases.

Temperature sensors: Mearings the temperature of the soil, which is usually used in frozen soil areas.

1.4.2 Network Layer in the system

Network Layer is the middle layer in the IoT architecture, which is also called transmission layer. It processes the information provided by the previous layer by transmitting relevant data and information to IoT hubs and devices through an integrated network. Different communication technologies such as Bluetooth and Wi-Fi, and various connection devices, including hubs and gateways are gathered in this layer, which makes it necessary.

For the consideration of Internet, wireless 3G or 4G provided by a cellular modem has been used for Internet access. Information transfer between the local computer and sensors can be achieved by three tools, including Bluetooth low energy (BLE), wireless transceivers or serial communication (Giri et al 2018). Among them, The maximum communication distance of the first two is shorter, theoretically 100 meters, but the latter is longer and can reach nearly 5000 meters.

With the development of LPWANs technology, the communication landscape has been further improved. LPWANs has the ability to cover long-distance transfering by working based on sub-GHz frequencies with high energy efficient. The obvious disadvantage of LPWANs is low baud rates, but for long time duration of measuring or monitoring, it can meet the needs of most IoT devices. **Fig 1.3** presents the several mainstream communication methods, For example: common used 3G, 4G, LTE or 5G, NFC, WIFI, Bluetooth and LPWA. It can be found that Low-Power Wide-Area (LPWA) network technology provides additional benefits of long-range data communication, low power requirements, and low cost due to usage of license-free bands of radio spectrum in the tire of data transmission. Although it is shown in **Fig 1.3 (b)** that the amount of propagating data is very low, considering that landslide monitoring is a long-term process, the accumulation of displacement, and the increase of water content is developed slowly, so the lower amount of data is acceptable in EWS.

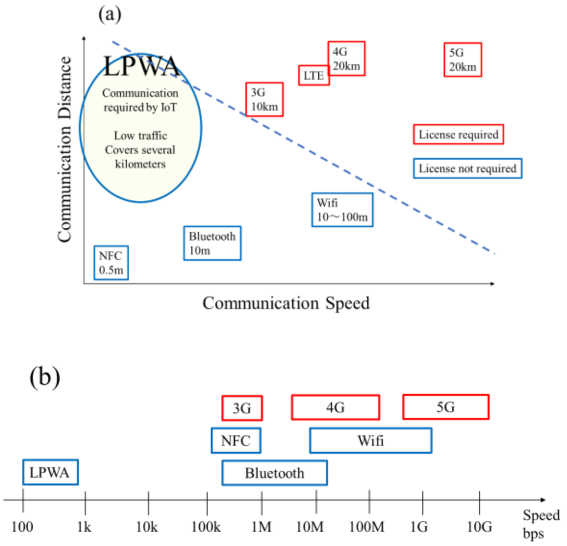

Fig 1.3 Comparisons of major wireless technologies; (a) Communication distance of each technology; (b) Communication data transmit the speed of each technology

Sigfox (Hobbs et al. 2020) was among the few first LPWANs to be commercially available. The network is organized in cells, each one covering a maximum area of 50 km, allowing up to 140 uplinks and 4 downlinks per device, per day. The technology operates as a one-hop star topology although the network requires a mobile operator to carry the generated traffic. In the Sigfox business model, the network access points are owned by the Sigfox company or official representatives, and users need to pay a premium per device per day.

LoRa – abbreviation for Long Range – is another popular LPWAN. Similarly, to Sigfox, it operates at low, sub-GHz frequencies at low duty-cycles, thus addressing the range-vs-energy trade-off. The main difference to Sigfox lies in the business model it assumes. The ownership and operation of LoRaWAN access points are open to everyone, and therefore, LoRa supports the operation of private IoT networks. Certain initiatives, such as The Things Network , leverage upon this model in order to develop crowdsourced IoT networks spanning across entire regions (the UK network spans across the entire country and continues to grow).

Complimentary to Sigfox and LoRa – wireless technologies that rely upon IoT-specific infrastructure – there are IoT wireless technologies being introduced that operate over the existing cellular network. NB-IoT (narrowband IoT) is such a technology that focuses specifically on indoor coverage, low cost, long battery life, and high connection density. It makes use of the LTE standard but dramatically limits the bandwidth, thus achieving energy efficiency. The great advantage of this technology is the fact that it makes use of the existing cellular infrastructure that already provides good coverage both indoors and outdoors. **Fig 1.4** demonstrates a comparison of Sigfox, LoRa and NB-IoT.

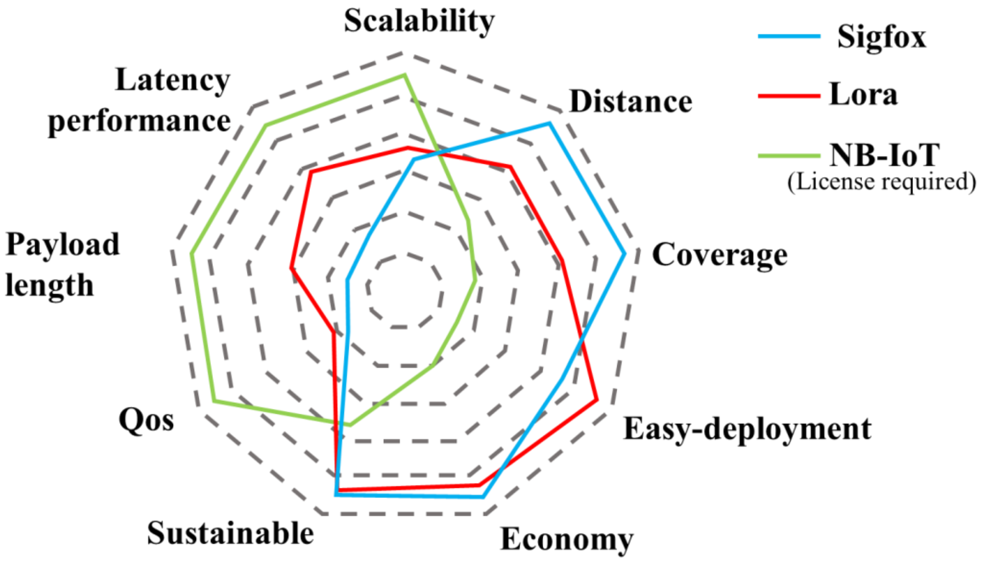

Fig 1.4 Comparisons of Sigfox, LoRa and NB-IoT (Karunarathne et al. 2020)

1.5 Research objectives

Through the review of disasters caused by heavy rainfall in Kyushu, the evaluation of slope stability under rainfall conditions, the comparison of landslide mitigation methods, and the elaboration of the current development of early warning systems, this study has identified the following objectives:

(1) To reveal the failure mechanism and stability analysis of the slope under rainfall conditions;

(2) To develop low-cost and sustainable early warning systems that can meet different geological conditions and network communication status;

(3) To propose an effective evaluation index among various precursory phenomena of the landslide;

(4) To introduce the application of EWS to the actual engineering projects, which can ensure the safety of the public as well as contribute greatly to disaster prevention, thereby protecting the lives and properties.

(5) To present how IoT-based EWS can forge new paths for interdisciplinary study and generate a positive impact on SDGs.

1.6 Original contributions to the knowledge

The research mainly focuses on the insufficiency of slope stability assessment under rainfall conditions and the development of early warning system. The specific original contributions include:

(1) **Stability analysis of unsaturated slopes for the early warning system considering different soil types and failure modes under continuous rainfall.** According to the different properties of soil, this work is divided into cohesive (clay, loess, silt) and cohesionless soil (sand). Research considers the deep failure mode of cohesive soil and the upper bound limit analysis is used to evaluate its stability; The shallow failure mode with cohesionless soil was analyzed by the consideration of Transient Rainfall Infiltration and Grid-Based Regional Slope-Stability (TRIGRS) model with the nonlinear suction equation (***Chapter 2***).

(2) **New developed low-cost and sustainable EWS based on IoT.** This part aims to address the shortcomings of the previous EWS and develops a low-cost and sustainable early warning systems based on IoT, which presents the obvious advantage of Low cost, low power consumption, open architecture for developers. In addition, the proposed EWS also provides the option to option to use both cellular networks and freely available radio frequency waves for data transmission through Low Power Wide Area (LPWA) connectivity system. (***Chapter 3***).

(3) **Proposing an effective evaluation index model of landslide through the analysis of the model test with motion analysis and interpolation analysis.** This part conducts a comprehensive study combining experimental, analytical, and software methods. The experimental method evaluated the distribution of soil moisture content and the migration of groundwater table. A real-time local factor of safety ($\boldsymbol{F}_\mathrm{s}$) during continuous rainfall periods was evaluated by the analytical technique. Parameters measured from the model test and $\boldsymbol{F}_\mathrm{s}$ estimations from the analytical technique were utilized to carry out an interpolation analysis to predict the data for additional rainfall conditions. Experimental validation and cross-

validation were used to ensure the feasibility of the interpolation result. Motion analysis based on **PIV** (Particle Image Velocimetry) provide the velocity of particle flow and displacement accumulation. Based on the rainwater infiltration trend, failure mechanism and soil movement during a landslide, this research classifies three stages of Initial Monitoring State, Alert State and Triggerring State to the proposed EWS, which can be regarded as an essential guide for the prediction of rainfall-induced shallow landslides in the field. (***Chapter 4 and 5***).

1.7 Organization of thesis

The detailed flow chart of this study is shown in **Fig 1.5.**

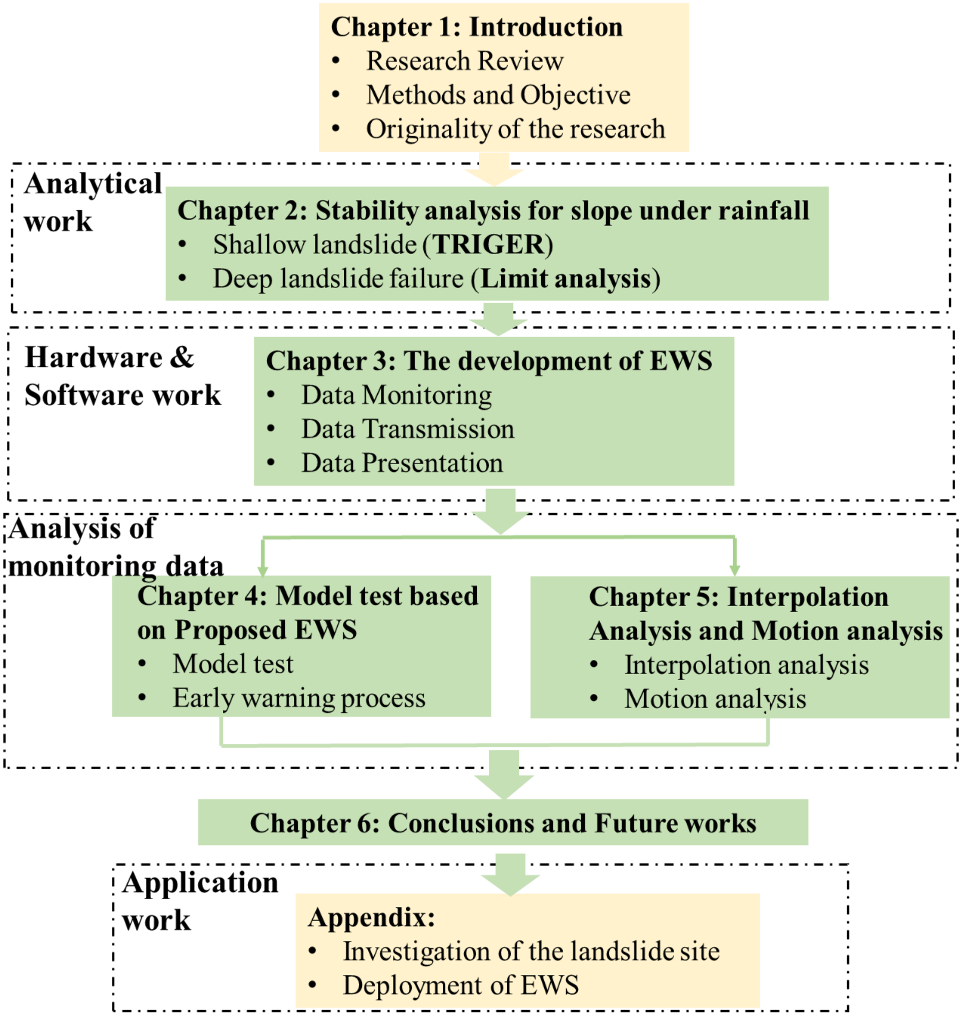

Fig 1.5 Flow chart of this thesis

Reference

Abraham, M. T., Satyam, N., Pradhan, B., & Alamri, A. M. (2020). IoT-based geotechnical monitoring of uns**Table** slopes for landslide early warning in the Darjeeling Himalayas. Sensors, 20(9), 2611.

Aggarwal, S., Mishra, P. K., Sumakar, K. V. S., & Chaturvedi, P. (2018, April). Landslide monitoring system implementing IOT using video camera. In *2018 3rd International Conference for Convergence in Technology (I2CT)* (pp. 1-4). IEEE.

Baum, R. L., & Godt, J. W. (2010). Early warning of rainfall-induced shallow landslides and debris flows in the USA. *Landslides*, *7*(3), 259-272.

Berilgen, M. M. (2007). Investigation of stability of slopes under drawdown conditions. *Computers and Geotechnics*, *34*(2), 81-91.

Bishop, A. W. (1955). The use of the slip circle in the stability analysis of slopes. *Geotechnique*, *5*(1), 7-17.

Bishop, A. W., & Morgenstern, N. (1960). Stability coefficients for earth slopes. *Geotechnique*, *10*(4), 129-153.

Bordoni, M., Meisina, C., Valentino, R., Lu, N., Bittelli, M., & Chersich, S. (2015). Hydrological factors affecting rainfall-induced shallow landslides: from the field monitoring to a simplified slope stability analysis. *Engineering Geology*, *193*, 19-37.

Capparelli, G., & Tiranti, D. (2010). Application of the MoniFLaIR early warning system for rainfall-induced landslides in Piedmont region (Italy). *Landslides*, *7*(4), 401-410.

Chang, K. T., & Chiang, S. H. (2009). An integrated model for predicting rainfall-induced landslides. *Geomorphology*, *105*(3-4), 366-373.

Chen, I. H., Lin, Y. S., & Su, M. B. (2020). Computer vision–based sensors for the tilt monitoring of an underground structure in a landslide area. *Landslides*, *17*(4), 1009-1017.

Chen, I. H., Lin, Y. S., & Su, M. B. (2020). Computer vision–based sensors for the tilt monitoring of an underground structure in a landslide area. Landslides, 17(4), 1009-1017.

Cogan J., Gratchev I. (2019). A study on the effect of rainfall and slope characteristics on landslide initiation by means of flume tests. *Landslides*, 16(12): 2369-2379

Dai C., Li W., Wang D., et al. 2021. Active Landslide Detection Based on Sentinel-1 Data and InSAR Technology in Zhouqu County, Gansu Province, Northwest China. Journal of Earth Science, 32(5): 1092-1103.

Deng, C., & Haigh, S. K. (2022). Sand deformation mechanisms mobilised with active retaining wall movement. *Géotechnique*, *72*(3), 260-273.

Dikshit, A., Satyam, D. N., & Towhata, I. (2018). Early warning system using tilt sensors in Chibo, Kalimpong, Darjeeling Himalayas, India. Natural Hazards, 94(2), 727-741.

Dong, Y., Lu, N., & McCartney, J. S. (2018). Scaling shear modulus from small to finite strain for unsaturated soils. *Journal of Geotechnical and Geoenvironmental Engineering*, *144*(2), 04017110.

Fredlund, D. G., & Rahardjo, H. (1993). *Soil mechanics for unsaturated soils*. John Wiley & Sons.

Fredlund, D. G., Morgenstern, N. R., & Widger, R. A. (1978). The shear strength of unsaturated soils. *Canadian Geotechnical Journal*, *15*(3), 313-321.

Froude, M. J., & Petley, D. N. (2018). Global fatal landslide occurrence from 2004 to 2016. *Natural Hazards and Earth System Sciences*, *18*(8), 2161-2181.

Gerscovich, D. M. S., Vargas Jr, E. A., & De Campos, T. M. P. (2006). On the evaluation of unsaturated flow in a natural slope in Rio de Janeiro, Brazil. *Engineering Geology*, *88*(1-2), 23-40.

Gian, Q. A., Tran, D. T., Nguyen, D. C., Nhu, V. H., & Tien Bui, D. (2017). Design and implementation of site-specific rainfall-induced landslide early warning and monitoring system: a case study at Nam Dan landslide (Vietnam). Geomatics, Natural Hazards and Risk, 8(2), 1978-1996.

Giri, P., Ng, K., & Phillips, W. (2018). Wireless sensor network system for landslide monitoring and warning. *IEEE Transactions on Instrumentation and Measurement*, *68*(4), 1210-1220.

Giri, P., Ng, K., & Phillips, W. (2018). Wireless sensor network system for landslide monitoring and warning. *IEEE Transactions on Instrumentation and Measurement*, *68*(4), 1210-1220.

Griffiths, D. V., & Marquez, R. M. (2007). Three-dimensional slope stability analysis by elasto-plastic finite elements. *Geotechnique*, *57*(6), 537-546.

Guo, L., Chen, G., Gao, J., & Li, C. (2021). Micro-scale analysis on shear characteristics of unsaturated soil by considering capillary suction and adsorption suction based on DDA. *Engineering Analysis with Boundary Elements*, *132*, 321-334.

Guo, L., Chen, G., Li, C., Xia, M., Gong, S., & Zheng, L. (2021). A bound water model for numerical simulation of SWCC in the wide suction range based on DDA. *Computers and Geotechnics*, *139*, 104378.

Han, Z., Su, B., Li, Y., Dou, J., Wang, W., & Zhao, L. (2020). Modeling the progressive entrainment of bed sediment by viscous debris flows using the three-dimensional SC-HBP-SPH method. *Water Research*, *182*, 116031.

Han, Z., Su, B., Li, Y., Wang, W., Wang, W., Huang, J., & Chen, G. (2019). Numerical simulation of debris-flow behavior based on the SPH method incorporating the Herschel-Bulkley-Papanastasiou rheology model. *Engineering Geology*, *255*, 26-36.

Hazarika H., Kazama M., Lee WF., (2016) Geotechnical Hazards from Large Earthquakes and Heavy Rainfalls. Springer

Hazarika, H., Yamamoto, S., Ishizawa, T., Danjo, T., Kochi, Y., Fujishiro, T., ... & Ishibashi, S. (2020). The 2017 July Northern Kyushu torrential rainfall disaster—geotechnical and geological perspectives. In Geotechnics for natural disaster mitigation and management (pp. 1-19). Springer, Singapore.

He, Y., Liu, Y., Hazarika, H., & Yuan, R. (2019). Stability analysis of seismic slopes with tensile strength cut-off. *Computers and Geotechnics*, *112*, 245-256.

He, Y., Liu, Y., Zhang, Y., & Yuan, R. (2019). Stability assessment of three-dimensional slopes with cracks. *Engineering Geology*, *252*, 136-144.

He, Y., Yu, J., Yuan, R., Wang, W., & Nikitas, N. (2022). Stability and failure mechanisms in three-dimensional cracked slope: Static and dynamic analysis. *Computers and Geotechnics*, *144*, 104626.

Hobbs, P. R. N., Jones, L. D., Kirkham, M. P., Pennington, C. V. L., Morgan, D. J. R., & Dashwood, C. (2020). Coastal landslide monitoring at aldbrough, east riding of Yorkshire, UK. *Quarterly Journal of Engineering Geology and Hydrogeology*, *53*(1), 101-116.

Huang, C. C., & Yuin, S. C. (2010). Experimental investigation of rainfall criteria for shallow slope failures. *Geomorphology*, *120*(3-4), 326-338.

Huang, W., Leong, E. C., & Rahardjo, H. (2018). Upper-bound limit analysis of unsaturated soil slopes under rainfall. *Journal of Geotechnical and Geoenvironmental Engineering*, *144*(9), 04018066.

Kanaya, H., Mansour, M. M., Hatanaka, S., Nakashima, A., & Takiguchi, O. (2021). Battery-Less Infrastructure Monitoring Sensor Platform. In *Advances in Sustainable Construction and Resource Management* (pp. 907-915). Springer, Singapore.

Kanaya, H., Tsukamaoto, S., Hirabaru, T., Kanemoto, D., Pokharel, R. K., & Yoshida, K. (2013). Energy harvesting circuit on a one-sided directional flexible antenna. *IEEE Microwave and Wireless Components Letters*, *23*(3), 164-166.

Karunarathne, S. M., Dray, M., Popov, L., Butler, M., Pennington, C., & Angelopoulos, C. M. (2020). A technological framework for data-driven IoT systems: Application on landslide monitoring. *Computer Communications*, *154*, 298-312.

Karunarathne, S. M., Dray, M., Popov, L., Butler, M., Pennington, C., & Angelopoulos, C. M. (2020). A technological framework for data-driven IoT systems: Application on landslide monitoring. *Computer Communications*, *154*, 298-312.

Keaton, J. R., J. Wartman, S. Anderson, J. Benoît, J. deLaChapelle, R. Gilbert, and D. R. Montgomery. (2014). The 22 March 2014 Oso Landslide, Snohomish County, Washington. Arlington, VA: Geotechnical Extreme Event Reconnaissance (GEER), National Science Foundation

Lee, J., Pullen, S., Datta-Barua, S., & Lee, J. (2016). Real-time ionospheric threat adaptation using a space weather prediction for GNSS-based aircraft landing systems. *IEEE Transactions on Intelligent Transportation Systems*, *18*(7), 1752-1761.

Li, X., He, S., & Wu, Y. (2010). Seismic displacement of slopes reinforced with piles. Journal of Geotechnical and Geoenvironmental Engineering, 136(6), 880-884.

Li, Z. W., & Yang, X. L. (2018a). Stability of 3D slope under steady unsaturated flow condition. *Engineering geology*, *242*, 150-159.

Li, Z. W., & Yang, X. L. (2018b). Active earth pressure for soils with tension cracks under steady unsaturated flow conditions. *Canadian Geotechnical Journal*, *55*(12), 1850-1859.

Liao, Z., Hong, Y., Wang, J., Fukuoka, H., Sassa, K., Karnawati, D., & Fathani, F. (2010). Prototyping an experimental early warning system for rainfall-induced landslides in Indonesia using satellite remote sensing and geospatial datasets. *Landslides*, *7*(3), 317-324.

Liu, Y., Hazarika, H., Takiguchi, O., & Kanaya, H. (2021). Developing a Sustainable System for Early Warning Against Landslides During Rainfall. In *Advances in Sustainable Construction and Resource Management* (pp. 917-926). Springer, Singapore.

Lu, N., and J. W. Godt (2008), Infinite slope stability under unsaturated seepage conditions, Water Resour. Res., 44, W11404, doi:10.1029/ 2008WR006976

Lu, N., Şener-Kaya, B., Wayllace, A., & Godt, J. W. (2012). Analysis of rainfall-induced slope instability using a field of local factor of safety. *Water Resources Research*, *48*(9).

Manenti, S., Wang, D., Domínguez, J. M., Li, S., Amicarelli, A., & Albano, R. (2019). SPH modeling of water-related natural hazards. *Water*, *11*(9), 1875.

Ministry of Land, Infrastructure, Transport and Tourism, Japan., 2020. Damage and response due to heavy rain in 2020 (In Japanese) https://www.mlit.go.jp/river/shinngikai_blog/hazard_risk/dai05kai/dai05kai_sankosiryo02.pdf

Mois, G., Folea, S., & Sanislav, T. (2017). Analysis of three IoT-based wireless sensors for environmental monitoring. *IEEE Transactions on Instrumentation and Measurement*, *66*(8), 2056-2064.

Mualem, Y. (1976). A new model for predicting the hydraulic conductivity of unsaturated porous media. *Water resources research*, *12*(3), 513-522.

Peruccacci, S., Brunetti, M. T., Gariano, S. L., Melillo, M., Rossi, M., & Guzzetti, F. (2017). Rainfall thresholds for possible landslide occurrence in Italy. *Geomorphology*, *290*, 39-57.

Piciullo, L., Tiranti, D., Pecoraro, G., Cepeda, J. M., & Calvello, M. (2020). Standards for the performance assessment of territorial landslide early warning systems. *Landslides*, *17*(11), 2533-2546.

Pinyol, N. M., Alonso, E. E., & Olivella, S. (2008). Rapid drawdown in slopes and embankments. *Water resources research*, *44*(5).

Ramesh, M. V. (2014). Design, development, and deployment of a wireless sensor network for detection of landslides. *Ad Hoc Networks*, *13*, 2-18.

Rawls, W. J., Brakensiek, D. L., & Miller, N. (1983). Green-Ampt infiltration parameters from soils data. *Journal of hydraulic engineering*, *109*(1), 62-70.

Saito, H., Nakayama, D., & Matsuyama, H. (2010). Relationship between the initiation of a shallow landslide and rainfall intensity—duration thresholds in Japan. *Geomorphology*, *118*(1-2), 167-175.

Shi, G., Zhang, J., Dong, C., Han, P., Jin, Y., & Wang, J. (2015, June). Fall detection system based on inertial mems sensors: Analysis design and realization. In *2015 IEEE International Conference on Cyber Technology in Automation, Control, and Intelligent Systems (CYBER)* (pp. 1834-1839). IEEE.

Stanier, S. A., Blaber, J., Take, W. A., & White, D. J. (2016). Improved image-based deformation measurement for geotechnical applications. Canadian Geotechnical Journal, 53(5), 727-739.

Su, Z., Wang, G., Wang, Y., Luo, X., & Zhang, H. (2022). Numerical simulation of dynamic catastrophe of slope instability in three Gorges reservoir area based on FEM and SPH method. *Natural Hazards*, *111*(1), 709-724.

Uchimura, T., Towhata, I., Lan Anh, T. T., Fukuda, J., Bautista, C. J., Wang, L., ... & Sakai, N. (2010). Simple monitoring method for precaution of landslides watching tilting and water contents on slopes surface. Landslides, 7(3), 351-357.

Vahedifard, F., Leshchinsky, D., Mortezaei, K., & Lu, N. (2016). Effective stress-based limit-equilibrium analysis for homogeneous unsaturated slopes. *International Journal of Geomechanics*, *16*(6), D4016003.

Van Genuchten, M. T. (1980). A closed-form equation for predicting the hydraulic conductivity of unsaturated soils. *Soil science society of America journal*, *44*(5), 892-898.

Vo, T., & Russell, A. R. (2017). Stability charts for curvilinear slopes in unsaturated soils. *Soils and foundations*, *57*(4), 543-556.

Wang, F., Dai, Z., Takahashi, I., & Tanida, Y. (2020). Soil moisture response to water infiltration in a 1-D slope soil column model. *Engineering Geology*, *267*, 105482.

Wei, Z. L., Wang, D. F., Sun, H. Y., & Yan, X. (2020). Comparison of a physical model and phenomenological model to forecast groundwater levels in a rainfall-induced deep-seated landslide. Journal of Hydrology, 586, 124894.

White, D. J., Take, W. A. & Bolton, M. D. (2003). Soil deformation measurement using particle image velocimetry (PIV) and photogrammetry. Géotechnique 53, No. 7, 619–631,

Xie J., Uchimura T., Chen P., (2019). A relationship between displacement and tilting angle of the slope surface in shallow landslides. *Landslides*, 16(6): 1243-1251

Xu, J., Ueda, K., & Uzuoka, R. (2022). Evaluation of failure of slopes with shaking-induced cracks in response to rainfall. *Landslides*, *19*(1), 119-136.

Yang, Y., Gao, W., Guo, S., Mao, Y., & Yang, Y. (2019). Introduction to BeiDou-3 navigation satellite system. *NAVIGATION, Journal of the Institute of Navigation*, *66*(1), 7-18.

Zhao, L., & You, G. (2020). Rainfall affected stability analysis of Maddingley Brown Coal eastern batter using Plaxis 3D. *Arabian Journal of Geosciences*, 13(20), 1-12.

Zizioli, D., Meisina, C., Valentino, R., & Montrasio, L. (2013). Comparison between different approaches to modeling shallow landslide susceptibility: a case history in Oltrepo Pavese, Northern Italy. *Natural Hazards and Earth System Sciences*, *13*(3), 559-573.

CHAPTER 2

2. STABILITY ANALYSIS OF UNSATURATED SLOPES UNDER RAINFALL CONDITIONS

2.1 Introduction

Through the geological investigation and engineering project case report, it is found that there are mainly two forms of slope failure considering the influence of rainfall conditions. One is the shallow slope failure caused by the rise of the groundwater table from the bottom to up, and the other is the deep slope failure caused by the saturated state from the upon to the bottom. As **Fig 2.1 (a)** shows, the first form is the occurrence of multiple shallow landslides initiating from slope toe, which usually occurs on a sandy slope. It appears with the phenomenon that the slope gradually tends to be saturated from the bottom due to the rise of the groundwater table (Zizioli et al., 2013; Cogan and Gratchev 2019; Wang et al., 2020; Wei et al., 2020). Many sandy slopes exist in an unsaturated state in nature and due to the existence of matric suction, the factor of safety of these unsaturated slopes is higher than that of saturated slopes (Fredlund and Rahardjo., 1993; Vahedifard et al., 2016; Li et al., 2018(a,b)). However, when rainfall occurs, pore water pressure increases significantly with the increase of soil moisture content, which significantly influences the overall stability of the slope. The other form is deep-seated slope failure which is mainly due to the saturation or even erosion of the topsoil by rainwater infiltration, such as the Green-Ampt model (Rawls et al., 1983). As Fig 2.1 (b) shows, the soil initially contains a certain amount of natural water content, then the downward infiltration of rainwater into the soil forms a wetting front of depth ΔH from the ground surface, this causes the infiltrated part to change to the saturated state. The topsoil mainly contains the clay layer, weathered soil, tropical residual soil, etc., and the erosion of soil will spread to the whole failure zone, resulting in a rapid and destructive landslide (Gerscovich et al., 2006; Keaton et al. 2014; Huang et al., 2018). According to the properties of different soil layers and failure modes, the research is mainly carried out through two points: (1) considering the shallow failure of non-cohesive soil; (2) considering the deep failure of cohesive soil. Both of these two modes will be analyzed the factor of safety under rainfall conditions.

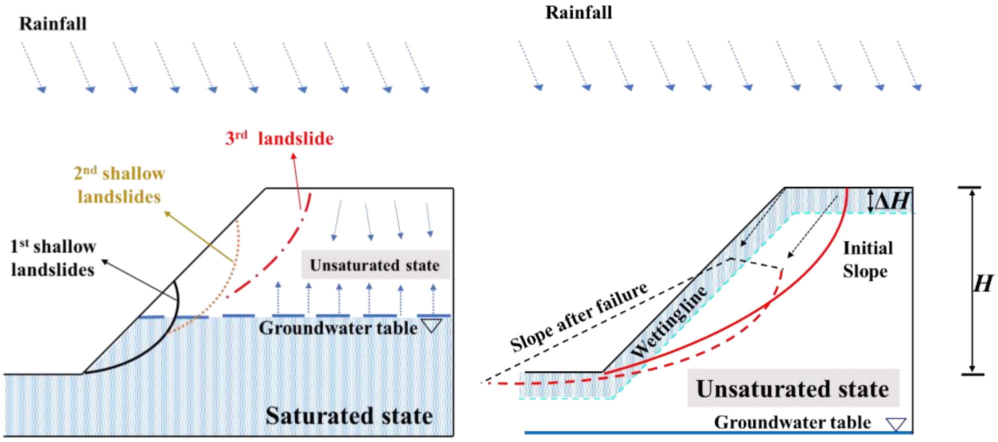

(a) Multiple shallow failures (b) Deep failure

Fig 2.1 Two typical failure modes: (a) Multiple shallow failures; (b) Deep failure

In order to simplify the analysis in the previous works, the slope is often considered to be completely dry or fully saturated (Utili 2013; Michalowski 2017). However, in nature, many slopes exist in an unsaturated state. In recent years, the stability analysis of unsaturated slopes has gradually become a hot topic of research. When analyzing unsaturated slopes, due to the existence of matric suction, the soil strength will be improved (Fredlund and Rahardjo, 1993). Therefore, the factor of safety of unsaturated slopes is higher than that of fully saturated slopes (Vahedifard et al. 2016; Li et al. 2018), but the dry condition will also present a higher estimated value than the actual situation. When considering the effects of rainfall conditions, along with the infiltration of rainwater above the wet front or the increase of groundwater table, the pore-water pressure of the slope will increase, and there will be some incremental increase in the soil moisture content inside the slope, which can affect the overall stability of the slope. Sandy slopes have been reported as shallow failures (Dai et al. 2003; Zizioli et al. 2013), which occurred form the slope toe and spread to the upon part along the slope surface. For this kind of failure, research always conducts the local factor of safety and find the most dangerous local areas based on the movement of the groundwater table. In fact, deep landslides are often found in nature, and this type of failure is often found in cohesive soil such as clay, silt and loose. And the disasters caused by deep landslides may produce more devastating disasters (Keaton et al. 2014).

The evaluation of dry slope has been discussed detailly (Chen et al. 1965), and when considering fully saturated soil slope, the effect of the pore-water pressure was normally assumed to be coefficient $\boldsymbol{r_u}$, as introduced by Bishop & Morgenstern (1960). Bigger $\boldsymbol{r_u}$ represents lagger pore-water pressure, which will lead to smaller factor of safety of the slope. For unsaturated slopes, the consideration of matric suction has become a focus. In order to express the shear strength characteristics of unsaturated soils, Fredlund et al (1978) proposed an extended Mohr-Coulomb criterion. And the relationship between the increase in shear strength and the increase of matric suction has been studied thoroughly by introducing another material variable φ_b. Fredlund and Rahardjo (1993) tested on various types of soil and they found that in most cases, φ_b is less than internal friction angle φ. However, the soil suction was often preset to be a certain value or linearly changes with infiltration depth. While the experimental results show that matric suction tends to change non-linearly along the infiltration depth matric suction tends to change non-linearly along the infiltration depth.

As mentioned above, the stability of unsaturated slopes in the previous study was only analyzed for a single state, but the dynamic change of slope stability during the rainfall process has been ignored. The purpose of this study is to develop an improved method that can obtain the stability of unsaturated slopes with different infiltration depths and different groundwater table. The result of this study was also confirmed with classic literature to ensure the correction. The factor of safety of slope under rainfall conditions can be calculated more realistic.

2.2 Stability analysis of slope under rainfall

2.2.1 Analysis of shallow failure mode-TRIGER

Field investigations and previous research have shown that sandy slopes are widespread in Japan, and the form of failure is typically characterized by multiple shallow landslides caused by infiltration of rainwater as well as rising groundwater table (Koizumi et al., 2018; Chueasamat et al., 2018). This study focuses on typical sandy soil slopes in Japan.

Previous studies have mostly focused on obtaining the $\boldsymbol{F}_{\mathrm{s}}$ under a single slip surface. However, this is not suitable for sandy soil slopes with multiple shallow landslides. As **Fig 2.2** shows, due to the increase of volumetric moisture content and the rise of the groundwater table due to the rainfall infiltration, the local factor of safety $\boldsymbol{F}_{\mathrm{s}}$ under different depths of the sandy slope is inconsistent. In order to evaluate the stability of slope during rainfall duration, the local factor of safety ($\boldsymbol{F}_{\mathrm{s}}$) has been calculated at different monitoring times. Although the classical method of infinite-slope stability analysis for rainfall-induced shallow landslide will present more unfavorable results than the actual situation, this model can also be extended to unsaturated conditions by considering the suction stress (Bordoni et al, 2015), in which shallow slope failure is controlled by an increase in pore water pressure owing to rainfall infiltration. The study combines the Brooks-Corey equation with soil suction and the process of rainfall infiltration, and ***F*s** was obtained by TRIGRS (Transient Rainfall Infiltration and Grid-Based Regional Slope-Stability) as:

$$F_s(Z,t)=\frac{\tan\varphi'}{\tan\beta}+\frac{c'-\sigma_s(Z,t)\tan\varphi'}{(\gamma+\gamma_w*w(Z,t))*Z*\sin\beta*\cos\beta} \tag{2.1}$$

Here *Z* refers to the depth below the ground surface (as shown in **Fig 2.3**), *t* is the measuring time, ***β*** (°) is the angle of slope, ***φ'*** (°) is the soil friction angle, while for unsaturated conditions, effective friction angle should include the range of variation (5° – 6°) and since sand is cohesionless soil, cohesion ***c'*** (kPa) is 0, ***γ*** (*N*/m^3) is the soil unit weight, γ_w (*N*/m^3) is the unit weight of groundwater, *w* is soil moisture content, and σ_s (kPa) defined by (Bishop and Morgenstern, 1960) for the saturated state (u_a-u_w<=0) and (Van Genuchten 1980; Griffiths and Lu 2005) for the unsaturated state (u_a-u_w > 0):

$$\begin{aligned}&\sigma^s=-(u_a-u_w) && (u_a-u_w)<=0\\ &\sigma^s=-(u_a-u_w)\left\{\frac{1}{1+[\alpha(u_a-u_w)]^n}\right\}^{1-1/n} && (u_a-u_w)>=0\end{aligned} \tag{2.2}$$

u_a is pore air pressure, which can be set as 0 in the calculation, u_w is pore water pressure, *a, n* are related parameters of soil water characteristic curves. For the saturated state, u_w can be obtained as

$$u_w=r_u\gamma z_1 \tag{2.3}$$

While for the unsaturated state, u_w can be obtained as:

$$u_w=\frac{1}{\alpha}\ln[(1+q/k_s)e^{(-\gamma_w\alpha z_1)}-q/k_s] \tag{2.4}$$

Here *q* is vertical specific discharge, the seepage state is negative, k_s is the saturated hydraulic conductivity, and z_1 is the net distance from the general point in the slope to the groundwater table, as shown in **Fig 2.3**, the monitoring point is in the opposite direction from the groundwater table under saturated state (Point A and B) and unsaturated state (Point C). $\boldsymbol{r_u}$ is the coefficient of pore water pressure, which can simplify the calculation of pore water pressure, but it presents an overestimation of the pore water in the part of hillslopes (Michalowski 2018). The coefficient $\boldsymbol{r_u}$ is usually assumed to be smaller than 0.6. The most unfavorable situation of $\boldsymbol{r_u}$ is considered in this study. As a result, the σ_s (kPa) used in this research can be described as:

$$\sigma^s = \begin{cases} r_u \gamma z_1 & (u_a - u_w) <= 0 \\ \dfrac{1}{\alpha} \dfrac{\ln[(1+q/k_s)e^{(-\gamma_w \alpha z_1)} - q/k_s]}{(1+\left\{-\ln[(1+q/k_s)e^{(-\gamma_w \alpha z_1)} - q/k_s]\right\}^n)^{1-1/n}} & (u_a - u_w) > 0 \end{cases} \tag{2.5}$$

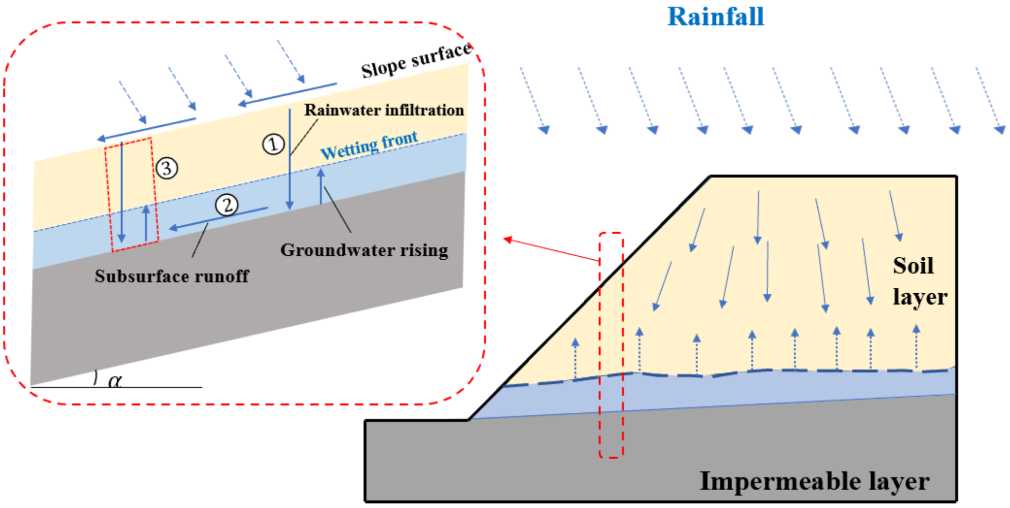

Fig 2.2 Typical shallow failure model

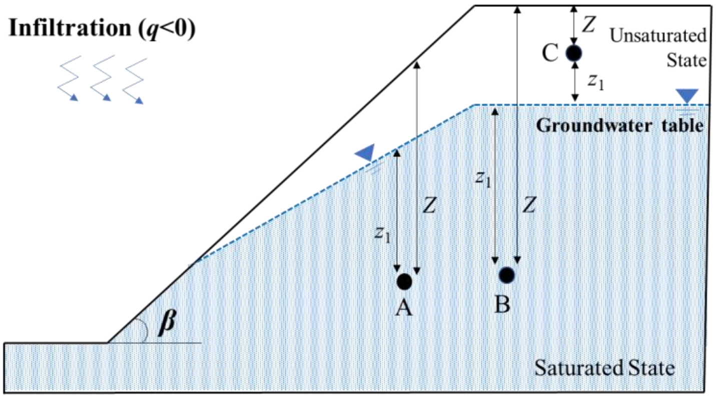

Fig 2.3 Water distribution in an unsaturated slope

2.2.2 Analysis of deep landslide by Limit analysis

Fig 2.4 shows the idealized distribution of pore water pressure in soil under rainfall conditions by Rahardjo et al. (1995). The upper part of the slope is in a saturated state due to rainfall infiltration, and the wetting front is the interface between the saturated and unsaturated regions. The unsaturated area continues up to the groundwater table and below the groundwater table, slope is also in a saturated state. Profile in **Fig 2.4** presents that the pore water pressures above and below the wetting front are diametrically opposite, and the upper pore water pressure is positive because the soil is saturated, which can be obtained by:

$$u_w = r_w * Z_w \tag{2.6}$$

Here r_w is the density of water. While below the wetting front, it is negative porewater pressure, which is also called matric suction and obtained by Equ. (2.4). According to the above derivation, the shear strength of the soil in the unsaturated area is:

$$\tau_f = c' + (\sigma - u_a)\tan\varphi' + c_{app} \tag{2.7}$$

Here σ-u_a is the net stress on the failure plane, c' is effective cohesion and φ' is the effective friction angle, c_{app} is apparent cohesion caused by negative porewater pressure in unsaturated areas that can be obtained by:

$$c_{app} = -\sigma^s \tan\varphi' \tag{2.8}$$

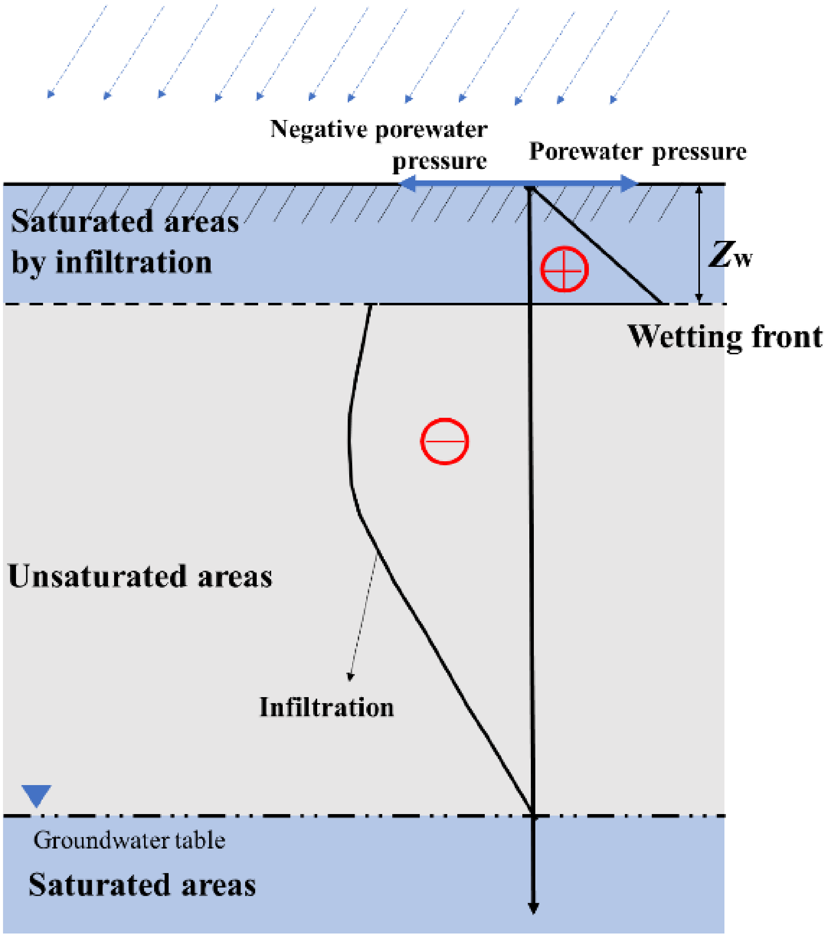

Fig 2.4 Profile of porewater pressure in residual soil (Modified from Rahardjo et al. 1995)

Based on rainfall infiltration and the profile of porewater pressure. It's easy to build the deep failure mode of the slope by limit analysis. Limit analysis is generally based on three assumptions: (1) Ideal plasticity assumption: the stress-strain curve is simplified to two connected straight lines, strain-softening phase in the curve is not considered; (2) The yield surface is convex, and the plastic strain of soil is calculated by yielding or thogonal rule calculation on the surface; (3) Small deformation assumption and virtual work equation. In the study, due to the continuous rainfall, it needs to assume uniform rainfall infiltration, that is, the distance Z_w between the wetting front and the surface of the slope is the same. The schematic diagram of the failure mechanism of slope with rainfall infiltration is shown in **Fig 2.5**. The log-spiral failure mechanism is defined as

$$r = r_0 \exp[(\theta - \theta_0)\tan\varphi] \tag{2.6}$$

where φ is the internal friction angle, and the length $O'A$ is the radius r_0 and θ_0 is the angle between $O'A$ and the horizontal plane. There is a depth of Z_w from the wetting front to the ground, which intersects the upper part of the sliding surface D, and the lower part E. θ_{w1} and θ_{w2} are angles of the radius $O'D$ and $O'E$ to the ground. All the figures are illustrated in **Fig 2.5 (a)**.

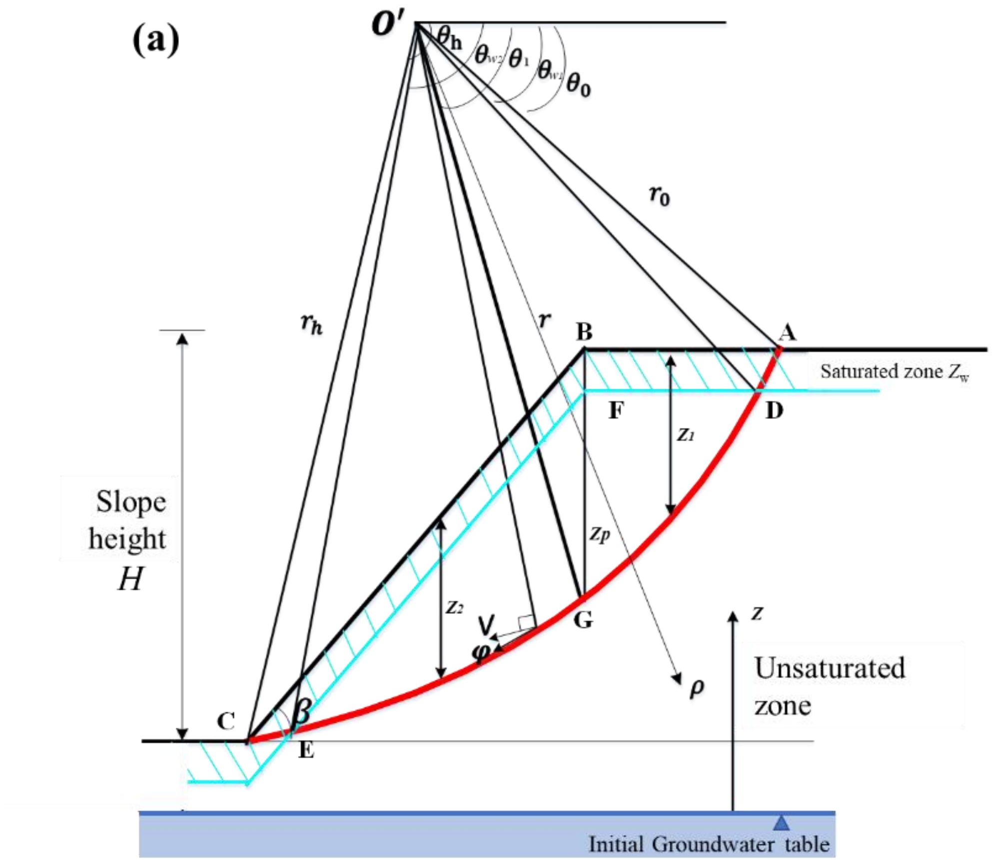

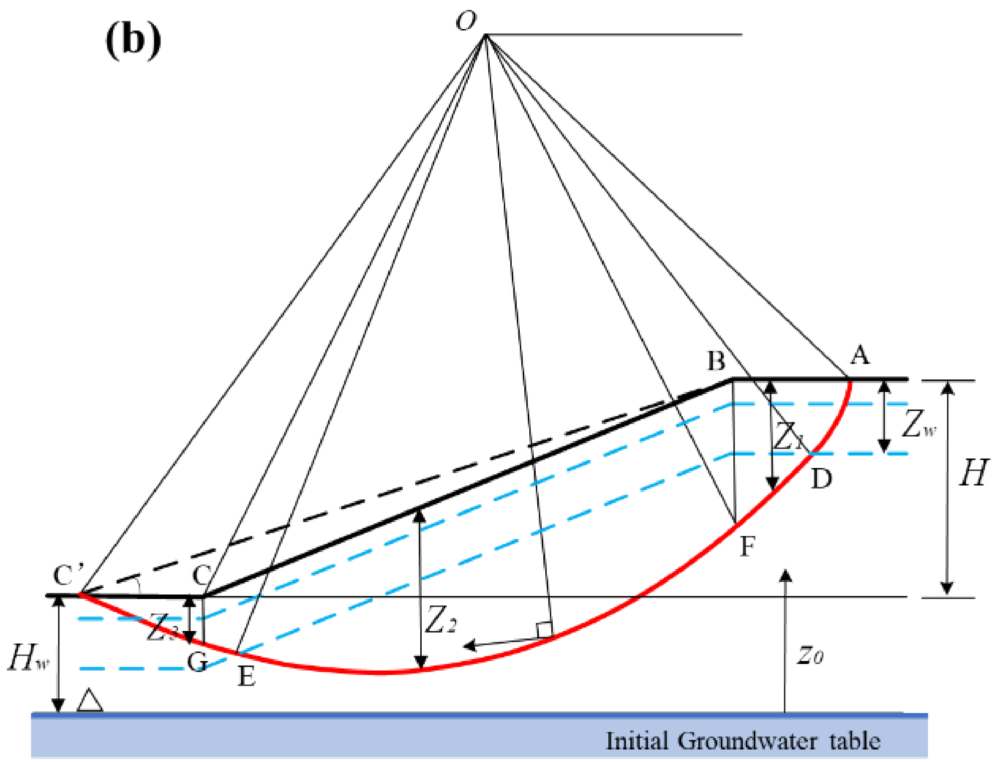

Fig 2.5 Failure mechanism with rainfall infiltration in the slope: (a) failure from slope toe; (b) failure below the slope toe

Based on the mechanism of failure mode in **Fig 2.5**, The kinematic method of limit analysis is an effective approach for the evaluation of unsaturated slope, and it is assumed that the slope keeps stable when the rate of internal energy dissipation is bigger than all of the external effects. As a result, the internal and external work rate balance is used to make the analysis of the critical state for unsaturated soil slope, the log-spiral upper bound limit analysis equation can be obtained as:

$$\dot{W}_r + \dot{W}_{u_w} = \dot{D}_c \tag{2.7}$$

Here W_r is the rate of external work by soil weight component, and the W_{u_w} is the external work by pore water pressure component. In this case, the block ABCA is used to calculate the soil weight work rate W_γ. Block ABCEFDA, with porewater pressure in the saturated areas, is considered to obtain the external work W_{u_w}. As **Fig 2.4** shows, internal energy dissipation is along the failure surface AC of logarithmic spiral shape, including the saturated part AD and CE, and the unsaturated part DE.

The factor of safety is the ratio of internal energy dissipation to external work:

$$F_s=(D_c+D_s)\ /(W_r+W_u-\ W_{u2}) \tag{2.8}$$

Here D_c is the energy dissipation of AC without any porewater pressure or matric suction, as shown below:

$$D_c=\frac{c'\omega r_0^2(e^{2(\theta_h-\theta_o)\tan\varphi}-1)}{2\tan\varphi} \tag{2.9}$$

ω is rotational angular acceleration in the failure process, D_s is the energy dissipation of DE with effects of matric suction:

$$D_s=\omega r_0^2 e^{2(\theta_{w1}-\theta_0)\tan\varphi}\int_{w_1}^{w_2} c_{app}e^{2(\theta-\theta_{w1})\tan\varphi}d\theta \tag{2.10}$$

Soil weight work rate W_r is：

$$w_r=\gamma\omega r_0^3(f_1-f_2-f_3-f_4) \tag{2.11}$$

γ is unit weight of soil and f_1 to f_4 in the formula are the energy dissipation of the blocks AOC′, AOB, BOC, and COC’ in **Fig 2.5 (b)** respectively, which can be obtained from (Chen 1965; Utili, 2013).

For the area with porewater pressure, research provides a scheme: the pore water pressure of the entire slip surface AC minus the pore water pressure of the unsaturated area DE as shown:

$$\begin{aligned} w_u=&r_u\gamma\omega r_0^2\tan\varphi(\int_{\theta_0}^{\theta_1} z_1\exp[2(\theta-\theta_0)\tan\varphi]d_\theta \\ &+\int_{\theta_1}^{\theta_2} z_2\exp[2(\theta-\theta_0)\tan\varphi]d_\theta+\int_{\theta_2}^{\theta_h} z_3\exp[2(\theta-\theta_0)\tan\varphi]d_\theta \end{aligned} \tag{2.12}$$

$$\begin{aligned} w_{u2}^2=&r_u\gamma\omega r_0^2\tan\varphi(\int_{\theta_{w1}}^{\theta_1}(z_1\text{-}z_w)\exp[2(\theta-\theta_0)\tan\varphi]d_\theta \\ &+\int_{\theta_1}^{\theta_{w2}}(z_2\text{-}z_w)\exp[2(\theta-\theta_0)\tan\varphi]d_\theta \end{aligned} \tag{2.13}$$

$$\begin{aligned} w_u^2 = {} & r_u \gamma \omega r_0^2 \tan\varphi \Big(\int_{\theta_{w1}}^{\theta_1} (z_1\text{-}z_w) \exp[2(\theta-\theta_0)\tan\varphi] d_\theta \\ & + \int_{\theta_1}^{\theta_2} (z_2\text{-}z_w) \exp[2(\theta-\theta_0)\tan\varphi] d_\theta + \int_{\theta_1}^{\theta_{w2}} (z_3\text{-}z_w) \exp[2(\theta-\theta_0)\tan\varphi] d_\theta \end{aligned} \tag{2.14}$$

Here r_u is coefficient of pore water pressure, generally set to 0.25, 0.5 or greater. Equ. (2.13) is the case that the logarithmic spiral shape crosses the slope toe and Equ. (2.14) is the case that the logarithmic spiral shape crosses below the slope toe. z_1 to z_3 is the distance from a point on the slip surface to the top of the slope respectively, which can be obtained by the following:

$$\begin{aligned} & \frac{z_1}{r_o} = \frac{r}{r_0}\sin\theta - \sin\theta_0 \\[2ex] & \frac{z_2}{r_o} = \frac{r}{r_0}\sin\theta - \sin\theta_h \exp[(\theta_h-\theta_0)\tan\varphi] + \\ & (\frac{r}{r_0}\cos\theta - \cos\theta_h \exp[(\theta_h-\theta_0)\tan\varphi])\tan\beta \\[2ex] & \frac{z_3}{r_o} = \frac{r}{r_0}\sin\theta - \sin\theta_h \exp[(\theta_h-\theta_0)\tan\varphi] \end{aligned} \tag{2.15}$$

For the unsaturated part: $\mathrm{z} = H + H_{wt} + r_0 \sin\theta_0 - r\sin\theta$. Based on the discussion above, the factor of safety depends on soil properties: ***c*, *γ*, *φ*, *a*, *n*, *k*s**; slope geometry: ***β*, *H***, water flow: ***q*, *H*w/*H***; rainfall intensity: ***Z*w/*Z*** (from 0% to 100 %, where 0% means that all are in a unsaturated state, and 100% means that all are in a saturated state). Research on the use of sequential quadratic optimization method (***SQP - Fmincon***) under Matlab to search for the factor of safety ***F*s.**

2.3 Results of unsaturated slope under rainfall

The study calculates the factor of safety ***F*s** for two analysis methods under different types of soil layers. The sandy slope mainly gives the F_s of the slope under the movement of the groundwater table, and the cohesive soil gives the ***F*s** under different infiltration depths.

2.3.1 Result of shallow failure by upward of groundwater table

In Lu and Godt (2008), the study analyzed seepage conditions for infinite slopes, and conducts case calculations for sand, clay, loess, etc. This research conducted the same analysis as the previous study and considered different kinds the sand soil (Coarse sand, Medium sand and Fine sand) to obtain the factor of safety. The hydrologic and shear strength properties of the three sand are shown in **Table 2.1** and three different slope angle (***β***) is considered in this research.

Table 2.1 Parameters of three different sand soil considered in this research

Parameter	**Symbol**	**Coarse sand**	**Medium sand**	**Fine sand**
Soil cohesion	c' / kPa	0	0	0
Internal friction angle	φ / °	40	40	40
Soil unit weight	γ / kNm^{-3}	14 to 18	14 to 18	14 to 18
Slope angle	β / °	30, 40 and 50	30, 40 and 50	30, 40 and 50
Initial volumetric moisture content	w / %	18	18	18
Inverse of the air entry pressure	a / kPa^{-1}	0.45	0.14	0.08
Pore size distribution	n	7.5	5.5	4.75
Vertical specific discharge	q / ms^{-1}	$-3.14*10^{-8}$	$-3.14*10^{-8}$	$-3.14*10^{-8}$
Saturated hydraulic conductivity	k_s / ms^{-1}	$1*10^{-6}$	$1*10^{-6}$	$1*10^{-6}$
Variation in friction angle	$\Delta\varphi$ / °	6	6	6

As shown in **Table 2.1**, Research was conducted in three different sand soil and three different slope angle (30°, 40 ° and 50 °). **Fig 2.6** shows the schematic diagram of shallow failure calculation. Above the groundwater table (positive value) is unsaturated state, and below the groundwater table (negative value) is the saturated state. **Fig 2.7** presents three types of sandy slope factors of safety charts. It can be clearly seen that when the groundwater table is lower than 0, the factor of safety decreases rapidly due to the influence of pore water pressure. Due to the nonlinear distribution of matric suction, the obtained factor of safety also exhibits nonlinear variation characteristics. It can be seen that the maximum value of the factor of safety appears at a distance of 0.5-1.5m above the groundwater table, then a longer distance leads to a reduction of the factor of safety and eventually tends to a stable state. Compare with the other two sand soil, fine sand presents better stability characteristics. The maximum factor of safety is increased by about 20% compared with coarse sand and around 10% compared with medium sand. But in areas much higher than the groundwater table (above 4 meters) or below the groundwater level, the factor of safety of different sand slopes is almost the same. Another well-understood phenomenon is that a higher slope angle will result in a lower F_s.

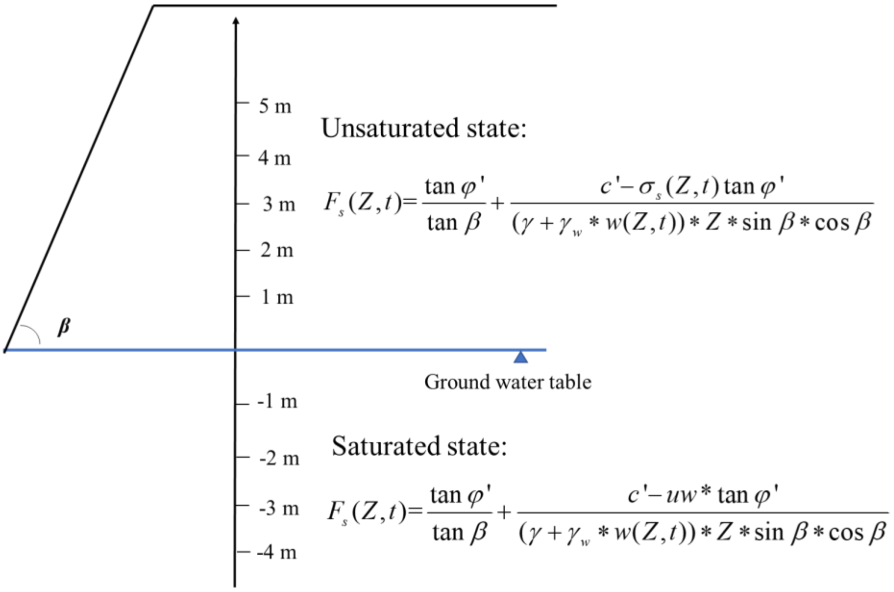

Fig 2.6 Schematic diagram of shallow failure calculation

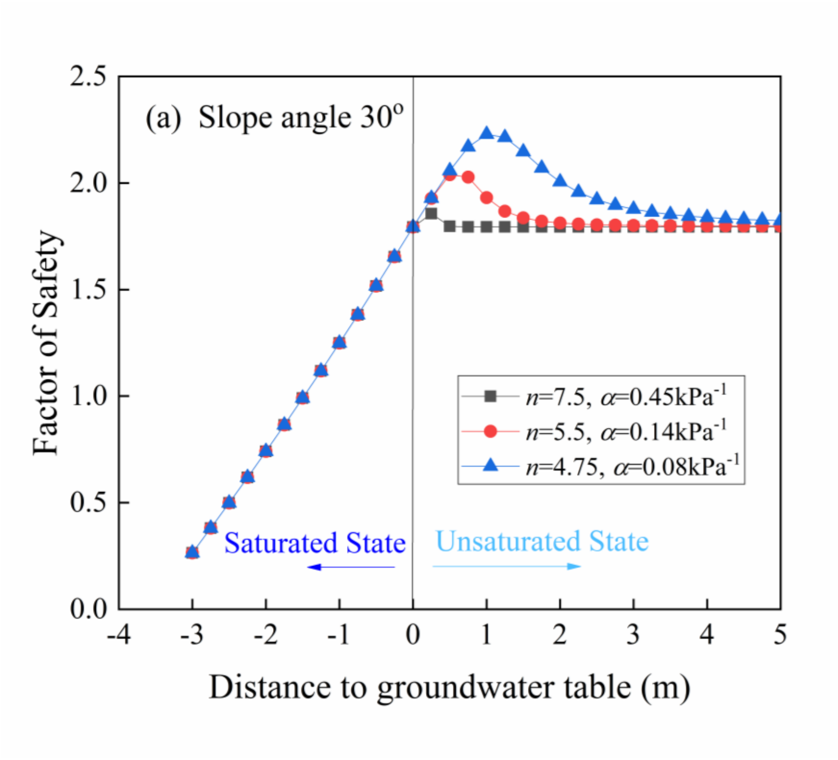
(a) Slope angle 30°
Factor of Safety
Distance to groundwater table (m)
2.5
2.0
1.5
1.0
0.5
0.0
-4
-3
-2
-1
0
1
2
3
4
5
n=7.5, α=0.45kPa-1
n=5.5, α=0.14kPa-1
n=4.75, α=0.08kPa-1
Saturated State
Unsaturated State

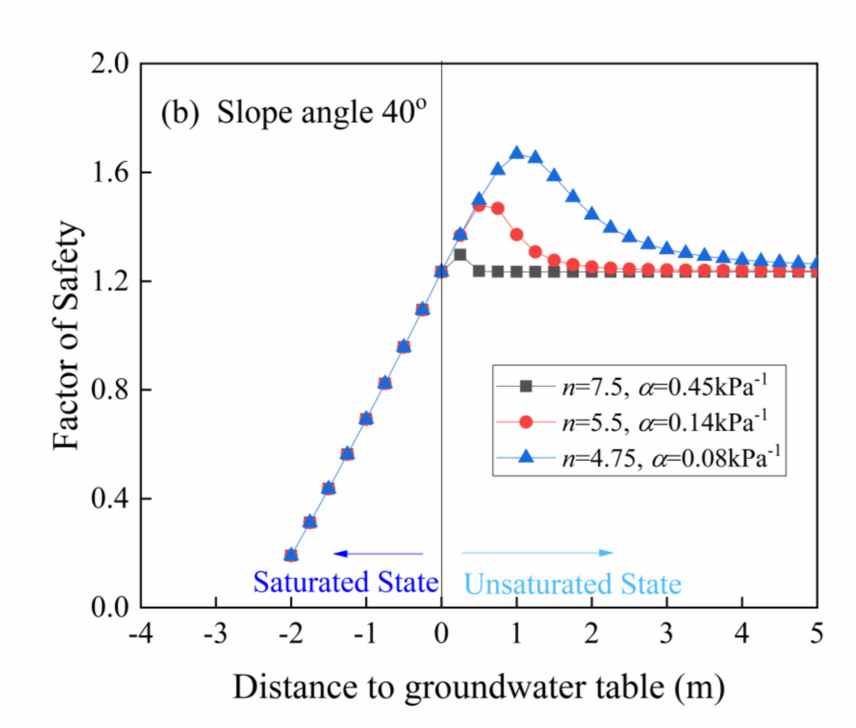
(b) Slope angle 40°
Factor of Safety
Distance to groundwater table (m)
2.0
1.6
1.2
0.8
0.4
0.0
-4
-3
-2
-1
0
1
2
3
4
5
n=7.5, α=0.45kPa-1
n=5.5, α=0.14kPa-1
n=4.75, α=0.08kPa-1
Saturated State
Unsaturated State

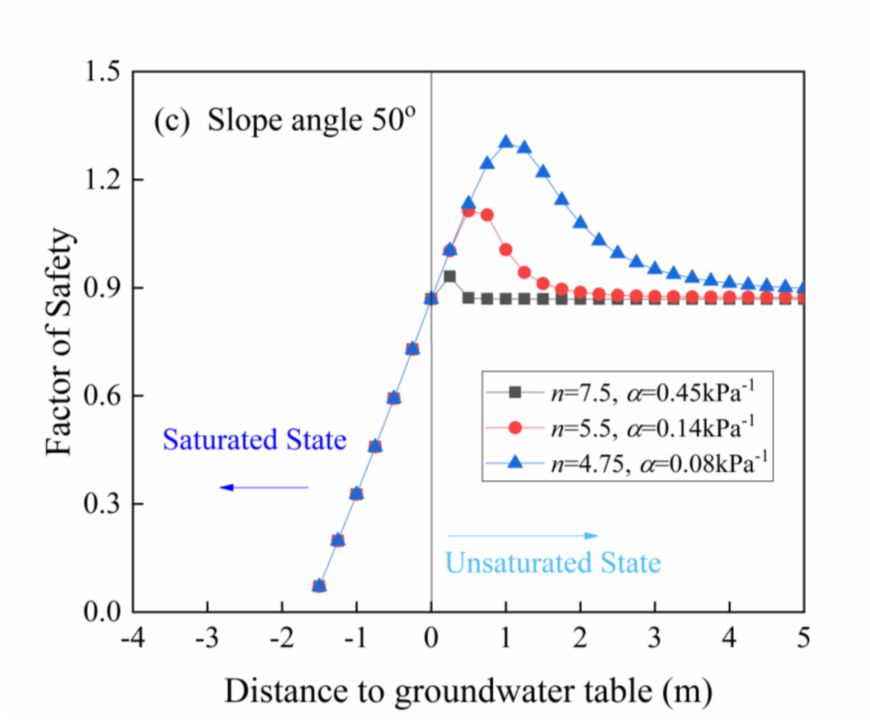

Fig 2.7 Three types of sandy slope factor of safety charts: (a) β=30°, (b) β=40 ° and (c) β=50 °

2.3.2 Result of deep failure under different infiltration depths

Bofore conducting the analysis of unsaturated slope under rainfall. Research needs to verify the correctness of results from imit analysis method. Based on the failure mode of 2D log-spiral, research from Vahedifard et al. (2016) presents the required cohesion (in **kPa**) to keep the unsaturated slope in a critical state, and their method is based on the equilibrium of moments. Li et al. (2018) also conducted 3D analysis of the unsaturated slope, and check the 2D results with the parameters of slope angle $\boldsymbol{\beta}$ = 90°, slope height $\boldsymbol{H}$ = 5 m and soil weight $\boldsymbol{\gamma}$ = 20 kN/m^3. For comparison of the result, this study also carried out the analysis when rainfall infiltration $\boldsymbol{Z_w/Z_p}$ =0 based on the same parameters. As **Table 2.2** shows, the results of the current study are the same as the previous study by Vahedifard et al. (2016) and Li et al. (2018), which strongly confirms the correctness of formula derivation and numerical calculation.

Table 2.2 Results comparasion with the previous study by Vahedifard et al. (2016) and Li et al. (2018) under β=90°, γ=20 kN/m^3, z_0=0m, H=5m

Soil types	φ	n	a	Source of results	No suction	q= −3.14×10^{-8}m/s	No flow q=0	q=1.15×10^{-8}m/s
Clay	20°	2	0.005	Vahedifard et al. (2016)	18.2	15.3	10.1	8.2
				Li et al. (2018)	18.2	15.2	9.9	8.0
				This study	**18.2**	**15.25**	**10.1**	**7.90**
Silt	25°	3	0.01	Vahedifard et al. (2016)	16.5	7.0	6.4	6.1
				Li et al. (2018)	16.5	6.9	6.2	5.9
				This study	**16.5**	**6.85**	**6.36**	**6.10**
Loess	28°	4	0,025	Vahedifard et al. (2016)	15.6	6.8	6.7	6.7
				Li et al. (2018)	15.6	6.7	6.7	6.6
				This study	**15.6**	**6.77**	**6.71**	**6.70**
Sand	30°	5	0.1	Vahedifard et al. (2016)	15.0	13.9	13.9	13.9
				Li et al. (2018)	15.0	13.9	13.9	13.9
				This study	**15.0**	**13.86**	**13.88**	**13.87**

Taking the parameters in **Table 2.2** of the four soil samples as an example, considering the parameters of $\boldsymbol{\beta}=90^{\circ}$, $\boldsymbol{\varphi}=30^{\circ}$, $\boldsymbol{\gamma}=20$ kN/m^3, $\boldsymbol{c}=20$ kPa, $\boldsymbol{z_0}=0$ m, $\boldsymbol{H}=5$ m, and research assumes the hydrostatic pressure coefficients are $r_{\mathrm{u}}=0.25$ and $r_{\mathrm{u}}=0.5$ respectively. $Z_{\mathrm{w}}/Z_{\mathrm{H}}$ varies from 0% to 100% presents the degree of rainfall infiltration, where 0% means all are in an unsaturated state, 100% means all in a saturated state, and from 0% to 100% means the slope reaches saturation from top to bottom areas.

Fig 2.8 shows the factor of safety of the cohesive soil under different rainfall infiltration considering the pore-water pressure coefficient $\boldsymbol{r_{\mathrm{u}}}=0.25$ and $\boldsymbol{r_{\mathrm{u}}}=0.5$. It is clear that a larger pore water pressure coefficient would lead to a more unfavorable condition for the slope. Clay presents the lowest safety factor. Loess and Silt show better stability. According to the research in the previous section, the sandy slopes are mostly perform shallow failures, so the following part of this study will not be carried out for the sandy slopes. The stability of the other three soils in the unsaturated state and under rainfall conditions was analyzed.

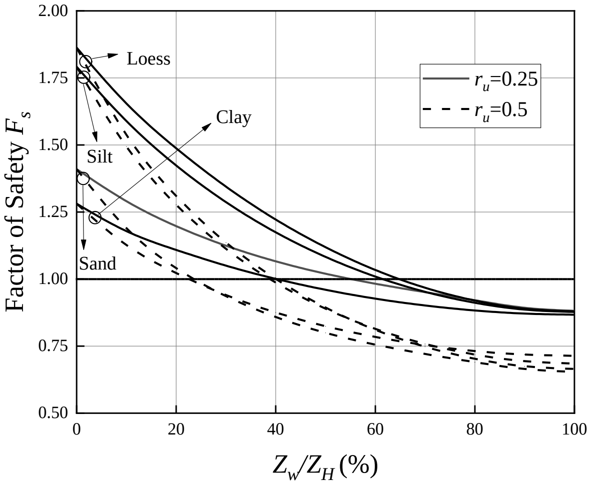

Fig 2.8 Factor of Safety of cohesive soil under different rainfall infiltration

Fig 2.9 shows $\boldsymbol{F_{\mathrm{s}}}$ of cohesive soil under different unsaturated flow conditions, research considers four different flow conditions: infiltration, no flow, evaporation and no-suction. The case of no-suction means that research doesn't consider the effects of suction stress in the slope, which is the same condition as the classic results. For the case of infiltration, rainwater will infiltrate into the unsaturated part. The value of infiltration ($q = -3.14\times10^{-8}$), no-flow ($q = 0$) and evaporation ($q = 1.15\times10^{-8}$) in the formula to obtain the **F_s**. The research results show that no matter what kind of soil it is, the factor of safety **F_s**, when the suction is not considered, is always smaller than that when considering the effects of the suction, and it is also confirmed that the stability of the slope will be improved under the suction. Different seepage states in Clay have a significant impact on the factor of safety. In the initial stage, the **F_s** gradually decreases from evaporation, no-flow to infiltration. However, with the continuous increase of rainfall infiltration, the influence of different infiltration states on the factor of safety **F_s** gradually decreases.

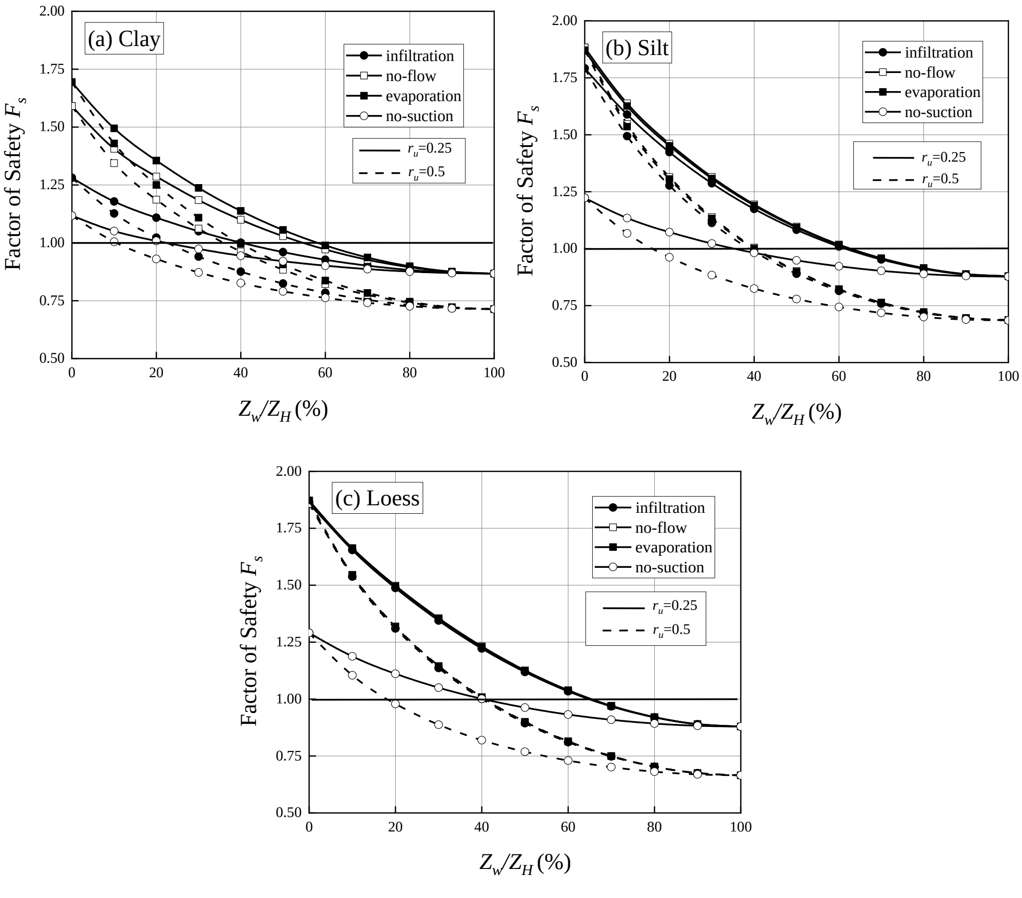

Fig 2.9 Factor of Safety of cohesive soil under different unsaturated flow conditions: (a) Clay; (b) Silt; (c) Loess

Research also conducted the stability analysis of slope under different rainfall infiltration and soil types considering the effects of slope angle and firction angle. **Fig 2.10** shows the Factor of Safety $\boldsymbol{F}_{s}$ of cohesive soil under different internal friction angle $\boldsymbol{\varphi}$, the internal friction angle $\boldsymbol{\varphi}$ of 15°, 20°, 25°, 30°, 35° and 40° was used to calculate the $\boldsymbol{F}_{s}$ and **Fig 2.11** presents Factor of Safety $\boldsymbol{F}_{s}$ of cohesive soil under different slope angle. The slope angle of 45°, 60°, 75° and 90° are taken into consideration in the analysis. Obviously, a larger internal friction angle will increase the stability of the slope, while a higher slope angle will lead to a lower factor of safety $\boldsymbol{F}_{s}$.

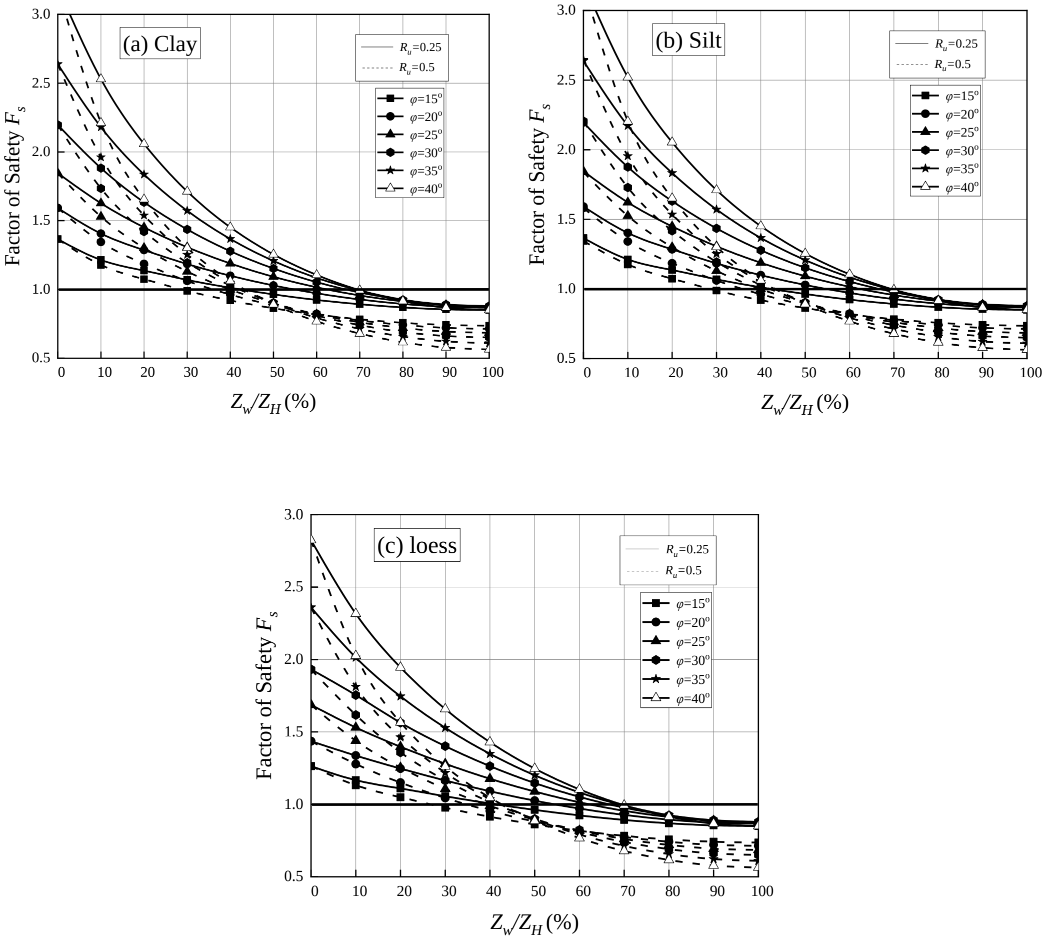

Fig 2.10 Factor of Safety of cohesive soil under different firction angle: (a) Clay; (b) Silt; (c) Loess

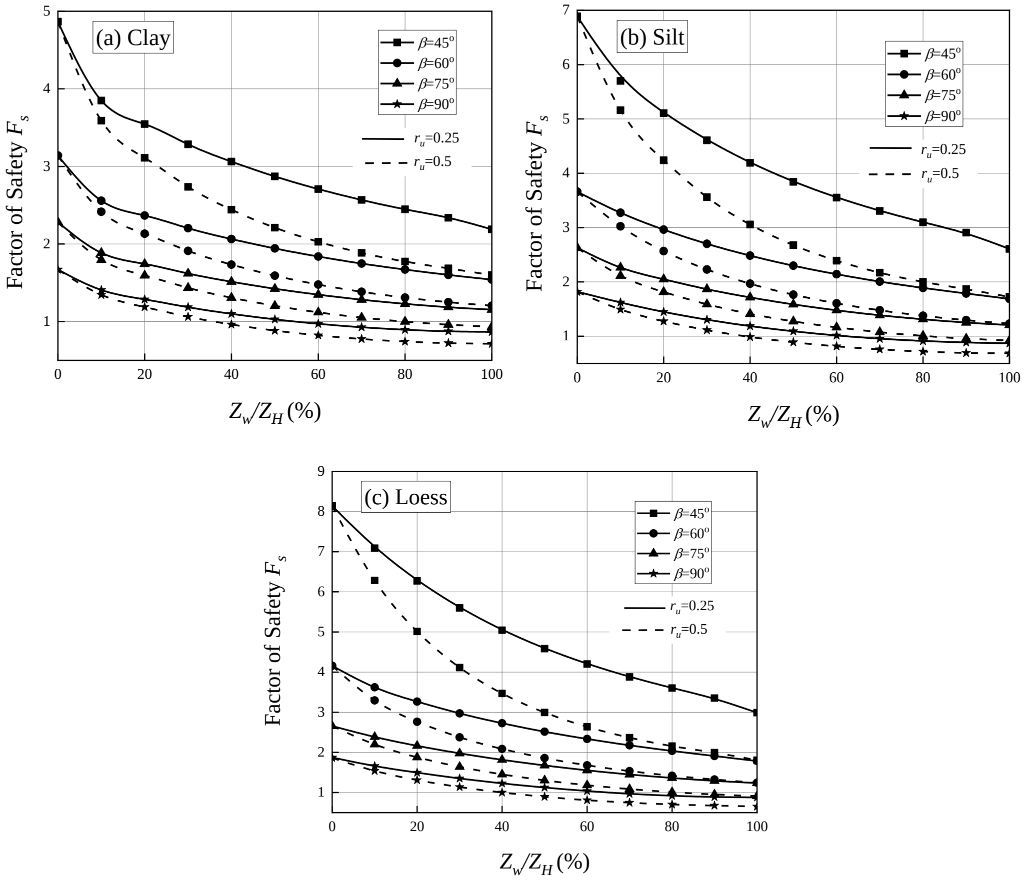

Fig 2.11 Factor of Safety of cohesive soil under different slope angle: (a) Clay; (b) Silt; (c) Loess

To peform the critical state of the unsaturated slope under rainfall infiltration, research selects one case as the example. **Fig 2.12** shows the critical state ($F_s = 1.00$) of the unsaturated slope under rainfall infiltrationwith two pore water pressure coefficient **r_u** = 0.25 and **r_u** = 0.5. It can be seen clearly that bigger pore water pressure coefficient will promote the occurrence of landslides faster. For the case of **r_u** = 0.25, critical state (**F_s** = 1.00) will appear when $Z_w/Z_H = 0.55$, while for the case of **r_u** = 0.5, critical state (F_s = 1.00) will appear when $Z_w/Z_H = 0.23$. Beyond these two depths, the **F_s** will be lower than 1.00, and the entire slope will be in an extremely dangerous state. The Stability factor (**N_s** = $\gamma H/c$) of the slope when in the fully saturated state ($Z_w/Z_H = 0.23$) in the research has also been calculated and compared the result with classic results by Michalowski (2017), result shows that the calculation results of the saturated slope are basically the same: when r_u=0.25, Stability factor N_s is 4.39351 by data from Michalowski (2017) and N_s = 4.401 in this research. When r_u=0.5, Stability factor N_s is 3.306 by data from Michalowski (2017) and N_s = 3.28 in this research. The consistency of the verification results once again reflects the accuracy of the calculation results.

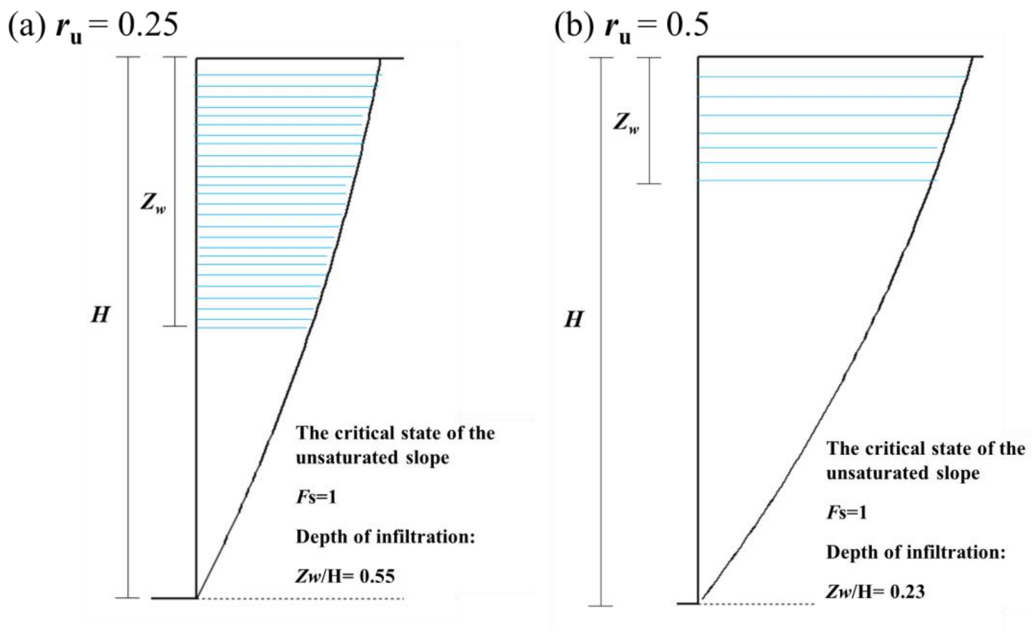

Fig 2.12 Critical state (F_s = 1.00) of the unsaturated slope under rainfall infiltrationwith of two pore water pressure coefficient: (a) r_u = 0.25; (b) r_u = 0.5

2.4 Conclusion of this chapter

In this chapter, research divides two forms of slope failure considering the influence of rainfall. One is the shallow slope failure caused by the rise of the groundwater table from the bottom to up, and the other is the deep slope failure caused by the saturated state from the upon to the bottom. This chapter also trys to develop an improved method that can obtain the stability of unsaturated slopes with different infiltration depths and different groundwater table. The conclusions of this chapter can be drawed as below:

(1) For the case of cohesionless soil, research presents an analytical framework

for evaluating the local safety factor of slopes under all possible groundwater table conditions. When the monitoring point is below groundwater table, $\boldsymbol{F}_s$ decreases rapidly due to the influence of pore water pressure. In the terms of the monitoring area above the groundwater table, the maximum value of the factor of safety appears at a distance of 0.5-1.5m above the groundwater table, then a longer distance leads to a reduction of the factor of safety and eventually tends to a stable state. The maximum $\boldsymbol{F}_s$ of fine sand is increased by about 20% compared with coarse sand and around 10% compared with medium sand. But in areas much higher than the groundwater table (above 4 meters) or below the groundwater level, the factor of safety of different sand slopes is almost the same.

(2) For the case of cohesive soil, upper bound limit analysis has been used to obtain the $\boldsymbol{F}_s$, which considers that the upper region is saturated due to rainfall infiltration, and the lower region remains unsaturated. A larger pore water pressure coefficient would lead to a more unfavorable condition for the slope. Clay presents the lowest safety factor. Loess and Silt show better stability. Comparing the calculation results of different parameters can be found that a larger internal friction angle will increase the stability of the slope, while a higher slope angle will lead to a lower factor of safety $\boldsymbol{F}_s$. Different seepage states in soil have a significant impact on the factor of safety. In the initial stage, the $\boldsymbol{F}_s$ gradually decreases from evaporation, no-flow to infiltration. However, with the continuous increase of rainfall infiltration, the influence of different infiltration states on the factor of safety $\boldsymbol{F}_s$ gradually disappears.

Reference

Bishop, A. W., & Morgenstern, N. (1960). Stability coefficients for earth slopes. Geotechnique, 10(4), 129-153.

Cogan J., Gratchev I. (2019). A study on the effect of rainfall and slope characteristics on landslide initiation by means of flume tests. Landslides, 16(12): 2369-2379

Dai C., Li W., Wang D., et al. 2021. Active Landslide Detection Based on Sentinel-1 Data and InSAR Technology in Zhouqu County, Gansu Province, Northwest China. Journal of Earth

Science, 32(5): 1092-1103.

Fredlund, D. G., & Rahardjo, H. (1993). Soil mechanics for unsaturated soils. John Wiley & Sons.

Fredlund, D. G., Morgenstern, N. R., & Widger, R. A. (1978). The shear strength of unsaturated soils. Canadian Geotechnical Journal, 15(3), 313-321.

Geotech J 55(4):477–485. https ://doi.org/10.1139/cgj-2017-0041

Griffiths, D. V., & Lu, N. (2005). Unsaturated slope stability analysis with steady infiltration or evaporation using elasto-plastic finite elements. International journal for numerical and analytical methods in geomechanics, 29(3), 249-267.

Huang, W., Leong, E. C., & Rahardjo, H. (2018). Upper-bound limit analysis of unsaturated soil slopes under rainfall. Journal of Geotechnical and Geoenvironmental Engineering, 144(9), 04018066.

Keaton, J. R., J. Wartman, S. Anderson, J. Benoît, J. deLaChapelle, R. Gilbert, and D. R. Montgomery. (2014). The 22 March 2014 Oso Landslide, Snohomish County, Washington. Arlington, VA: Geotechnical Extreme Event Reconnaissance (GEER), National Science Foundation

Li, Z. W., & Yang, X. L. (2018a). Stability of 3D slope under steady unsaturated flow condition. Engineering geology, 242, 150-159.

Li, Z. W., & Yang, X. L. (2018b). Active earth pressure for soils with tension cracks under steady unsaturated flow conditions. Canadian Geotechnical Journal, 55(12), 1850-1859.

Lu, N., & Godt, J. (2008). Infinite slope stability under steady unsaturated seepage conditions. Water Resources Research, 44(11).

Lu, N., & Likos, W. J. (2006). Suction stress characteristic curve for unsaturated soil. Journal of geotechnical and geoenvironmental engineering, 132(2), 131-142.

Michalowski RL (2018) Failure potential of infinite slopes in bonded soils with tensile strength cut-off. Can

Michalowski, R. L. (1995). Slope stability analysis: a kinematical approach. Geotechnique, 45(2), 283-293.

Michalowski, R. L. (2017). Stability of intact slopes with tensile strength cut-off. Géotechnique, 67(8), 720-727.

Rahardjo, H., Lim, T. T., Chang, M. F., & Fredlund, D. G. (1995). Shear-strength characteristics of a residual soil. Canadian Geotechnical Journal, 32(1), 60-77.

Rawls, W. J., Brakensiek, D. L., & Miller, N. (1983). Green-Ampt infiltration parameters from soils data. Journal of hydraulic engineering, 109(1), 62-70.

Utili, S. (2013). Investigation by limit analysis on the stability of slopes with cracks. Geotechnique, 63(2), 140-154.

Vahedifard, F., Leshchinsky, D., Mortezaei, K., & Lu, N. (2016). Effective stress-based limit-equilibrium analysis for homogeneous unsaturated slopes. International Journal of Geomechanics, 16(6), D4016003.

Van Genuchten, M. T. (1980). A closed-form equation for predicting the hydraulic conductivity of unsaturated soils. Soil science society of America journal, 44(5), 892-898.

Wang, F., Dai, Z., Takahashi, I., & Tanida, Y. (2020). Soil moisture response to water infiltration in a 1-D slope soil column model. Engineering Geology, 267, 105482.

Wei, Z. L., Wang, D. F., Sun, H. Y., & Yan, X. (2020). Comparison of a physical model and phenomenological model to forecast groundwater levels in a rainfall-induced deep-seated landslide. Journal of Hydrology, 586, 124894.

Zizioli, D., Meisina, C., Valentino, R., & Montrasio, L. (2013). Comparison between different approaches to modeling shallow landslide susceptibility: a case history in Oltrepo Pavese, Northern Italy. *Natural Hazards and Earth System Sciences*, *13*(3), 559-573.

CHAPTER 3

3. DEVELOPMENT OF IOT-BASED EWS

3.1 Introduction

The newly developed EWS can be divided into two basic components: System software configuration and equipment configuration. As **Fig 3.1** shows, for software aspect, it is mainly about data transmission and processing by IoT. For equipment aspect, a series of low-power consumption sensors have been selected, they were monitored and transferred by capture server and obtained the power sources from off-grid solar photovoltaic system.

As mentioned before, IoT devices are very dependent on network signals, i.e. a wifi system is usually assumed next to the monitoring system. However, these systems require wired internet or Wi-Fi to transmit data from sensors to a complex network of servers, which are costly and consume a lot of energy. Therefore, there is a need to develop a new integrated real-time data-driven monitoring system that can handle "instantaneous data”. In addition, transmitting recorded data through Wi-Fi or cellular networks is not feasible in many mountainous and underpopulated areas. Furthermore, analyzing the data accumulated in the sensor networks on a cloud server places an excessive load on the network.

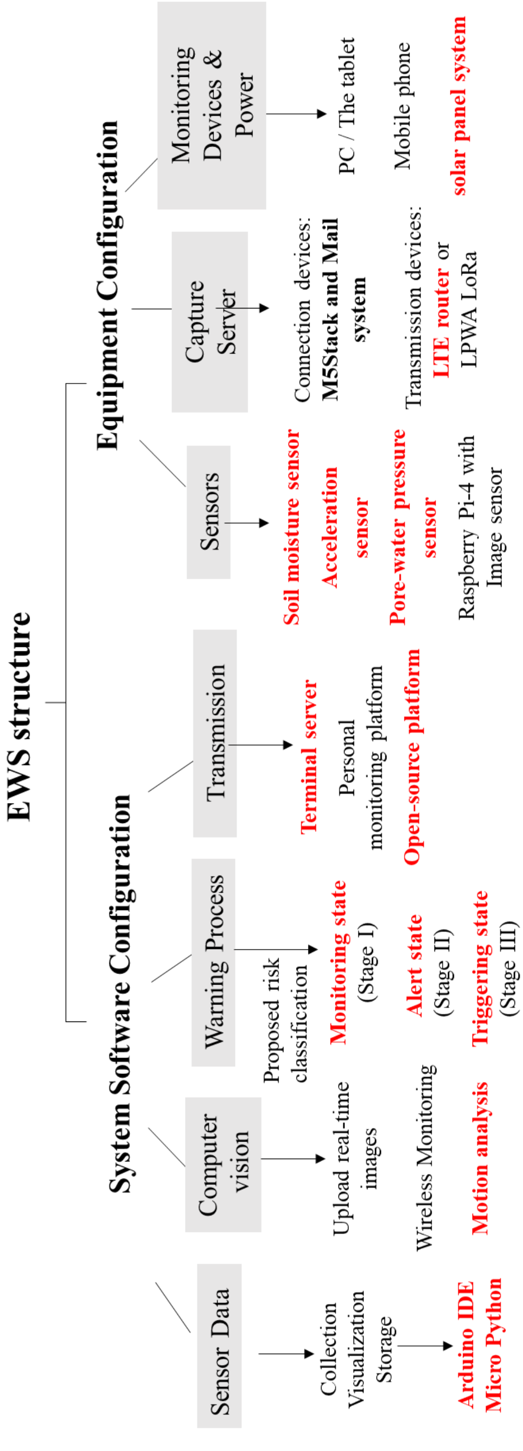

Fig 3.1 Architecture of EWS

3.2 Architecture of the System

3.2.1 Data acquisition of the EWS

Regarding the part of data acquisition, this study conducted the development of sensing devices based on IoT to complete the work of collecting and transmitting data from the monitoring objects. This section contains not only IoT-based hardware devices (sensors and IoT boards) but also IoT networks. As for the equipment part, the selection principle is ultra-low power consumption, cost-effective and easy deployment. For the utilization of wireless communication technology, it is first necessary to adapt to the functional requirements of the **EWS** (usually the total amount of data collection and data transmission rate). At the same time, the system needs to ensure the applicability and access permission of infrastructure, and control operating costs. Taking into account the economic benefits and the application of IoT, sensors in this EWS are:

(1) Soil moisture sensor (SEN0193, DFRobot): this product was used to measure the soil moisture content and obtained the moisture distribution in the slope. The sensor includes an on-board voltage regulator which gives it an operating voltage range of 3.3 to 5.5V. It is compatible with low-voltage MCUs (both 3.3V and 5V) and the weight of each sensor is only 15g.

(2) Pore water pressure sensor (KPG PA): this micromodule equipment was chosen to measure the porewater pressure and got the water level by rainwater infiltration. The sensor needs to be connected to handle data logger, but data can be transmitted to the cloud by mail system. The diameter of the sensor is only 10 mm and the weight of each sensor is 50g.

(3) Accelerometer sensors (MPU 6886): accelerometer sensors were arranged to measure the movement of soil, even some small deformation with the accuracy of 0.01^{o}. We found that it has been the smallest 9-axis Motion Tracking device currently on the market and this product incorporates the latest design innovations,

which enables the device to significantly reduce chip size and power consumption, further improving performance and reducing costs. The acceleration sensor that can replace the expensive displacement sensor in the EWS.

(4) Image sensors (Sony IMX219PQ CMOS) plugged into the Raspberry Pi-4 were used to capture real-time image or videos in the monitoring area. Raspberry Pi-4 is an ultra-compact computer which is suitable for many kinds of situations. To develop more functions, it can be connected with external sensors, such as computer vision, voice recognition and other industries. Image Sensors are supported by Raspberry Pi-4. Still image resolution of the sensor is 3280*2464 pixels, it also supports video of 1080p30, 720p60 and 640*480p60/90. The device combination has the advantages of low power consumption, portability, low price, and good performance.

All figures of sensor are shown in **Fig 3.2**. **Table 3.1** present the details of the equipment used in the EWS, it's obvious that this research selects the relatively lightweight and portable sensors on the market based on good accuracy and adaptability. So, whether considering the cost of sensors or the cost of transportation and installation, the current EWS is very cost-effective. Compared with the price of the some equipment provided in (Gamperl et al., 2021), the entire system can even be put into use for one tenth of the cost.

The capture server is comprised sensor connection devices and Internet connection devices. For the measuring areas, LTE devices can be chosen to provide wireless 4G or network port to the Raspberry Pi and communication devices (M5Stack and Handheld data logger with DMA-ESL). The connection between communication devices and sensors can be facilitated by 2.4-GHz low energy with a theoretical maximum range of 100 m. As all the data can be sent to cloud, it's easy to check by many portable devices, such as mobile phone, PC and Table. **Fig 3.3** shows the communication device in the data acquisition of EWS.

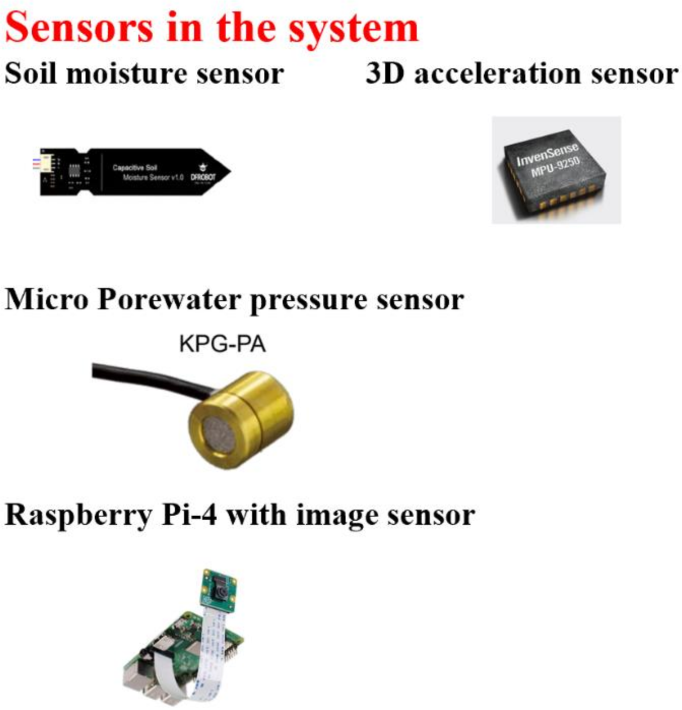

Fig 3.2 Sensors used in the EWS

Fig 3.3 Communication configuration in the system

Table 3.1 Device information of early warning system

Device	Type	Each Size	Each Weight	Operating Voltage	Power consumption
Soil moisture Sensor	SEN0193	90*25*5mm	15g	3.5V	---
Porewater pressure sensor	KPG PA	*Φ*8.7mm	25g	2V	---
Acceleration sensor	MPU9250	13x11mm	0.45g	2.4-3.6V	---
Raspberry pi with image sensor	Pi 4	175x145x9.5mm	550g	5.1V	2.2 W
IoT boards	M5Stack	54x54x18mm	50g	5V	1.62 W
Handheld data logger with wireless mail IoT	DMA-ESL	250*150*20mm	1000g	12V	10 W
Mobile router	Aterm MP02LN	45*90*10mm	150g	3.8V	2 W

3.2.2 Data transmission of the EWS

In terms of data transmission, WIFI communication methods are usually used, which is based on WIFI system like 4G or 5G, and it needs Network Station. For areas with stable network signals, the research will use M5stack IoT devices to connect various sensors, and use wifi to transmit data to the cloud. The schematic diagram of the specific connection is as follows in **Fig 3.4**. One M5stack IoT can be connected with two soil moisture sensors and one acceleration sensor. Mail system will also be used to transfer the real-time data of porewater pressure sensors to the cloud. For areas where the network signal is unstable or there is no communication station, the research will use the LoRa-IoT device based on LPWA transmission to connect various sensors. Research is dedicated to solving the problem that pore water pressure sensors need to rely on data loggers.

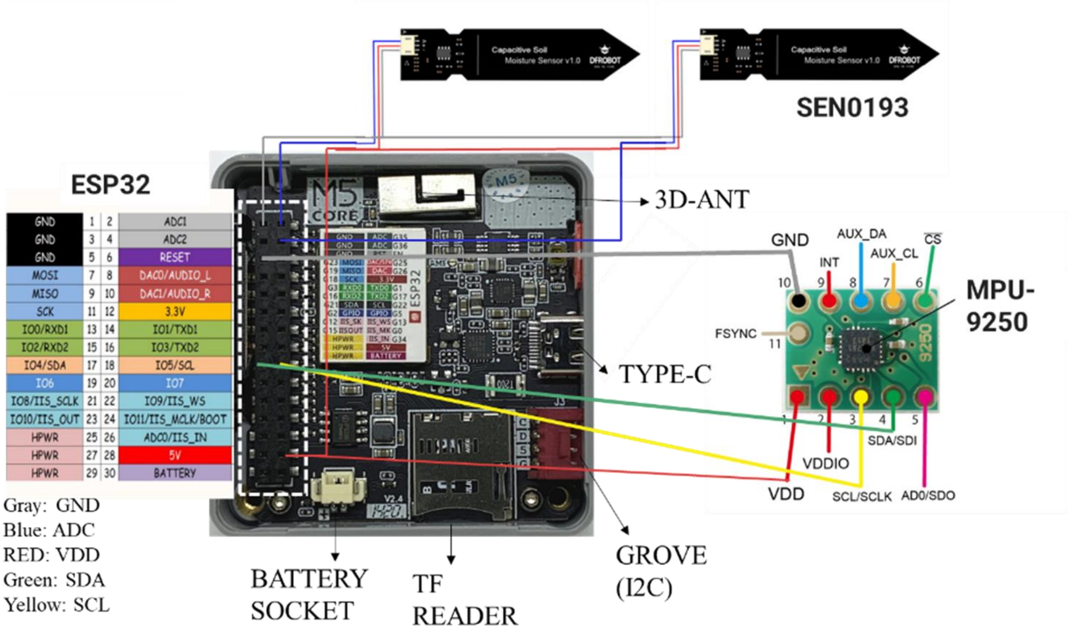

Fig 3.4 Diagram sensor conection by M5stack

3.2.3 Data display and analysis of the EWS

For remote real-time monitoring, this research carried out a visual display on the basis of Ambient. Ambient is an IoT data service that receives, stores, and visualizes sensor data. This function developed in Arduino compiler/IDE helps to make creative designs for IoT as easy as possible. It plots the sensor data in real-time without the requirement of a detailed initial setup. By adding more settings, Ambient can provide powerful customization capabilities, such as giving graphs and data names that are easy to understand, changing graph types, and overlaying multiple data on one graph. The most important thing is that the monitoring results can be observed remotely, and it supports various devices to check, such as mobile phones and computers.

Regarding the data analysis part, this research presents the principle considered for handling monitoring data. The data processing tire manages IoT big data streams, which will be trained for landslide monitoring by proposed risk classification. Based on the trend of rainfall infiltration, key warning indices such as soil moisture content, pore-water pressure, and deflection angle are set in the system, and a comprehensive slope stability analysis is carried out to obtain the real-time Factor of Safety (F_s) of the slope under various rainfall conditions. The whole proposed risk classification has been divided into three stages: Monitoring State (Stage I), Alert state (Stage II), and Triggering State (Stage III). And before each landslide, at least 3 warning signs will be sent.

Three main data display methods have been introduced in this thesis. The first is the designated software or APP, this is easy to monitor data and set the threshold, but it has the limilation of data display form (Shown in Fig 3.5 of the mail system software). In general, such methods are less exploitable. The second method is some open-source platform, which provides a free website for users to develop. Users only need to write the program in the EWS and the system can directly send data to the website. This is much easier for user to operate with real-time checking. But the data limilation need to be considered. The last is the personal DIY monitoring platform that implemented an application to access and visualize the time series database. The system correctly collected the sensor data (as shown in **Fig 3.7**). It can provide different kinds of pictures, parameters and other information. However, it is difficult to develop and requires budget to maintain.

Fig 3.5 Data display of terminal server

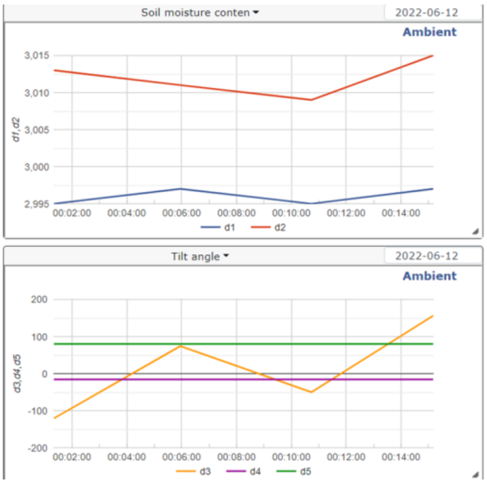

Fig 3.6 Data display of open-source platform

Fig 3.7 Visualization of sensor values

3.2.4 Off-grid solar photovoltaic system

To make the monitoring sustainable, solar panel will be put near the sensors and communication devices for timely power supply. And research applied a battery low-consumption infrastructure monitoring sensor platform (Kanaya et al. 2021). It's also necessary to ensure the system with continuous power supply for around one week without any sunshine, so the solar panel with a large power capacity was considered in this research. The maximum absorption power of the solar panel is 200W, and the storage capacity of the battery is over 3000Wh, so in theory, 10 hours of continuous absorption of sunshine can ensure that the battery is fully charged. In order to ensure the sustainable operation of the whole EWS process, research also calculated the battery usage of each device group in the Table.3.1. Since sensors will be connected with IoT devices, so this study only needs to calculate the power when the IoT devices are all connected to the sensors. The monitoring area is usually divided evenly into several groups, and one group has around 5 IoT boards, one Raspberry Pi-4, one mail system and one mobile router, the whole power consumption for one group is around 20W. Therefore, each group only needs to build a solar system, which can guarantee normal operation for more than three days even without any solar energy. The Off-grid solar photovoltaic system was shown in **Fig 3.8**.

Fig 3.8 Off-grid solar photovoltaic system

3.3 Operation of the early warning system

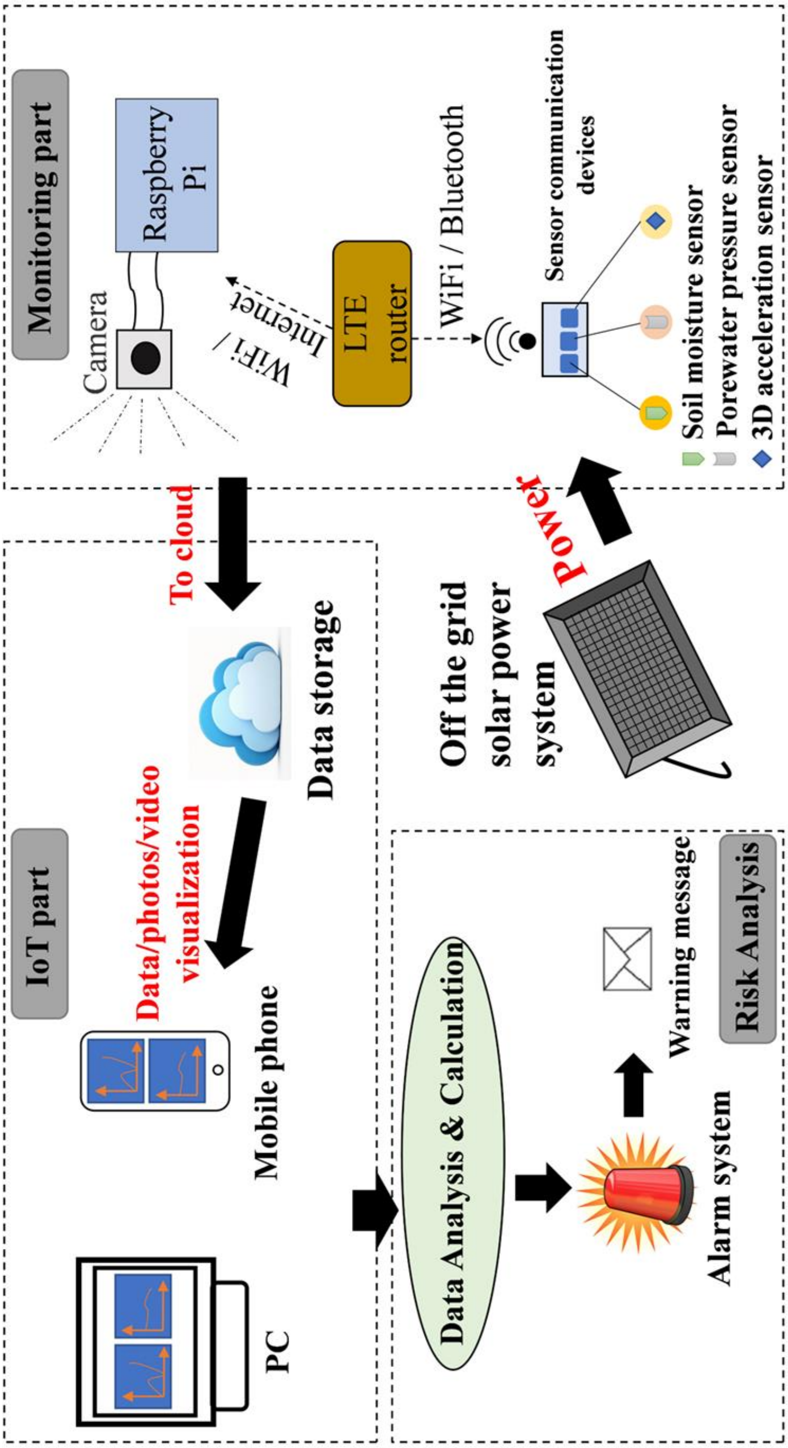

Fig 3.9 Diagram of early warning process

As **Fig 3.9**. shows, the proposed Internet of Things (IoT) based EWS will provide an operational platform for comprehensive data storage and quantitative analysis. First of all, according to the geological conditions of the site, establish the suitable EWS, including sensors, IoT devices, communication devices, and Off-grid solar photovoltaic system. Data collected from embedded sensors such as soil moisture sensors and pore water pressure sensors are used to determine the degree of rainwater infiltration and change in the groundwater table, and data from 3D accelerometers are utilized to measure the deflection angle. Real-time images from Raspberry Pi with digital cameras are used to determine landslide time and track the displacement of the monitoring points by motion analysis. A sustainable solar panel is used to power the entire system. All the data can be stored in the cloud and operators can monitor the system remotely. Furthermore, once the monitoring parameters reach predetermined threshold limits, the system sends warning signals.

3.4 Thresholds setting and alarm time in the EWS

This part just gives an simple example of the early warning process. First of all, this study considers the soil moisture sensors, porewater pressure sensors and acceleration sensors, so users have to set threshold before staring the EWS work. Here, according to the different slope failure modes, the data monitored by the sensors will have different magnitude of values at different point to time. The right side in **Fig 3.10** is the early warning process for shallow failure, while the left side is the early warning process for deep failure. Before a landslide occurs, at least three warning signals will be issued. This flow chart also provides some references for the issuance time of early warning signals. The slope geometry and soil conditions will affect the early warning process and the criteria of thresholds. However this flowchart intends to present a generalized warning principle for different geometrical and geological slope conditions.

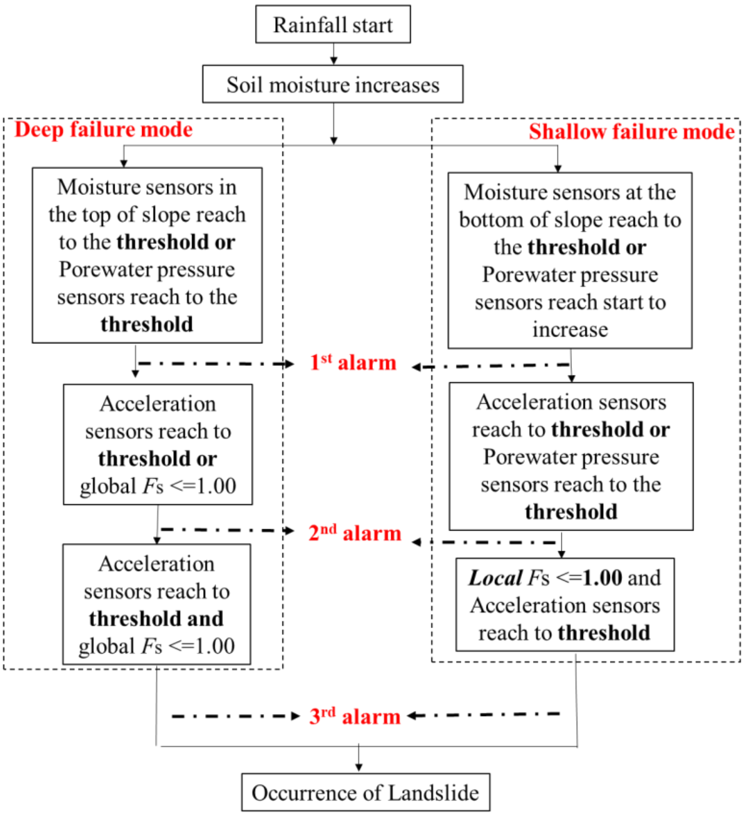

Fig 3.10 A simple example of early warning process

3.5 Conclusion of this chapter

The architecture, operation and comparison of the newly developed EWS are discussed in this chapter. The preliminary conclusions are as follows:

(1) The proposed EWS can monitor the soil moisture content and pore water pressure, track the ground deformation and provide real-time F_s during the rainfall. The application of IoT and solar battery systems enables the proposed EWS to operate cost-effectively and sustainably.

(2) This system can accommodate and be compatible with any sensor with an I2C output, thereby making it possible to be upgraded at any point of time for different application scenarios and monitoring requirements. This system has an option to use both cellular networks and freely available radio frequency waves for data transmission through Low Power Wide Area (LPWA) connectivity system. This makes it flexible to be used in areas with good, bad and no cellular networks.

(3) This chapter also presents how IoT-based EWS can forge new paths for interdisciplinary study and generate a positive impact on disaster mitigation work in the future.

Reference

Kanaya, H. Mansour, M. M. Hatanaka, S. Nakashima, A. & Takiguchi, O. 2021. Battery-Less Infrastructure Monitoring Sensor Platform. In Advances in Sustainable Construction and Resource Management : 907-915, Springer, Singapore.

Liu, Y., Hazarika, H., Takiguchi, O., & Kanaya, H. (2021). Developing a Sustainable System for Early Warning Against Landslides During Rainfall. In Advances in Sustainable Construction and Resource Management (pp. 917-926). Springer, Singapore.

Lu, N., Şener-Kaya, B., Wayllace, A., & Godt, J. W. (2012). Analysis of rainfall-induced slope instability using a field of local factor of safety. Water Resources Research, 48(9).

Noreen, U., Bounceur, A., & Clavier, L. (2017, May). A study of LoRa low power and wide area network technology. In 2017 International Conference on Advanced Technologies for Signal and Image Processing (ATSIP) (pp. 1-6). IEEE.

Saari, M., bin Baharudin, A. M., Sillberg, P., Hyrynsalmi, S., & Yan, W. (2018, May). LoRa—A survey of recent research trends. In 2018 41st International Convention on Information and Communication Technology, Electronics and Microelectronics (MIPRO) (pp. 0872-0877). IEEE.

Tanaka, K., Maeda, H., Yamashita, K., Liu, Y., Hazarika, H (2022) Implementation and proof experiment of Communication Network for Disaster Prevention using LPWA. Springer-Verlag Lecture Notes in Computer Science (ICCSA 2022), Spain

CHAPTER 4

4. LABORATORY EXPERIMENT BASED ON PROPOSED EWS

4.1 Introduction

The method of model test is classic and commonly used, which is also the closest to the real scene of landslide disasters. In the preceding experiment studies, various sensors were inserted inside the slope to monitor the soil moisture content, pore-water pressure, slope displacement, etc., and summarize the relevant laws (Chueasamat et al 2018; Cogan and Gratchev 2019; Xie et al.2019). Studies often focus on multiple preconditional, preparatory, and triggering factors, such as rainfall intensity and initial soil moisture content to elucidate the hydrological characteristics, failure forms, and mechanisms under rainfall conditions. Cogan and Gratchev (2019) conducted model tests under different rainfall conditions, and his study considered the rainfall effects of rainfall intensity (40, 70 and 100 mm/h), slope angle (45–55°) and initial soil moisture content (5–12%). Finally, the experiment data was analyed by Intensity-Duration curve and compared with classic results. Xu et al (2022) conducted a series of centrifugal experiments to study the effect of continuous heavy rainfall on the slope stability in the case of cracks after the earthquake. The results are combined with particle image processing and theoretical analysis. This study provides a certain reference for similar engineering geological backgrounds. Huang and Yuin (2010) carried out model experimental analysis on sand slopes, recorded the volume of different shallow landslides, the time of displacement, drew a series of ***I-D*** curves, and proposed a large number of evaluation expressions. Wang et al (2020) presented the results of a centrifuge test of rainfall-induced instability in a variably saturated slope. This work elucidated the role of rainfall intensity and initial conditions (eg, slope angle, porosity, and soil saturation) on the kinematics of failure onset and after failure. The failure modes, infiltration profiles and deformations were characterized in the initial and post-failure stages. Following the summary, two failure modes are introduced, whose test data are presented in two threshold curves together with literature data to define the critical conditions for slope failure under rainfall infiltration.

In order to verify the feasibility of the system, a series of model tests were carried out in the experiment room. The designed model tests were conducted using a rectangular box and rainfall simulator employed for the slope under different rainfall intensity and initial soil moisture content. The rainfall intensity considered in this research is 45 mm/h, 70 mm/h and 100 mm/h. The initial soil moisture content is 8%, 12% and 17%. Experimental method presents the distribution of soil moisture content within slope, and the migration of groundwater table calculated from the data of the porewater pressure, and small deflection angle of the monitoring points. Real-time local factor of safety (F_s) during continuous rainfall periods is evaluated by the analytical method.

This chapter firstly introduces the operation principle of the early warning system under different geological conditions, and proposes the thresholds that can be applied to this experiment. A series of experiments were subsequently carried out, and the warning times of different stages and detailed parameter changes were shown. This study can provide a feasibility verification for the launch of the early warning system.

4.2 Proposed Early Warning Process

Considering the effects of rainfall on the monitoring slope, there are two forms of landslide, one is deep slope failure which is mainly due to the saturation or even erosion of the topsoil by rainfall infiltration, where the topsoil mainly contains the clay layer, weathered soil, tropical residual soil, etc. The other kind is multiple shallow failures from slope toe, which usually occurs in sandy soil slope. It appears with the phenomenon that the slope gradually tends to be saturated from the bottom due to the rise of the groundwater table. As a result, research will consider the following step to prepare the sensor deployment and threshold setting: (1) Conduct preliminary on-site geological surveys to determine specific failure modes; (2) Regarding the deployment of sensors under each borehole in the slope, both of moisture sensors and acceleration sensors need to be deployed at different depths. According to different failure modes, the porewater pressure sensor needs to be deployed in the upper layer, while for shallow failure, the porewater pressure sensor can be deployed below; (3) Test the critical or saturated water content of the soil to define the threshold, set the threshold of deflection angle according to slope geometry and set the threshold of the porewater pressure according to the depth of sensor location in each borehole. Since the sandy slopes are widely distributed in Japan, the failure mode is typically characterized by multiple shallow landslides. This study will focus on typical sandy soil slopes to give an example of threshold setting and EWS working.

4.2.1 Rainwater Flow in the Soil

In designed laboratory test, sand soil has been usually chosen to explore the failure mechanism of slope under the condition of heavy rainfall. As a result, the system is mainly tested on homogeneous sandy slopes currently. The infiltration of rainwater on sandy slope will cause the rise of the groundwater level and the decrease of the shear strength. The path of water infiltration, soil moisture distribution and the ground water level can be considered as important indexes for the prediction of landslide. The schematic diagram of rainwater infiltration in the slope is shown in **Fig 2.2**. First of all, research needs to clarify the detailed process of rainwater infiltration to the sandy slope:

(1) rainwater infiltrates and soil moisture increases to a critical value of $\boldsymbol{M}_{\mathbf{c\text{-}t1}}$, this is not the saturated moisture content of the sand, and the moisture content will keep constant around $\boldsymbol{M}_{\mathbf{c\text{-}t1}}$ for a period;

(2) Rainwater reaches to the impermeable layer and generates porewater pressure, due to the groundwater level rising, the water content increases again until the soil reaches fully saturated state $\boldsymbol{M}_{\mathbf{c\text{-}t2}}$.

(3) The porewater pressure rapidly rises to a critical value $\boldsymbol{F}_{\mathbf{w\text{-}t}}$. After the proposed process, some small and obvious deflection angles will be captured ($\boldsymbol{D}\_{}_{\mathbf{t1}}$ / $\boldsymbol{D}\_{}_{\mathbf{t2}}$).

The phenomenon of rainwater infiltration and groundwater increase has also been highlighted in Wang et al., (2020). It can be concluded that with the process of infiltration, rainwater will run from slope surface to impermeable soil layer and accumulate on the interface, finally it will cause the increase of groundwater level. According to the result of previous research (Koizumi et al., 2018; Jacob and Ivan 2019; Chueasamat et al., 2019), for shallow landslide with sandy soil, a landslide often occurs when slope reaches saturated or quasi-saturated state. Based on the rainwater infiltration into the soil, the soil moisture content at the critical state and saturated state can both be used as a threshold reference in the infiltration process, and the evolution of porewater pressure can also be used as the threshold evaluation standard. When the slope is gradually saturated, particles in the slope will move slightly, so sensors will detect some slight deflection angles. In the study of using deflection angle to forecast the occurrence of landslide, research found that once the internal deflection of the slope exceeds the threshold, a landslide will occur rapidly (Uchimura et al., 2015).

4.2.2 Flowchart of Early Warning process

This designed laboratory test is based on a hypothetical homogeneous slope and uniform rainfall infiltration, 4 important warning indices: soil moisture content, pore-water pressure, soil deflection angle, and safety factor (F_s) are considered to evaluate the state of the slope and issue signals of landslides, the flow chart is shown in **Fig 4.1.** As the flowchart shows, first of all, the thresholds of warning indices need to be input into the system, which represent the transition of each risk stage. All the warning indices are determined by the type of soil and the shape of the slope. The thresholds set in this research are as follows: 1. Soil moisture thresholds M_{c_t1} and M_{c_t2}, which represent the critical value of sand slope before saturation and saturated volumetric moisture content respectively; 2. Pore-water pressure: P_{w_t1} and P_{w_t2}, P_{w_t1} is the state when the pore-water pressure is first captured, which is generally 0-0.1 kPa, P_{w_t2} is the critical value before landslide; 3. Small deflection angle thresholds $D_{\_t1}$ and big deflection angle thresholds $D_{\_t2}$ before landslide; 4. Threshold of safety factor F_{s_t}, which is usually 1.0, and is in a safe state when $F_s>1$ and in danger state when $F_s<1$. After setting all the thresholds, the work will start. The first stage is Monitoring State, in which the soil moisture will increase from initial volumetric moisture content to M_{c_t1} with the rainwater infiltration, since the rainwater doesn't reach to impermeable layer, there is no pore-water pressure in this step. So, the 1st warning message will be sent once the pore-water pressure sensors detached reaction of rising P_{w_t1} or all moisture sensors reach M_{c_t1}, which also means that the system enters to Alert State. Then the soil moisture sensor will capture the rapid increase and the slope will become a saturated state as the groundwater level moves from bottom to upon. However, in this state, porewater pressure doesn't reach the threshold P_{w_t2} and acceleration sensors don't find any fluctuations (less than $D_{\_t1}$). Once the acceleration sensors exceed the small deflection threshold $D_{\_t1}$, or porewater pressure reaches the threshold P_{w_t2}, the 2nd warning message will be released, and the state will enter the third stage: Triggering

State. Finally, when real-time *F*s is smaller than 1.0 or deflection angle is more than $D_{\_t2}$, the system will give the last warning message and landslide will occur within a very short time. **Fig 4.1** describes the whole process and timeline of early warning in detail.

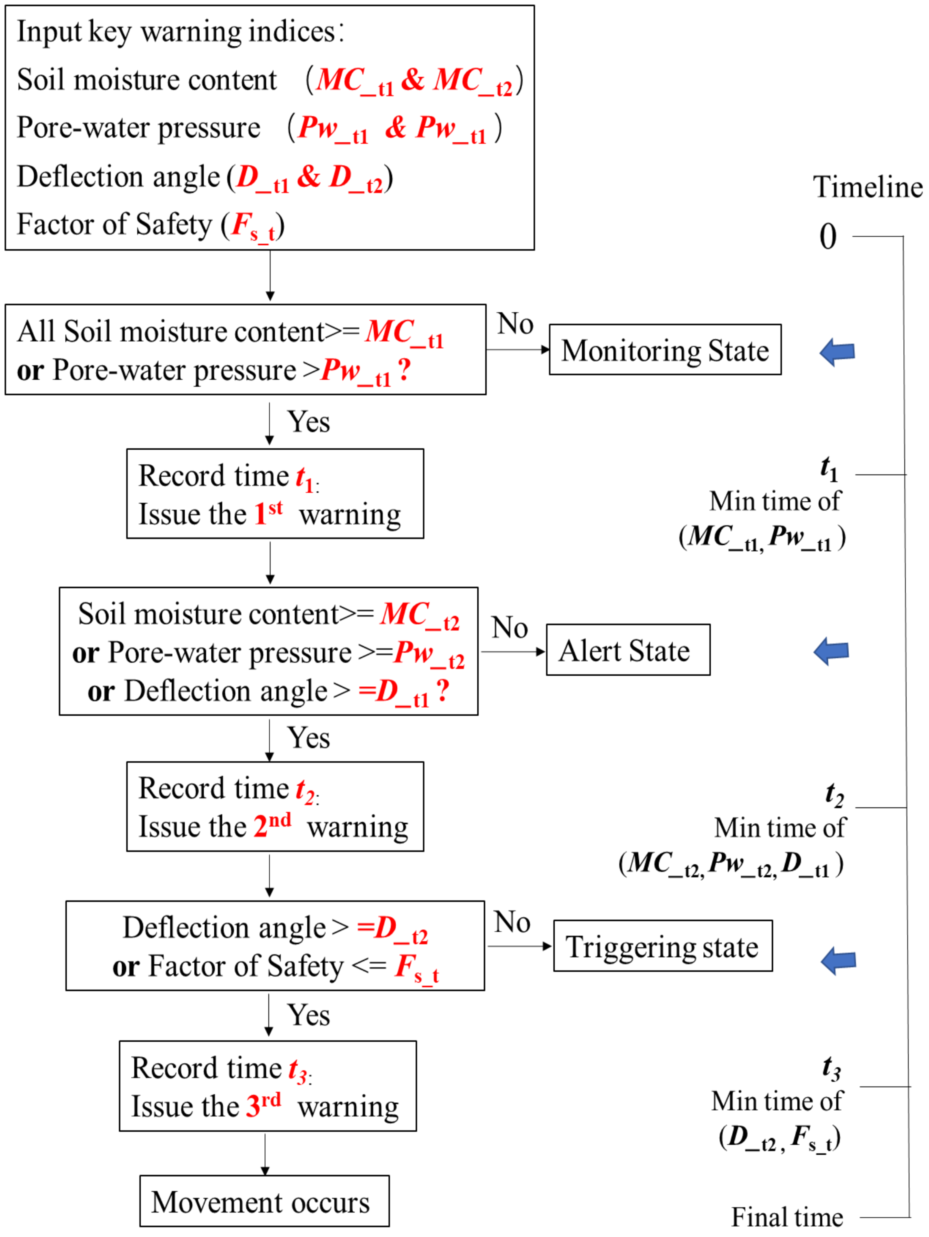

Fig 4.1 Flowchart of the proposed EWS

4.3 Preparation work before the test

4.3.1 Soil type

A model test was carried out to check the feasibility of the system. The soil type chosen in this research is Kumamoto silica sand type of *K*7 (fine sand) which is subangular and has uniformity coefficient. The grain size distribution of *K*7 is shown in **Fig 4.2** and the specific physical information of soil is shown in **Table 4.1.**

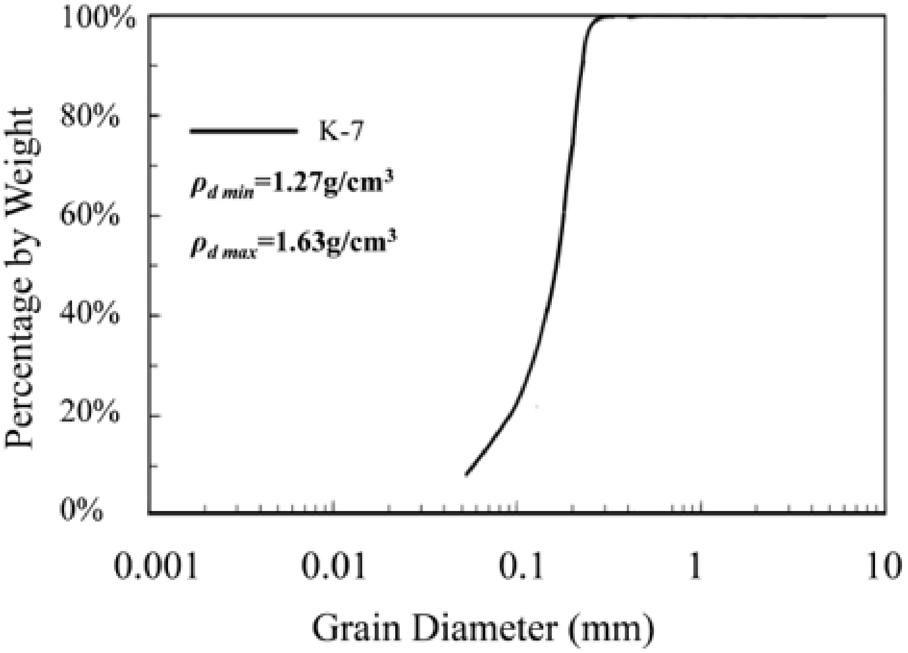

Fig 4.2 Grain-size distribution curve for the silica sands K7

Table 4.1 Soil used in this research

Soil Type	Mean grain size, D_{50} (mm)	Uniformity coefficient U_c	Specific gravity, *G*s	Dry density (g/cm^3)	Void ratio, *e*
K7	0.17	2.96	2.62	1.4	0.866

4.3.2 Experimental facility

As **Fig 4.3** shows, the rectangular box was used to conduct the test, and the slope model was designed by a length of 800 mm, a width of 400 mm and a height of 450 mm. The rainfall intensity was controlled to produce artificial rainfall by the suspended sprinklers with flowmeter. A set of wireless sensor combinations: 6 soil moisture sensors, 3 pore-water pressure sensors and 4 MEMS acceleration sensors were placed in the slope, 2 raspberry Pi with image sensors took real-time photos or videos from the front view and top view. The artificial rainfall simulator and model size information are shown in **Fig 4.3 (a)**. Four soil moisture sensors were put below the top of the slope, and 2 soil moisture sensors were put below the surface. The porewater pressure sensors were located in the bottom and four acceleration sensors were arranged along the surface. The layout of test sensors and devices information in the early warning test are performed in **Fig 4.3 (b)**.

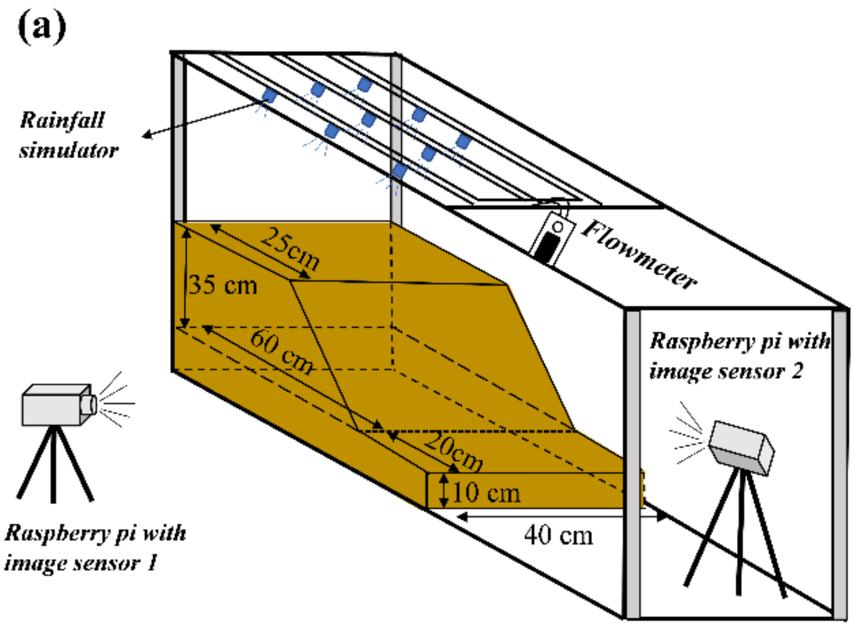

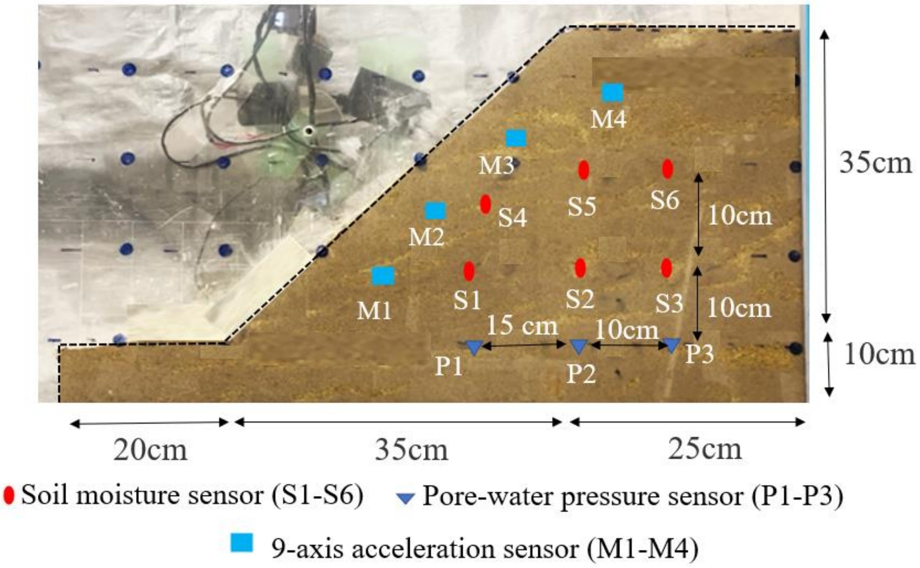

Fig 4.3. Model test overview. (a) artificial rainfall simulator and model size; (b) test sensors layout

4.3.3 Testing constraints

Model tests were conducted considering rainfall intensity and initial volumetric moisture content, which are divided into Group A and Group B in Table.4. 2. The rainfall intensity in this research is 45 mm/h, 70 mm/h, and 100 mm/h, and the initial volumetric moisture content is 8%, 12%, and 17%. Rainfall intensity of 60 mm/h was also conducted to verify the accuracy of the interpolation calculation in the next chapter.

Table 4.2 Testing program

Test	Initial soil moisture content	Rainfall intensity	Description
A	17%	45	Group A
B	17%	70	Group A and B
C	17%	100	Group A
D	12%	70	Group B
E	8%	70	Group B
F	17%	60	Verification test

4.3.4 Threshold Settings

This research also conducted some testing work with reference to previous studies (Wang et al. 2020) to obtain the moisture evolution of sand soil K7. Results from labortory tests show that the critical value of sand slope before saturation state is around 28%, and saturated volumetric moisture content is 36%-38%. So, research set $MC\_{}_{t1}$=28% and $MC\_{}_{t2}$=36%. Since the P1 was located below the hillslopes, it was the first sensor to react, P_{w_t1} is set to 0.1kPa. The vertical distance between P1 and slope surface is 20 cm, so 1.5 kPa was set as the P_{w_t2} in this model. According to the previous study on deflection angle (Uchimura et al., 2010; 2015), it was concluded that operators need to be cautious when deflection angle reaches 0.005 degrees per hour and waning level enters to Alert / Evacuation state once deflection angle is more than 0.1 degrees per hour. Since the system in this research will give 3 warning messages and each test usually lasts 1-2 hours. Deflection angle index is set to $D\_{}_{t1}=0.1^{o}$, which is one of the weathervanes that state changes from Alert State to Triggering State, and this study also set that $D\_{}_{t2}=1^{o}$, which means the landslide will occur soon. Since this study uses the most unfavorable pore-water pressure coefficient to calculate the safety factor, the obtained F_S is always lower than the actual situation, so setting F_S to 1 is an early warning of landslide occurrence.

As a result, the threshold set in this research is: (1) $MC\_{}_{t1}$=28% and $MC\_{}_{t2}$=36%; (2) $Pw\_{}_{t1}=0\pm0.1$ kPa and $Pw\_{}_{t2}$=1.5 kPa; (3) $D\_{}_{t1}=0.1^{o}$ and $D\_{}_{t2}=1^{o}$; (4) F_{s_t}=1.000.

4.4 Results and Discussion of the test based on EWS

4.4.1 Model test based on EWS under different rainfall intensities

All real-time data will be transmitted to the cloud and displayed visually. **Fig 4.4** to **Fig 4.6** present the time history of volumetric moisture content, pore-water pressure, soil deflection angle and factor of safety (F_s) under three rainfall intensities. It's obvious that greater rainfall intensity results in faster landslides. Monitoring results show that moisture sensor S2 was always the last sensor that detached reaction because it was located at the deepest part of the slope and it also stayed away from the slope surface. Therefore, when S2 reaches the threshold, it is considered that the entire monitored slope reaches the threshold MC_{t1}. In addition, Pore-water pressure sensor P1 was always the fastest sensor to monitor pore water pressure, because it had the shortest distance from the slope. Comparing the time of MC_{t1} and P_{w_t1}, it is found that the time of MC_{t1} is usually smaller than P_{w_t1}, for example, time for S2 to reach MC_{t1} in three cases was around 48min, 40min and 35min respectively, but the response time for P1 in the three cases was 65min, 42min and 35min. Therefore, the first signal will be sent at an earlier time. Before the first warning, the slope was in Stage I - Monitoring State. With the infiltration of rainwater, the soil moisture content kept stable for a short time near the threshold MC_{t1}. On the contrary, S1 and S2 re-increased faster than other sensors because the groundwater table went up from impermeable soil layer, and all the sensors raised to MC_{t2} in turn as soil slope gradually became a saturated state. Research found that S1 was always the first sensor that reached MC_{t2}, time for the area near S1 to become a saturated state in three cases was 81min, 62min and 48min, which was considered to be one important index for the 2nd warning. After entering to Stage II - Alert State, porewater pressure increased rapidly. The time for pore-water pressure sensor to reach MC_{t2} was 92min, 65min and 50min in three cases. As the pore-water pressure increased, it's obvious that there was some fluctuation from the data of MEMS acceleration sensors. D_{t1} was set to evaluate the intensity of fluctuation, research found that M1 near the slope toe was the first MEMS sensor to detach rection and the time of D_{t1} in three cases was 93min, 70min and 50min. According to the principle of early warning, compare the time when the three parameters reach the threshold, the second warning signal will be released at time of 92min, 65min and 50min. After 2nd warning was sent, the whole slope was in danger state and it entered Stage III -Triggering State. Obvious deflection angle was captured by the sensor from M1 to M4, because sandy soil slopes often cause multiple shallow landslides. When in Triggering State, the deflection angle of M1 increased from $\boldsymbol{D}_{\_t1}$ to $\boldsymbol{D}_{\_t2}$ at time of 106min, 80min and 57min. At this time, the F_s also dropped rapidly until reaching the critical value of 1.00. Under the three rainfall cases, F_s reached the critical value in 99 min, 76 min and 56 min respectively, which are all less than the time of deflection angle $\boldsymbol{D}_{\_t2}$**.** Therefore, the 3rd message was sent when F_s reaches the critical value. Research also finds that it cost only 3-12 min for the occurrence of the landslide after 3rd message. **Table 4.3** records the time of each indicator threshold, warning signal, and the occurrence time of multiple landslides in detail. The experimental results were in line with expectations, that is, the three warnings were sent before the landslide occurred.

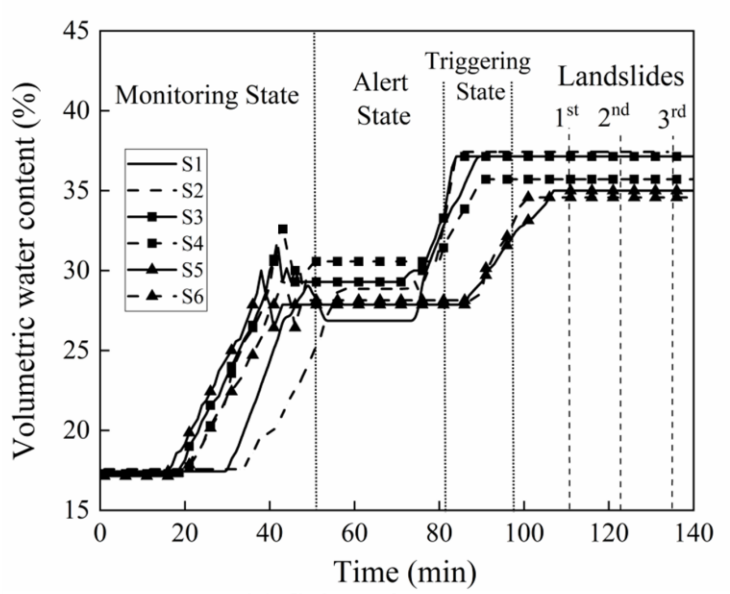

(a) Soil moisture content

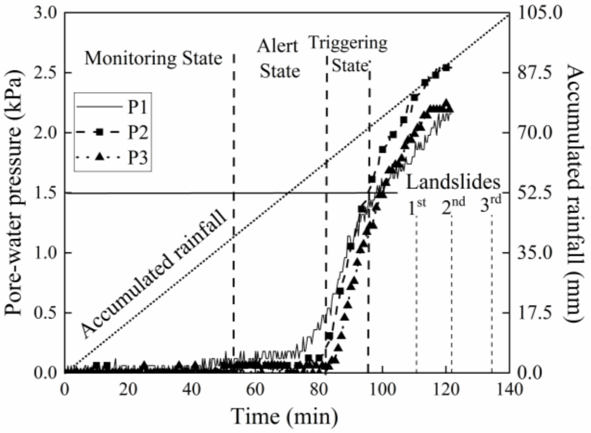

(b) Pore-water pressure

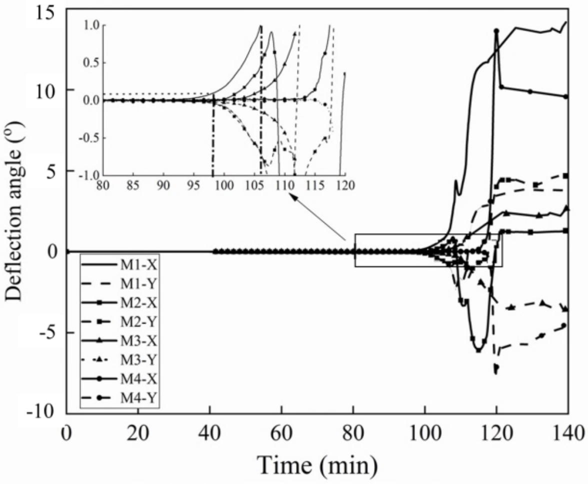

(c) Deflection angle

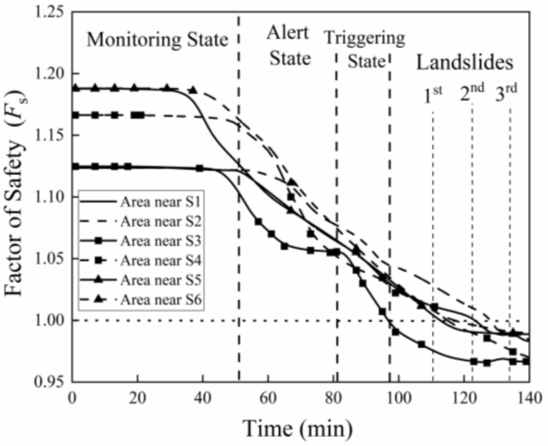

(d) Factor of Safety

Fig 4.4 Model test result of Test A: (a) Volumetric moisture content; (b) Pore water pressure; (c) Deflection angle; (d) Factor of Safety

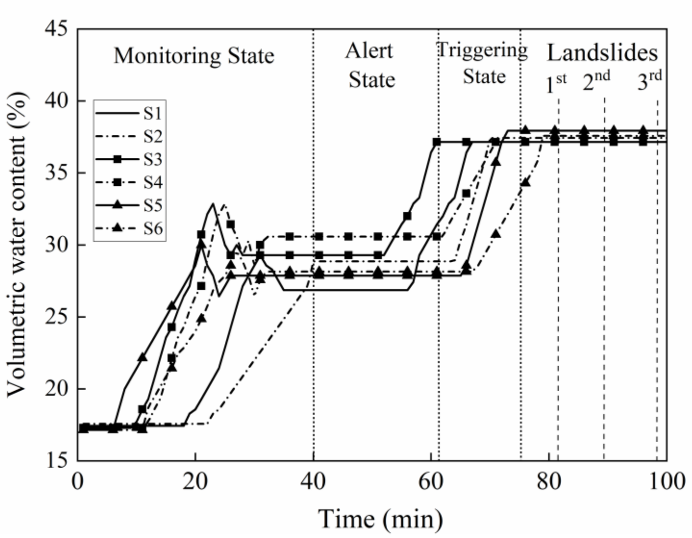

(a) Soil moisture content

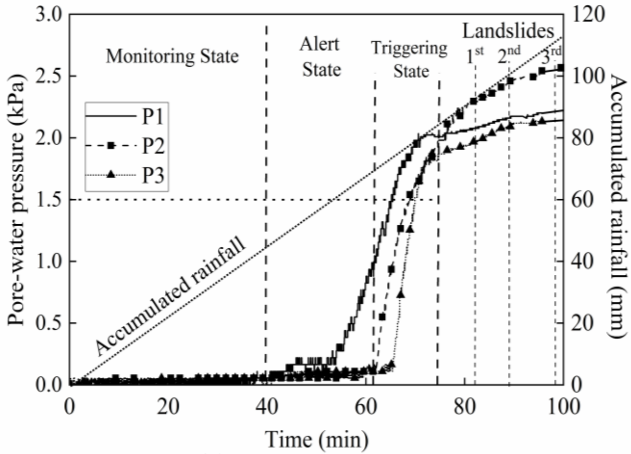

(b) Pore-water pressure

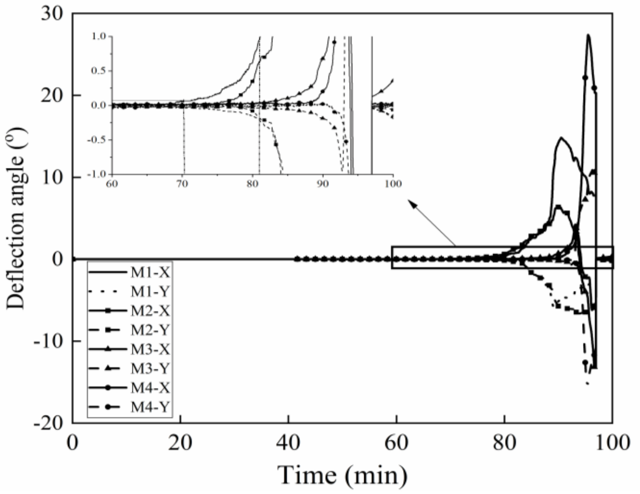

(c) Deflection angle

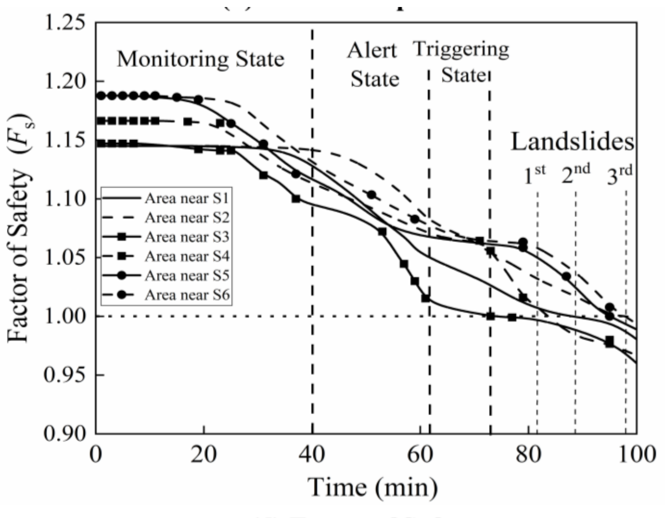

(d) Factor of Safety

Fig 4.5. Model test result of Test B: (a) Volumetric moisture content; (b) Pore water pressure; (c) Deflection angle; (d) Factor of Safety

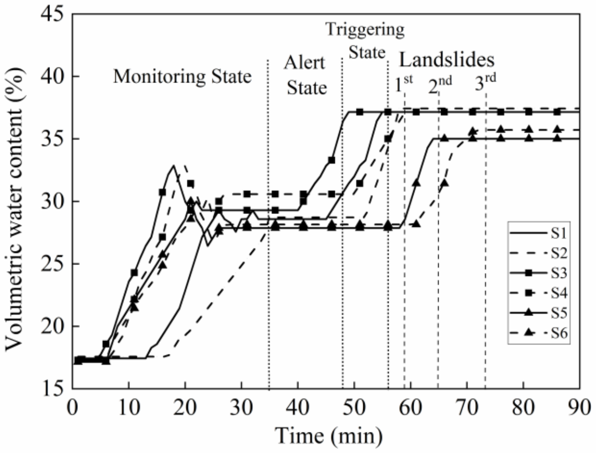

(a) Soil moisture content

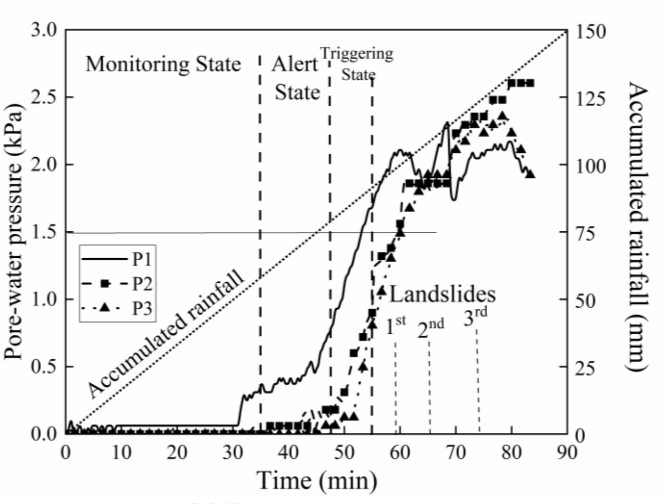

(b) Pore-water pressure

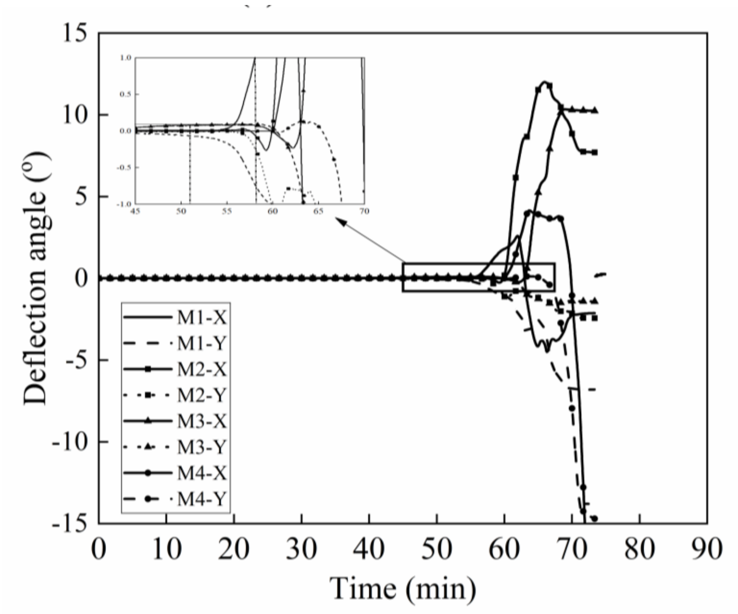

(c) Deflection angle

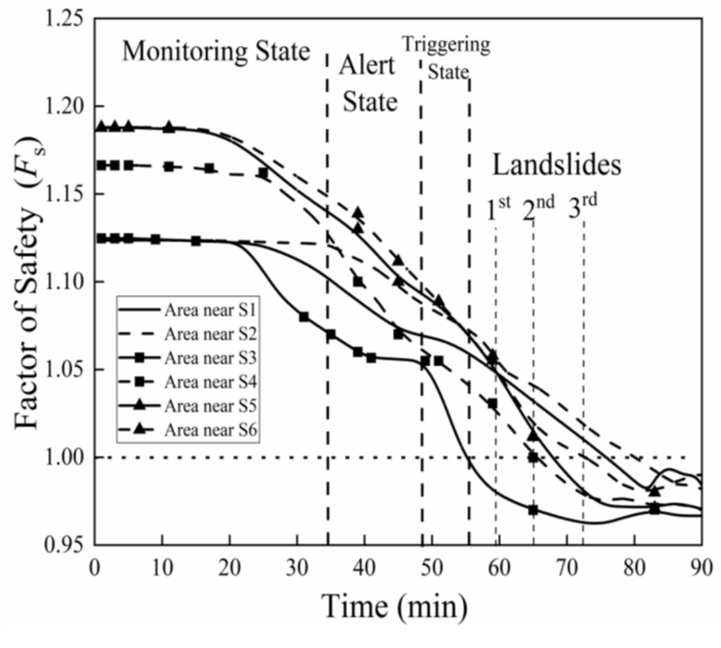

(d) Factor of Safety

Fig 4.6 Model test result of Test C: (a) Volumetric moisture content; (b) Pore water pressure; (c) Deflection angle; (d) Factor of Safety

Table 4.3 Time of each indicator, signal, and the occurrence time of multiple landslides

Case No.	Rainfall intensity (mm/h)	Time of warning indices (min)							Time of warning (min)			Time of each landslide (min)		
		Stage 1		Stage II			Stage III							
		MC_{t1}	Pw_{t1}	MC_{t2}	Pw_{t2}	D_{t1}	F_{s_t}	D_{t2}	1st*	2nd	3rd	1st	2nd	3rd
A	45	52	65	81	92	93	99	106	52	81	99	111	122	135
B	70	40	42	62	65	70	76	80	40	62	76	82	91	98
C	100	35	35	48	50	50	56	57	35	48	56	59	65	73

To evaluate the accuracy of the test results, research conducted a comparison with representative Intensity-Duration thresholds with similar soils types (Chien et al., 2005; Dahal and Hasegawa 2008; Jacob and Ivan 2019). ***I-D*** thresholds explain time to collapse against different rainfall intensities, which has been widely used around the world as an early warning system. As shown in **Fig 4.7**, in this study, two important times were used to compare, namely, the first shallow landslide on the slope surface and the final deep landslide. It was found that most of the result in the test is between the upper bound (Chien et al., 2015) and lower bound (Dahal and Hasegawa 2008), which verifies the rationality of the system. But test result of the first shallow landslide is a bit lower than the average value of previous studies because the slope in this research was considered to be whole homogeneous and this study set a big initial water content (12%) and large slope angle (45°). The rainfall intensity-duration thresholds were developed using data and the function of thresholds are:

$$I\_{1st}=98.78*D^{-1.228} \qquad (6)$$

$$I\_{final}=128.4*D^{-1.252} \qquad (7)$$

Here I is rainfall intensity (mm/h) and D is the duration (h). The I-D obtained in this study can also provide certain reference values for similar soil sample slopes.

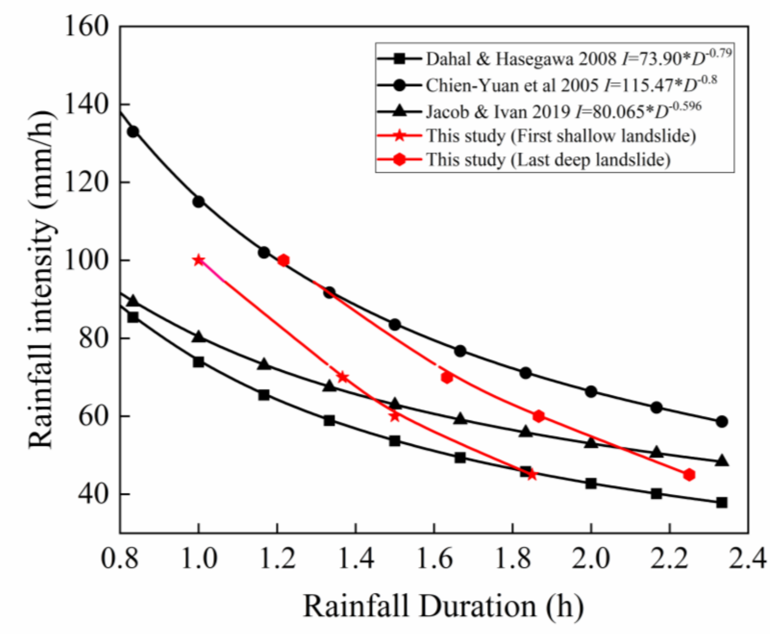

Fig 4.7 Results of *I-D* thresholds compared with previous research

Fig 4.8 and **Fig 4.9** shows the sand slopes always induce multiple shallow landslides from both side view and front view. Research presents the front view at different duration times during rainfall intensity 100 mm/h. As the initial state is shown in Fig.8, from the side view, 7 tracking points were marked in the slope, of which 4 points (Point 1-Point 4) are along the slope and 3 points (Point 5-Point 7) are inside the slope. Research defines three slope failures based on obvious movement captured by motion analysis (next chapter), which occurred successively from bottom to top. Research also can provide real-time displacement of monitoring points, motion trajectory and deflection of monitoring point coordinates, etc. Fig.10 shows that point 1 and point 5 have the fastest response, while point 1, point 2 and point 3 have longer displacement than other points. Because point 1 and point 5 are located in the first shallow landslide area, prompting them to move the fastest. Since point 1- point 3 are close to the slope surface and are in the landslide area, the resulting displacement is longer. Motion analysis also record the tilt angle *a* of recorded point coordinates, it's different from that of data from MEMS acceleration sensor. The tilt angle *a* of recorded point coordinates is the angle between the final position and the initial position with respect to the horizontal plane. It is also easy to understand that the tilt angle *a* generated in the upper part will be significantly larger than that in the lower area because the slope is steep with 45° and the landslide mass is accumulated at the slope toe, so it is more likely to generate a larger tilt angle. Especially Point 3 and Point 4 at the top area, resulting in nearly 2 times the tilt angle of Point 5. It can be clearly seen that after the first landslide occurs, it will quickly spread to multiple landslides, and eventually produce extremely violent long-distance landslides. According to the results in the figure, more than 50% of the sliding distances of the monitoring points are derived from the last deep landslide.

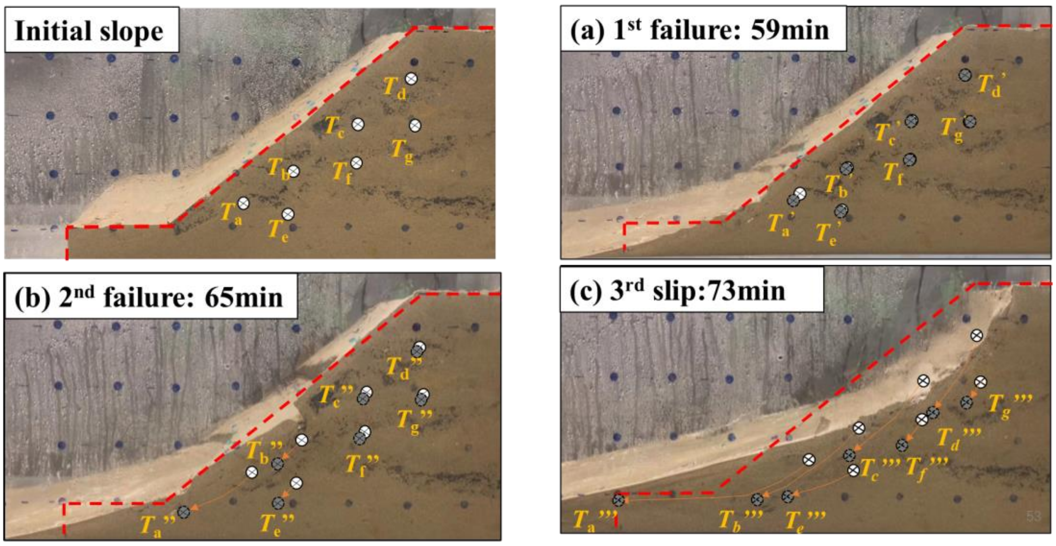

Fig 4.8 Side view of slope failure at different landslide stage

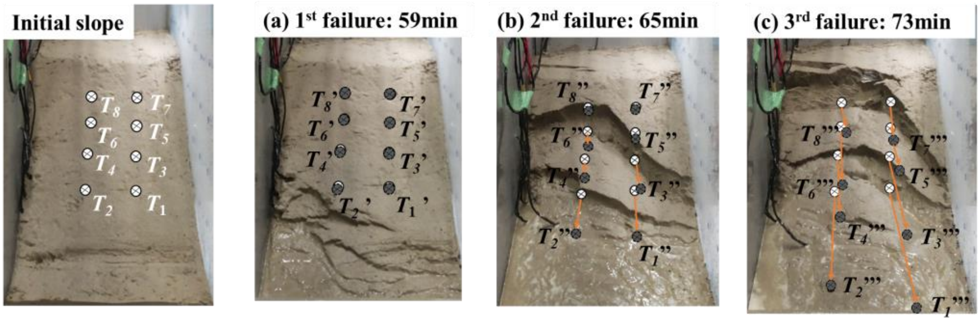

Fig 4.9 Front view of slope failure at different landslide stage

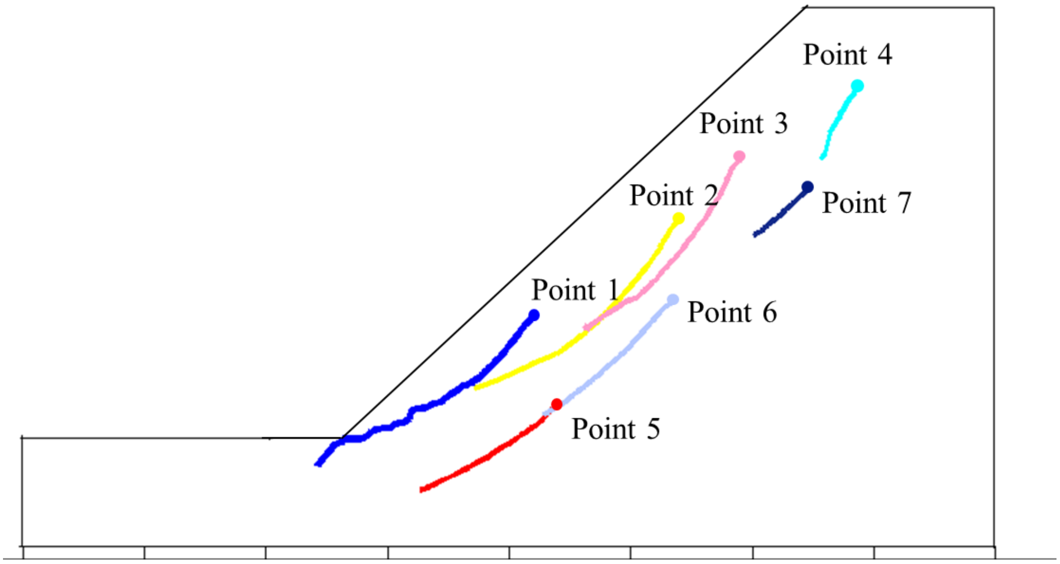

Fig 4.10 Particle coordinate motion trajectory

4.4.2 Model test based on EWS under different initial moisture content

In order to analyze the influence of the initial volumetric water content, experimental simulations with initial volumetric water content of 8%, 12%, and 17% are carried out at a fixed rainfall intensity of 70 mm/h. **Fig 4.11** and **Fig 4.12** present the results of Test D and Test E. It can be found that the results of Test D and Test E present the same trend as the results of Test A to Test C. But the lower initial water content leads to a longer time to trigger the landslides. Result in Table 4.4 shows the time of the three different states of three cases. The time for the first landslide from Test D, E is 115 min and 131 min, respectively, while the time for the final landslide from Test D and E is 131 min, and 148 min.

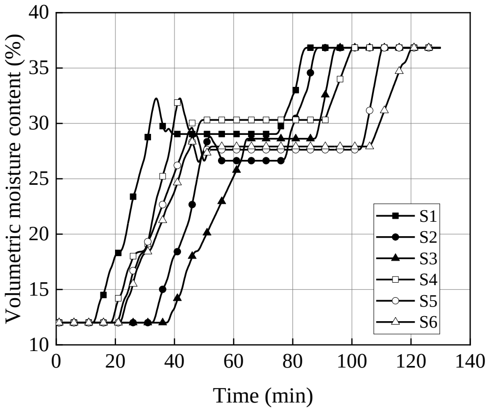

(a) Soil moisture content

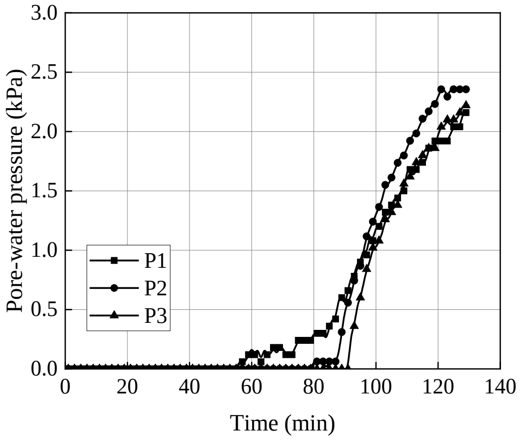

(b) Pore-water pressure

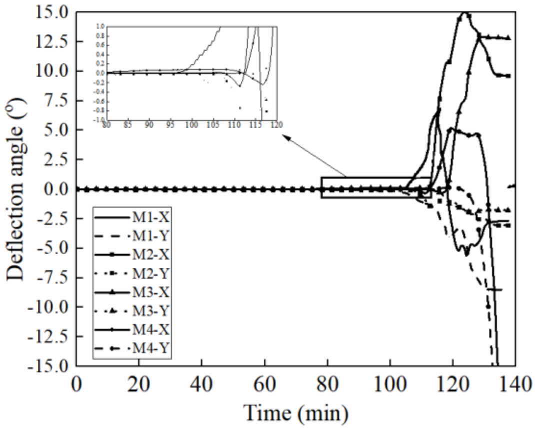

(c) Deflection angle

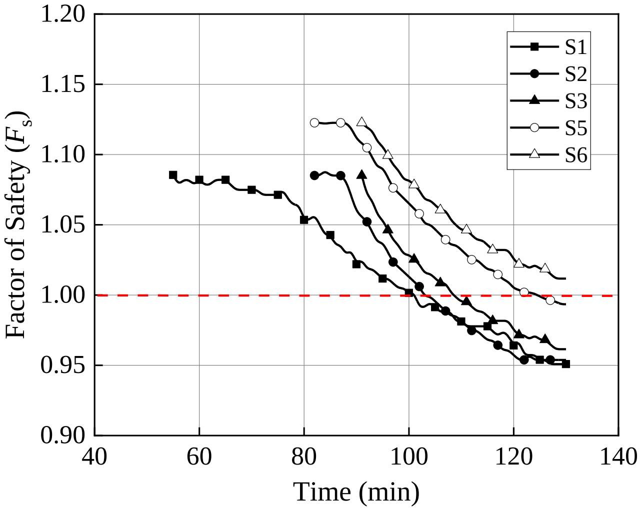

(d) Factor of Safety

Fig 4.11 Model test result of Test D: (a) Volumetric moisture content; (b) Pore water pressure; (c) Deflection angle; (d) Factor of Safety

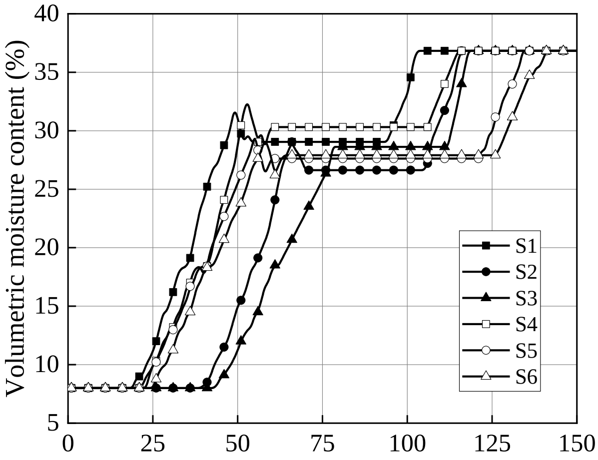

(a) Soil moisture content

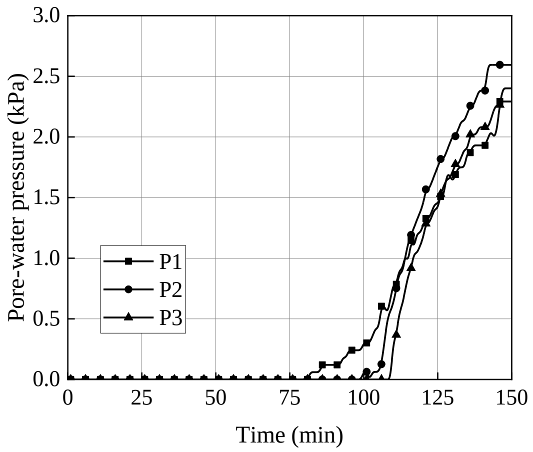

(b) Pore-water pressure

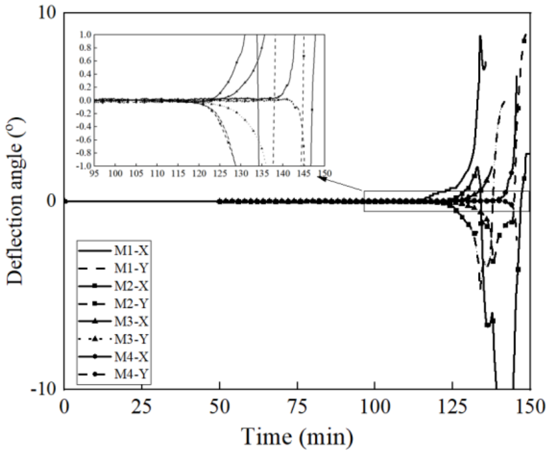

(c) Deflection angle

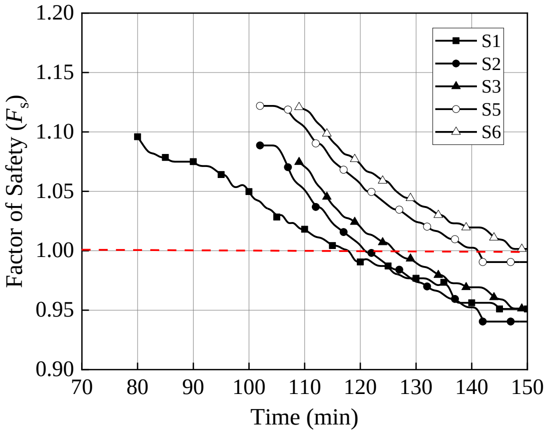

(d) Factor of Safety

Fig 4.12 Model test result of Test E: (a) Volumetric moisture content; (b) Pore water pressure; (c) Deflection angle; (d) Factor of Safety

Table 4.4 Time of each indicator, signal, and the occurrence time of multiple landslides

Case No.	Initial moisture content	Time of warning indices (min)							Time of warning (min)			Time of each landslide (min)		
		Stage 1		Stage II			Stage III							
		MC_{t1}	Pw_{t1}	MC_{t2}	Pw_{t2}	D_{t1}	F_{s_t}	D_{t2}	1^{st}*	2^{nd}	3^{rd}	1^{st}	2^{nd}	3^{rd}
B	17%	40	42	62	65	70	76	80	40	62	76	82	91	98
D	12%	52	56	84	95	98	102	108	52	84	102	115	124	131
E	8%	77	82	92	117	118	119	124	77	92	119	131	140	148

Table 4.4 presents each indicator time, signal time, and the occurrence time of multiple landslides, which shows the same trend as the trend in **Table 4.3**. The first landslide time in the three cases is: 82 min, 115 min and 131 min, the last landslide time is 98 min, 131 min and 148 min. While the alarm time for the three cases is 76 min, 102 min and 119 min respectively. These results all confirm the rationality of EWS.

4.5 Conclusion of this chapter

In order to evaluate slope stability under rainfall conditions and carry out early warning analysis for landslides. This research proposed a new EWS based on multiple sensors with IoT to monitor and forecast rainfall-induced landslides. The process of rainwater infiltration, porewater pressure change and the deflection angle of soil at different early warning stages were introduced in this research and model tests under typical geological conditions in Japan have been conducted to verify EWS feasibility. Here are some conclusions of this study:

(1) The newly developed real-time EWS is composed of cost-effective and portable sensor units, the entire sensor combination requires ultralow-power during operation and an off-the-grid solar energy-powered integrated sensor platform is used to optimize the sustainability of the system. The low cost and standalone energy harvesting feature of the EWS, allows it to be applicable across the world.

(2) Under rainfall conditions, the sandy slope model goes through five stages:

the volumetric moisture content increases, the groundwater table rises, the slope gradually saturates, $\boldsymbol{F}_\mathbf{s} \leq 1.00$, and the landslide occurs. The sequence of these five stages can be used as an important reference for the landslide prediction model. According to the important monitoring indicators and F_s calculated in real-time, the whole early warning process is divided into three stages: Monitoring State, Alert State and Tiggering State. In this study, factor of safety $\boldsymbol{F}_\mathbf{s}$, which is lower than the actual situation is used for risk assessment and landslide prediction. Research found that $\boldsymbol{F}_\mathbf{s}$ has been significantly reduced under continuous rainfall, and It will drop below 1.00 just before the landslide.

(3) In this study, the system presents accurate predictions and three warning times are all before the occurrence of the landslide. The model test based on **EWS** can provide the distribution characteristics of rainwater, the evolution trend of the groundwater table, which verifies the feasibility of the EWS.

Although the current experimental analysis is only carried out on a homogeneous indoor model slope, the concept for equipment assembly, landslide monitoring, risk classification, and warning message releasing has been proposed as a framework, which can be considered as a representative case for developing low-cost and sustainable early warning system in the future.

Reference

Chien-Yuan, C., Tien-Chien, C., Fan-Chieh, Y., Wen-Hui, Y., & Chun-Chieh, T. (2005). Rainfall duration and debris-flow initiated studies for real-time monitoring. Environmental Geology, 47(5), 715-724.

Chueasamat, A., Hori, T., Saito, H., Sato, T., & Kohgo, Y. (2018). Experimental tests of slope failure due to rainfalls using 1g physical slope models. Soils and Foundations, 58(2), 290-305.

Cogan J., Gratchev I. (2019). A study on the effect of rainfall and slope characteristics on landslide initiation by means of flume tests. Landslides, 16(12): 2369-2379

Dahal R., Hasegawa S., 2008. Representative rainfall thresholds for landslides in the Nepal Himalaya. Geomorphology 100:429–443

Huang, C. C., & Yuin, S. C. (2010). Experimental investigation of rainfall criteria for shallow slope failures. Geomorphology, 120(3-4), 326-338.

Koizumi K, Sakuradani K, Oda K, Komatsu M, Ito S (2018). Relationship between initial quasi-saturated volumetric water content and rainfall-induced slope deformation based on a model slope experiment. J. Geo Eng., 13(4): 179-87

Wang, F., Dai, Z., Takahashi, I., & Tanida, Y. (2020). Soil moisture response to water infiltration in a 1-D slope soil column model. Engineering Geology, 267, 105482.

Xie J., Uchimura T., Chen P., (2019). A relationship between displacement and tilting angle of the slope surface in shallow landslides. Landslides, 16(6): 1243-1251

Xu, J., Ueda, K., & Uzuoka, R. (2022). Evaluation of failure of slopes with shaking-induced cracks in response to rainfall. Landslides, 19(1), 119-136.

CHAPTER 5

5. COMPUTER VISION-BASED MONITORING TECHNOLOGY AND METHOD OF INTERPOLATION

5.1 Introduction

Traditional sensors such as acceleration sensors mentioned above, extensometers and strain gauges (Dunnicliff, 1988; Malet et al., 2002; Corsini et al., 2005; Ramesh and Vasudevan, 2012) have always been used for the monitoring of ground movement and some deformation. For example, the exciter was used to give elastic waves to provide information on soil moisture and shear deformation (Tao et al, 2019). The current popular Micro-electro-mechanical systems (**MEMS**)-based equipment has be developed for remote monitoring with real-time data uploading functions (Meng and Ansari, 2013; Lin et al., 2015). However, Traditional sensors require professional techniques such as drilling, and they often only provide monitoring data information, which still has certain deficiencies in restoring the damage form (Su et al. 2009; Brückl et al., 2013). Thus, at present, due to the rapid development of computer science, more and more researchers have been using an instrument for real-time deformation or displacement monitoring based on the technology of computer vision, which presents the significant advantages of automatically identifying certain hazardous structures in the monitored area. Existing studies have shown that the variable monitoring of tunnels, the displacement of bridges, the expansion of cracks, and the inclination of landslides can all be applied by computer version based image processing (Saada et al., 1999; Miura et al., 2005; Lee and Shinozuka, 2006; Khuc and Catbas, 2017; Stark et al., 2017). A large number of scholars continue to optimize the software to improve the precision of captured images (Stanier et al., 2016).

In this study, several groups of experiments were carried out for the verification of the early warning system. However, the experimental method has several shortcomings. One of the most obvious problems is that only a single soil parameter and external influencing factors are considered in each experiment and only a limited number of cases can be obtained, which severely limits the evaluation and application value. Therefore, this chapter is also devoted to solving such problems and will use interpolation analysis to expand the limited data to the global, which improves a wider application. Research also carries out corresponding verification about the interpolation results.

5.2 Computer version-based particle tracking technology

When the slope is gradually saturated, particles in the slope will move slightly, so sensors will detect some slight deflection angles. In the study of using deflection angle to forecast the occurrence of landslide, research found that once the internal deflection of the slope exceeds the threshold, a landslide will occur rapidly (Uchimura et al., 2010) **Fig 5.1 (a)** presents the direction of the deflection angle in this research. Computer vision – based device will capture the movement of the targeted particles and define the time of the landslide, the soil point trajectory is shown in **Fig 5.1 (b).** In model tests, it can be used to track the movement of particles on the entire slope. When used in the field, it can be placed in the most dangerous areas for targeted monitoring, such as cracks or potential sliding surfaces. For the image or video data, motion analysis will also give the displacement of each tracking point and forecast the potential displacement of the landslide. DIPP-Motion, a full spec off-line motion analysis software for all needs based on normalized cross correlation, binarization of gray-scale, HLS color, and checker-marker tracking. All kinds of charts can be available for DIPP-Motion such as point trajectory, distance from the starting point, average point, rotation angle. In this research, point trajectory and displacement (distance from the starting point) will be obtained from the software. As **Fig 5.1 (b)** shows, the research marked the tracking points in the intended area before each test. Subsequently, a raspberry pi with image sensor was used to take a picture in every 5 seconds and uploaded images to the cloud. The motion analysis will be carried out once getting the new picture from the field so that the movement of the soil will be recorded in real time. Considering the displacement of each tracking point is also a very important reference index, because the time of landslide will be identified according to the movement of each tracking point. In addition, the deflection angle-displacement relationship can be used to predict the scope of the landslide in the future to make targeted protective measures (Xie et al., 2019). The specific calculation principle and calculation formula are also shown in the Fig.5.1. The calculation principle, tracking method and error analysis of particle tracking, research in (Take 2015; Stanier et al., 2016) has been introduced in detail.

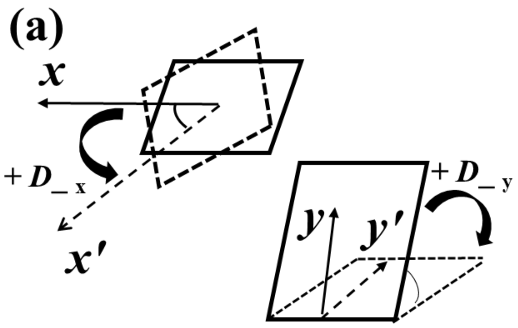

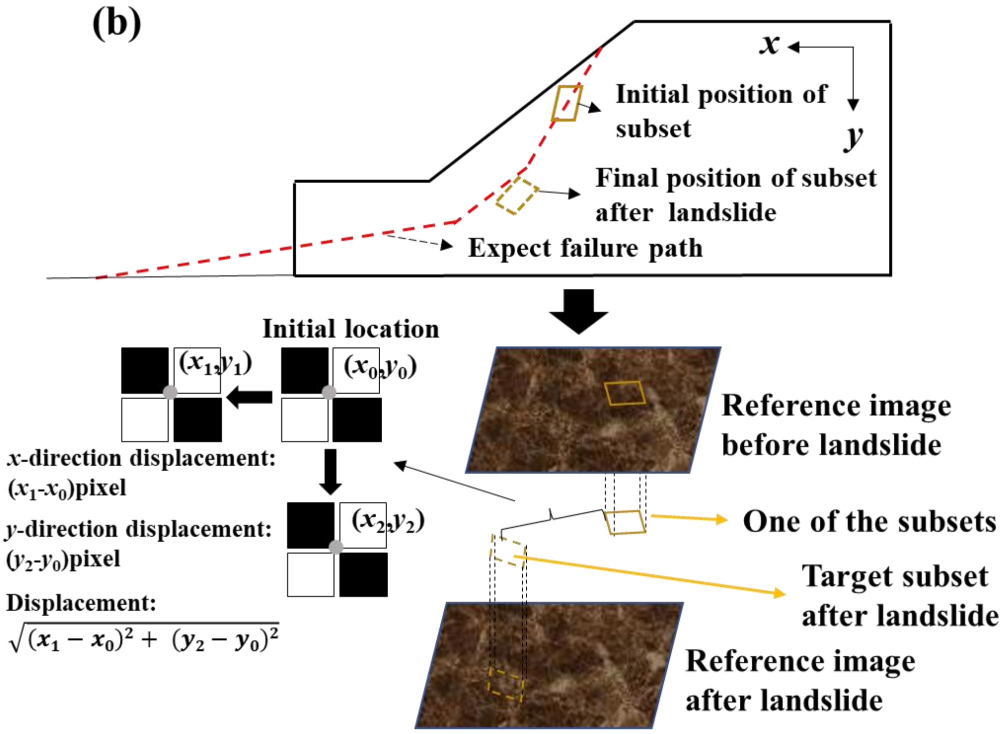

Fig 5.1. Soil flow in motion analysis: (a) Particle movement direction determination; (b) Displacement determination by motion analysis

5.2.1 PIV analysis of rainfall-induced landslide experiments

As shown in **Fig 5.2,** two cameras are placed on the side and front of the model to capture particle movement during the sliding, which are also used to identify the occurrence time of each landslide. Since the landslide occurs at the stage when the slope gradually reaches saturation, the initial moisture content has less influence on the failure mode and particle flow, while the rainfall intensity has a significant effect on the particle flow velocity and the movement trajectory. Therefore, the motion analysis of sandy slopes is mainly carried out on the effects of different rainfall intensities.

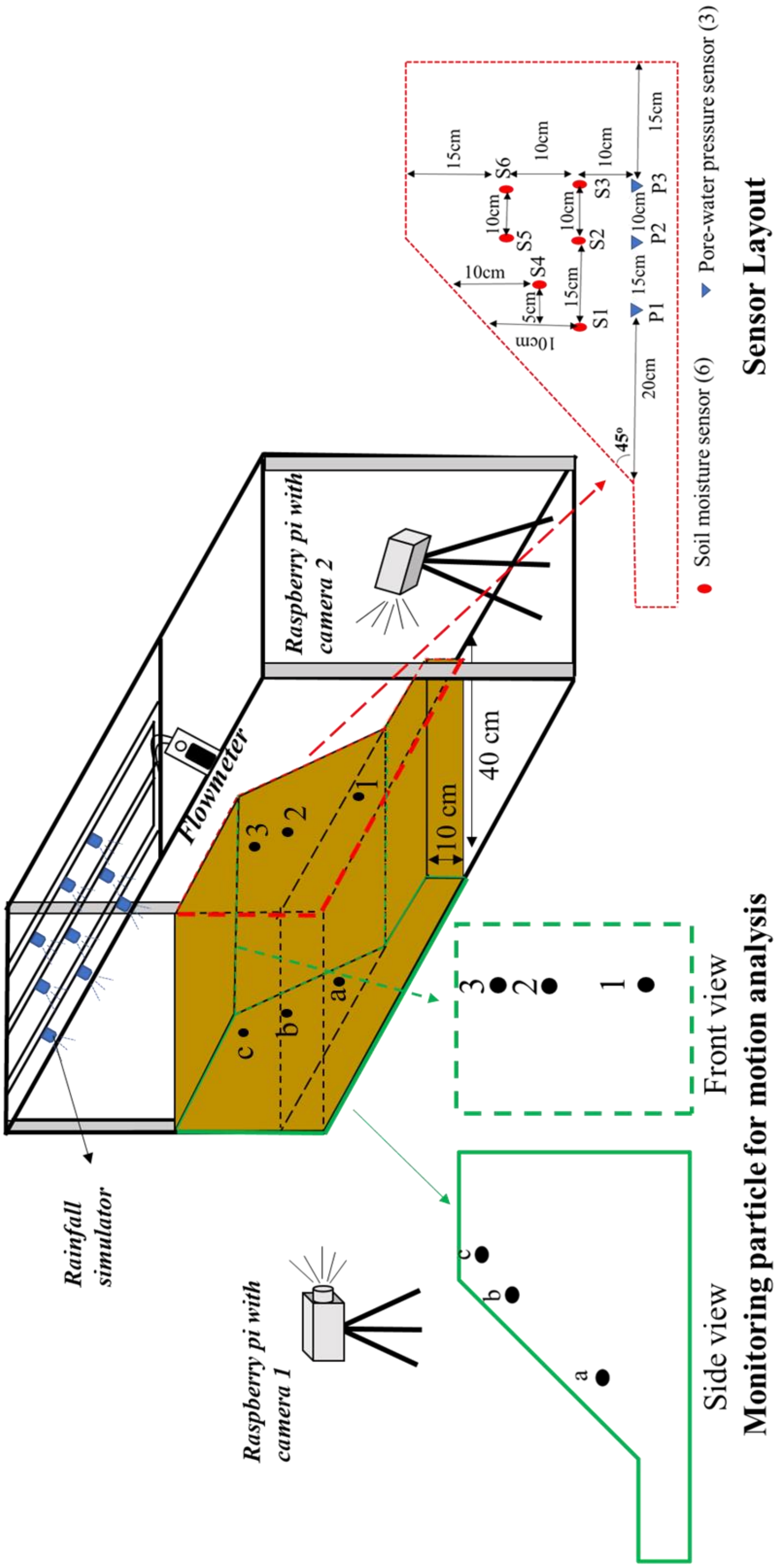

Fig 5.2 Cameras setup in the experiment and monitoring points disturbtion

As already explained in the above, three shallow landslides induced by rainfall are recorded in each case. **Fig 5.3** to **5.5** show the characteristics of shallow landslides on sandy slopes, the upper picture of each figure shows the particle motion trajectory and velocity information, and the lower picture shows the cloud map of the particle motion velocity. Occurrence time of the three shallow landslides in each case was shown in the figures. It can be clearly found that the three shallow landslides spread from the slope toe to the upper part. The results for Test A in **Fig 5.3** show that the third landslide did not even reach the top of the slope, which is inconsistent with Test B and Test C. It can be implied that the low rainfall intensity causes the groundwater level to rise slowly, and the rainwater impact is weaker. The maximum particle motion velocity vectors in the three cases are 0.126 mm/s, 0.138 mm/s and 0.235 mm/s, respectively. According to the velocity result under rainfall intensity 100 mm/h obtained by Chueasamat (2018), the particle motion velocity given in this study is lower, because the previous study considered relative density D_r=0, while the relative density in this study is 50%. Greater relative density will undoubtedly make the slope more stable and thus the flow of particles will be slower in the event of a landslide. From the results in the cloud map, it can be seen that with greater rainfall intensity, the sliding volume of the slope is larger and the peak velocity coverage is wider within the slope. **Fig 5.6** to **5.8** show the characteristics of shallow landslides from the top view. A notable phenomenon is that the sliding velocity of the slope observed from the top is greater than that of the side. Movement velocity increased by about 20%. A reasonable explanation is that although we have done lubrication, it is still difficult to suppress the reduction effect of boundary friction on soil motion.

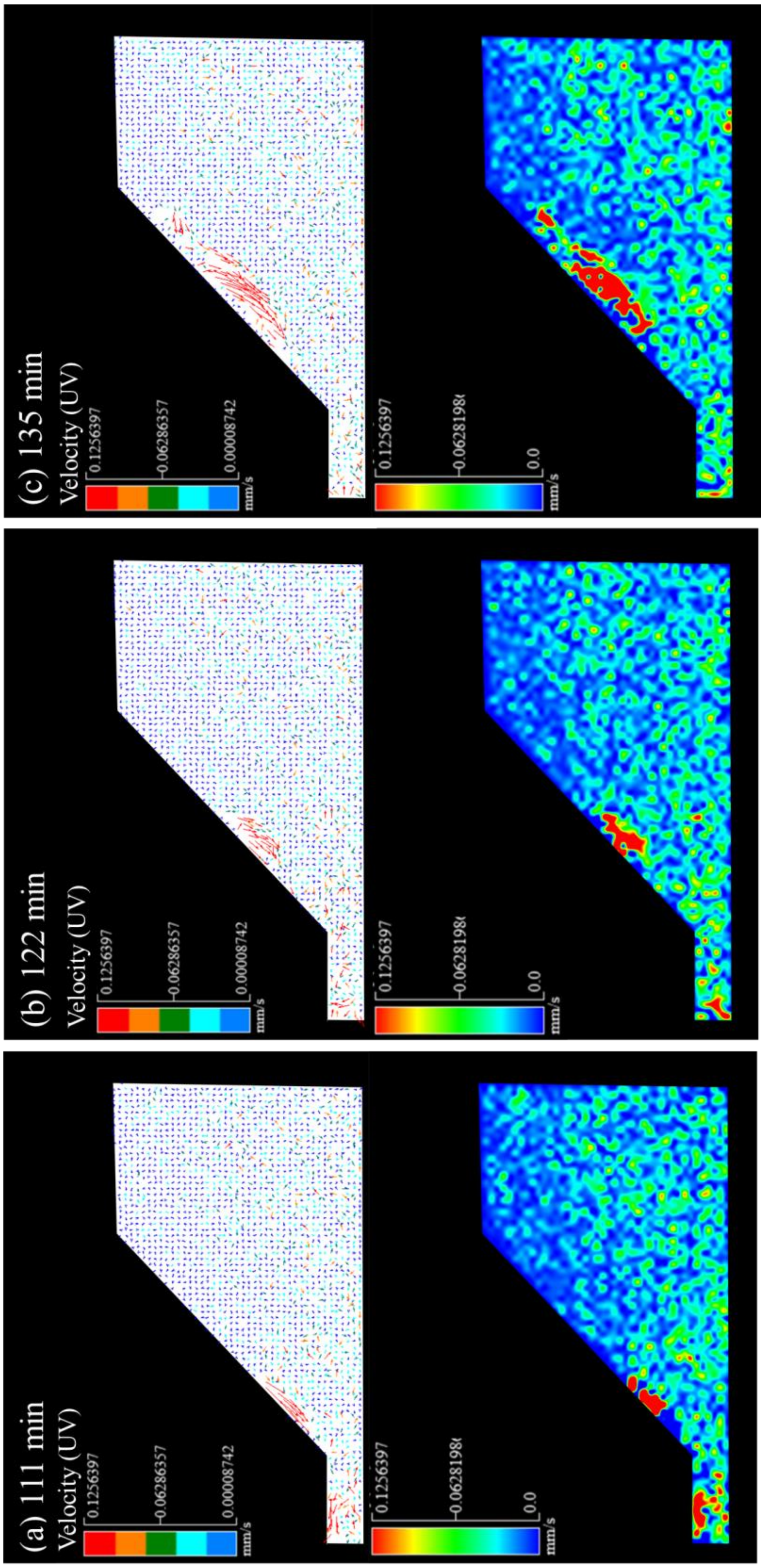

Fig 5.3 Result of PIV on Test A (Side view)

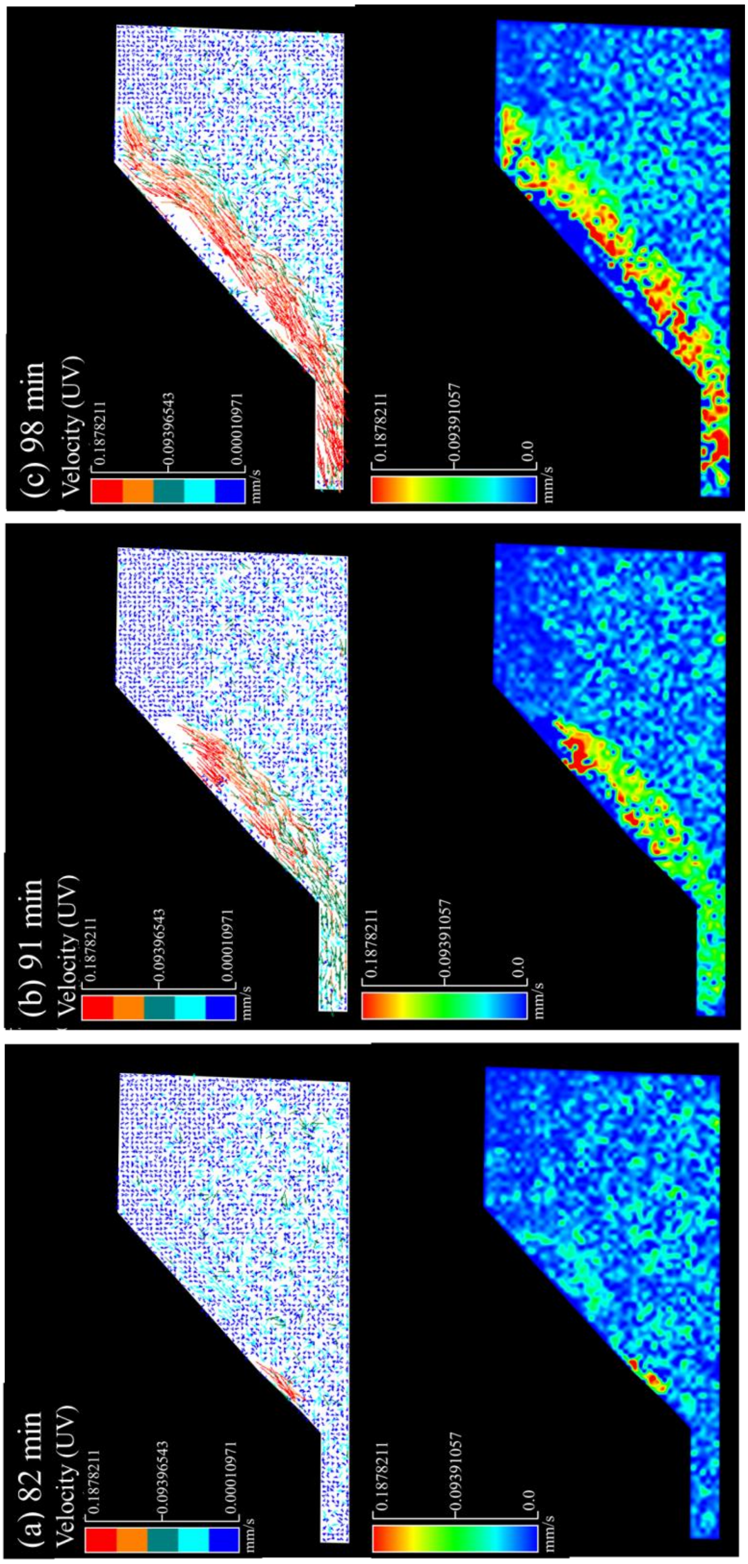

Fig 5.4 Result of PIV on Test B (Side view)

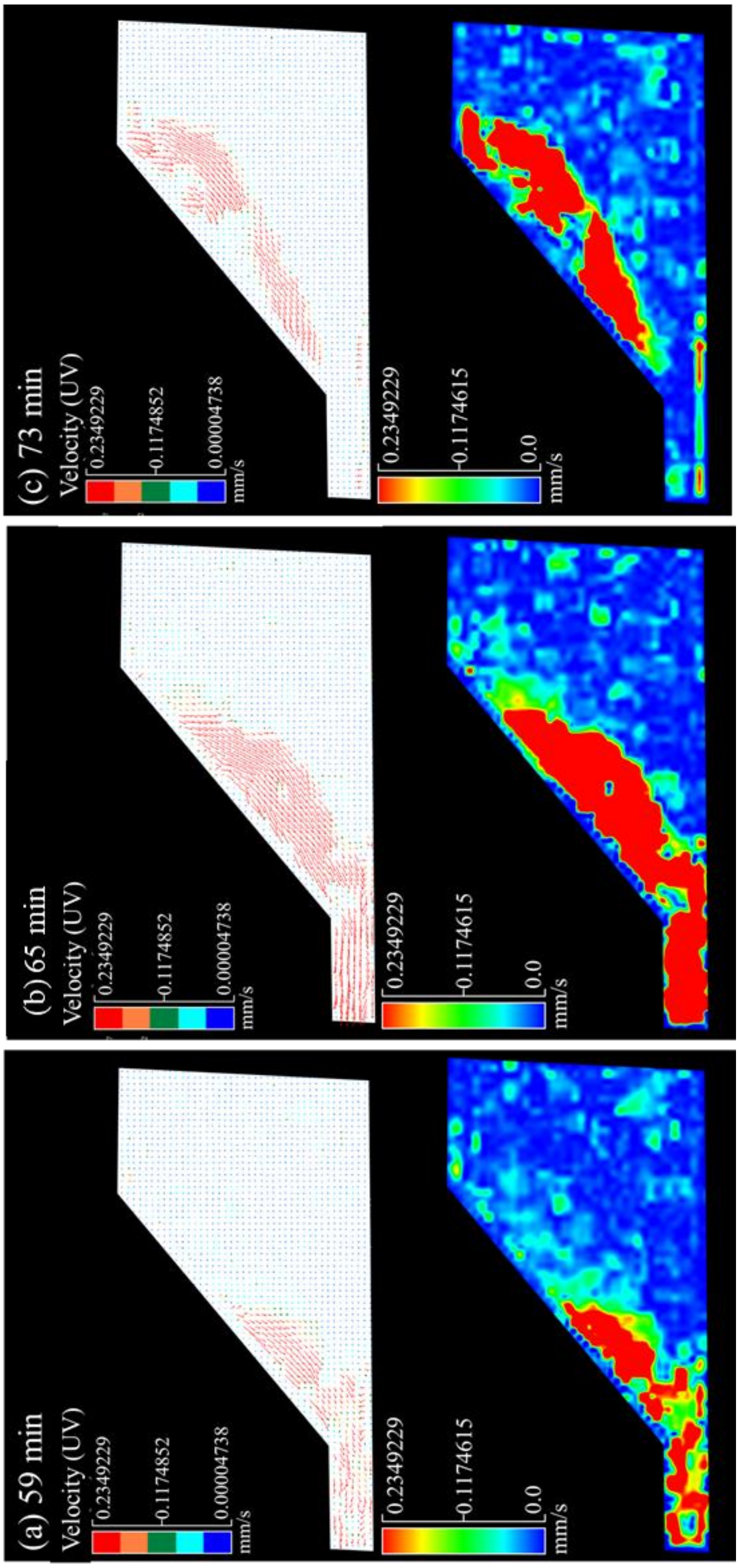

Fig 5.5 Result of PIV on Test C (Side view)

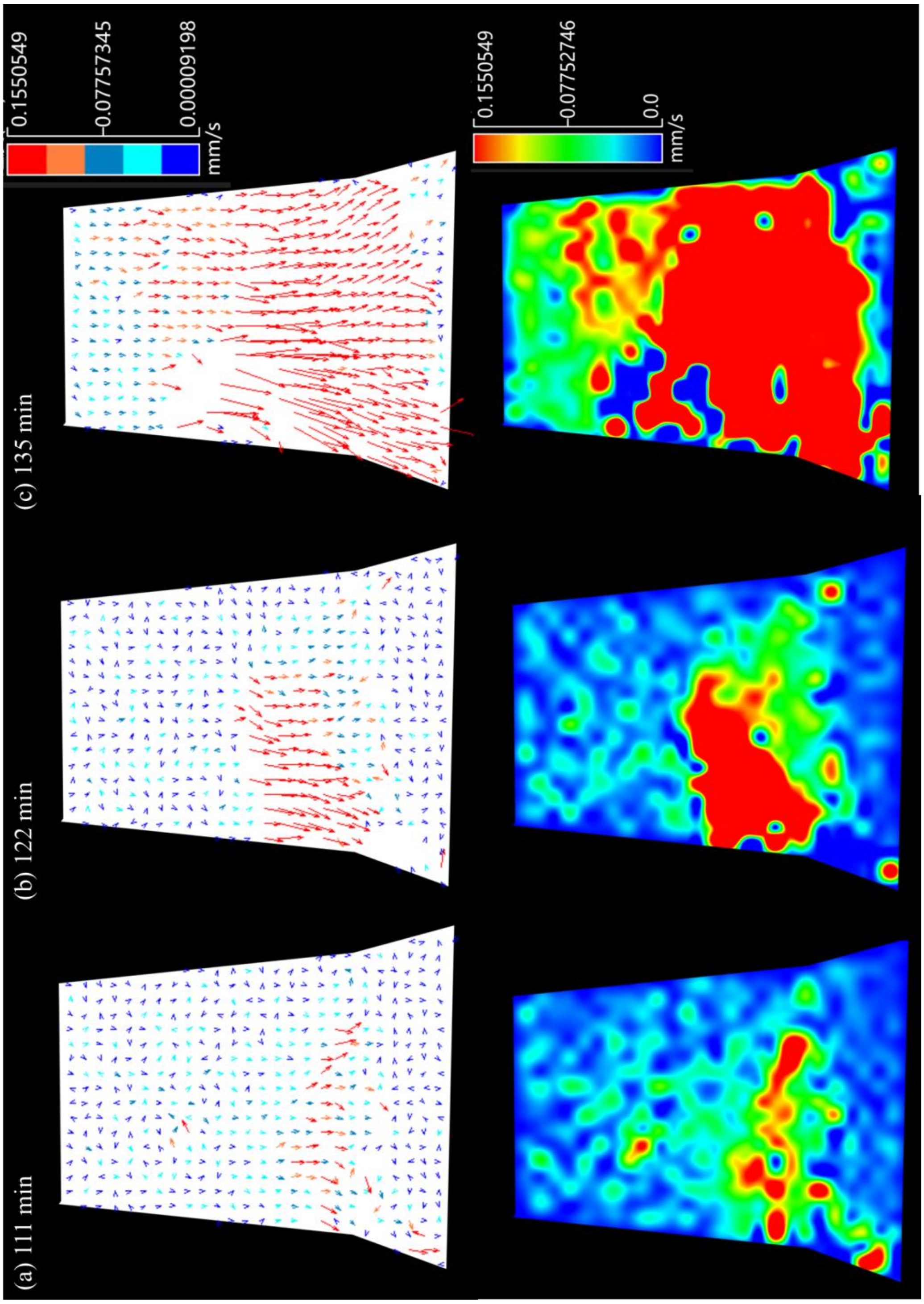

Fig 5.6 Result of PIV on Test A (Front view)

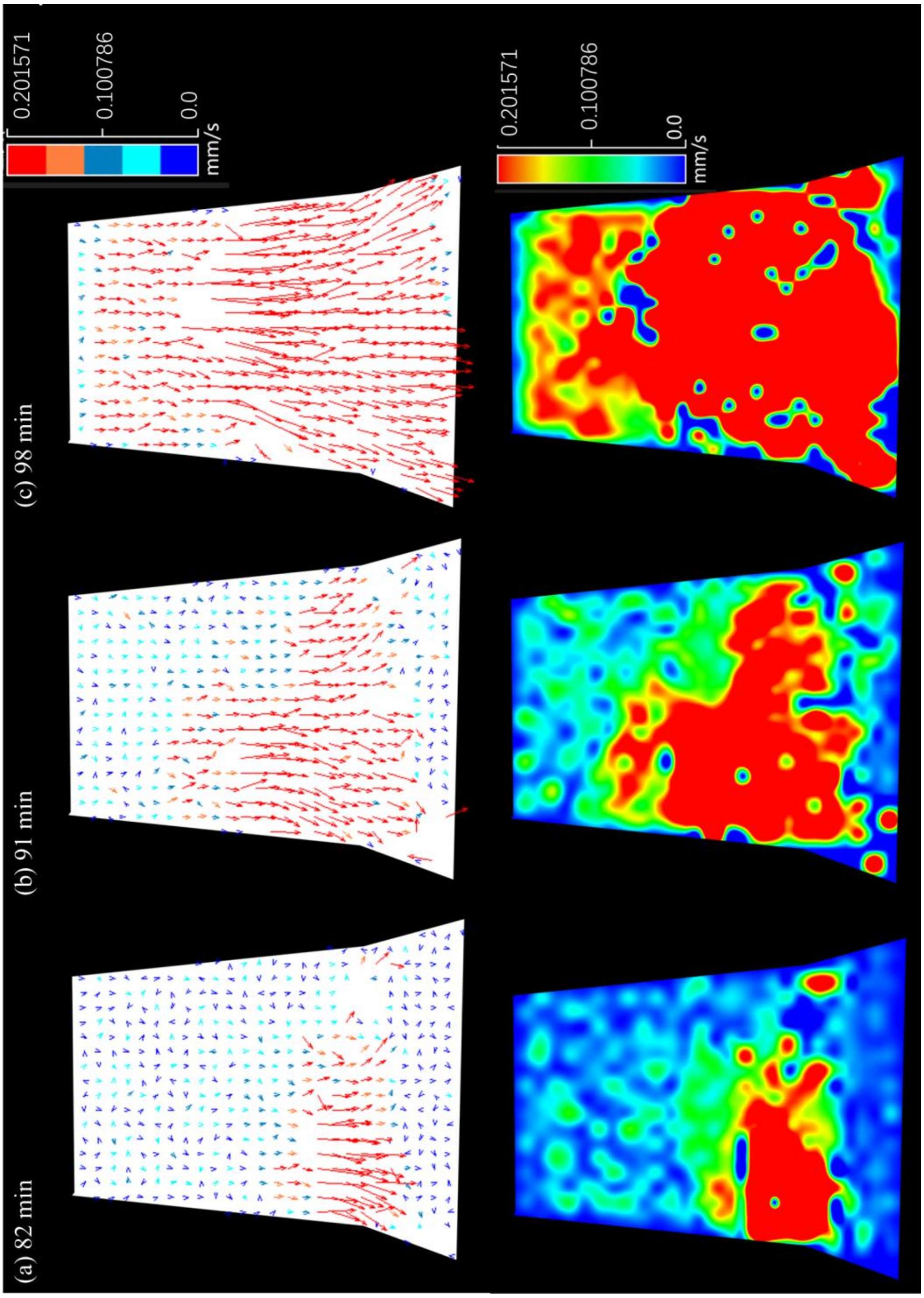

Fig 5.7 Result of PIV on Test B (Front view)

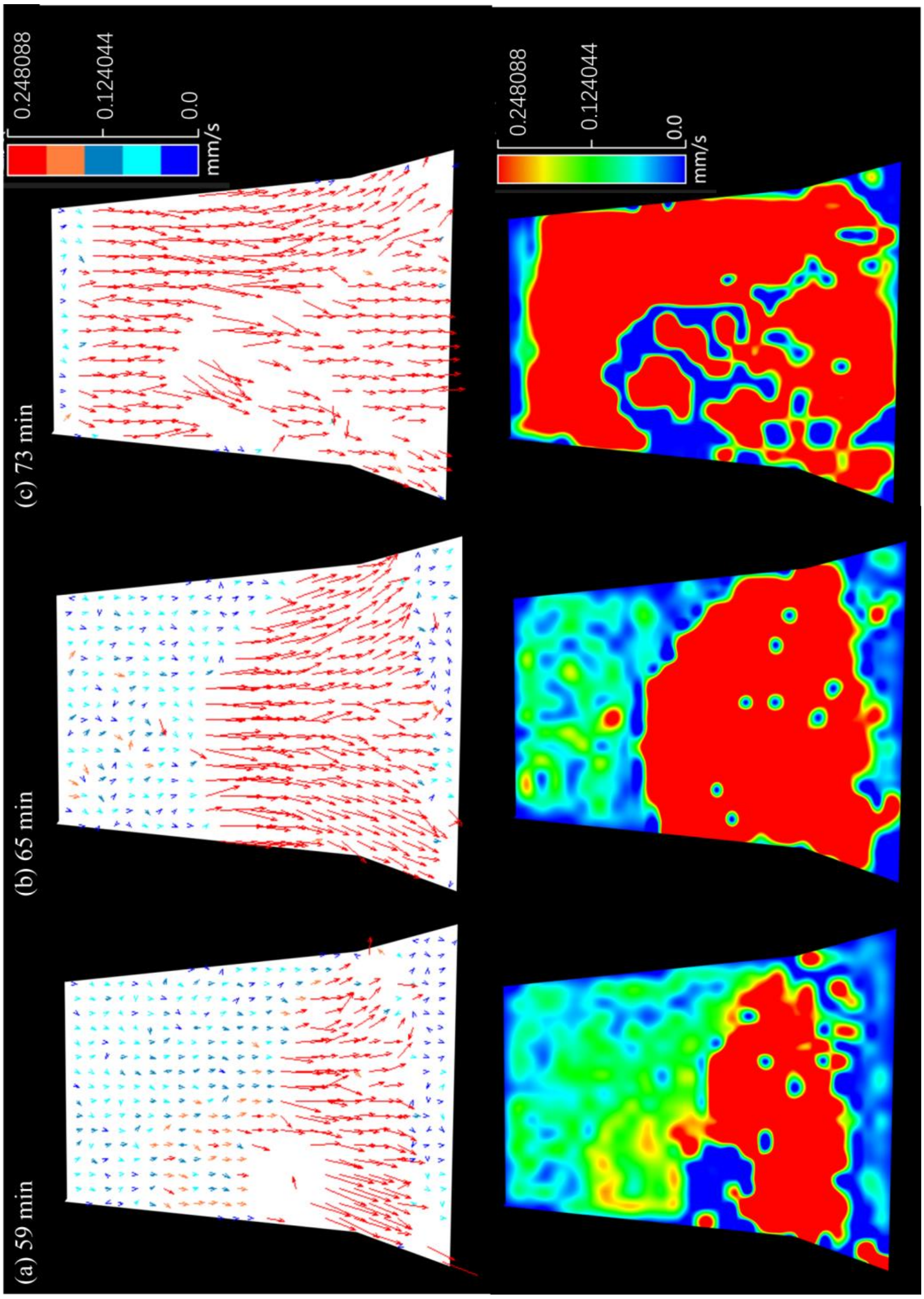

Fig 5.8 Result of PIV on Test C (Side view)

5.2.2 Displacement of monitoring points

The left corner of **Fig 5.2** shows the information of tracking points in both the side view and front view. From the side view, 3 tracking points (T_a, T_b, and T_c) were marked along the slope surface. T_a always reacts faster and has longer displacement than other points, because T_a is located in the first shallow landslide area, prompting it to move the most immediately. **Fig 5.9 (a)** shows that the maximum landslide displacement T_a in the three cases is almost the same. The reason is that the three shallow landslides all promote the sliding of the Ta area close to the slope toe, and the sliding trend is consistent. However, the sliding displacement of T_c at the top regions in the three cases is quite different; most notably, the sliding distance for Test A is even lower than 10 cm. In Test A, there is no final large-scale landslide near T_c area, and the displacement comes from the sliding of the bottom part, which promotes T_c small-scale sliding.

From the front view, 3 tracking points (T_1, T_2, and T_3) were marked from the slope bottom to upward. The distribution of monitoring points is roughly the same as the side view, the displacement produces a similar trend. However, two significant differences can be found. One is that the sliding start time of the monitoring point of the front view is faster than that of the side view. The same situation was also observed in the experiment, that is, there will be cracks on the slope surface before the landslide occurs, and the cracks generally expand from the center to both sides, which causes the middle area to slide faster than the two sides from the front view. The second is that the displacement monitoring from the front view is larger, the maximum displacement is 25.05 cm, 28.11 cm, and 30.41 cm, while the maximum displacement of the side view is 23.05 cm, 21.32 cm, and 20.71 cm respectively. The research thinks that this is because of the boundary force on both sides. Although the research has lubricated the glass on both sides to reduce unnecessary resistance, there is still a small force that hinders sliding.

The position of three monitoring points on each side is relatively consistent with the sliding range of the three shallow landslides. Therefore, it can also be found from **Fig 5.9** that the time of rapid displacement accumulation of the three monitoring points on each view is quite close to the occurrence time of each shallow landslide defined by real-time image observation. For example, the time of the first shallow landslide in three cases is 58 min, 82 min, and 110 min, the time for more than 1 cm displacement of T_a is 61 min, 84 min, and 113min from the side view, while time for more than 1 cm displacement of T_1 is 60 min, 83 min and 111 min from the front view.

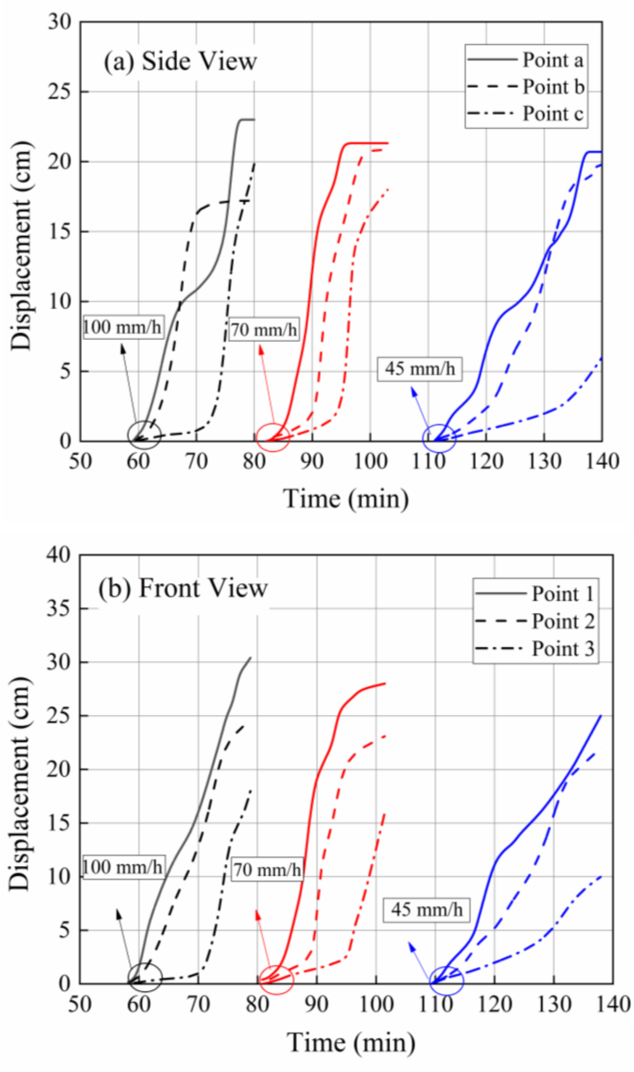

Fig 5.9 Displacement of tracking points under different rainfall intensity: (a) Side view; (b) Front view

5.3 Interpolation analysis

In order to predict the results for intermediate cases, for which the experiments were not performed, an interpolation of the observed results is performed based on the limited experimental data. For this, a linear polynomial function is used to predict new data points for curve fitting within a discrete set of known data points (Hogben, 2006). The interpolation results cover the entire range within the rainfall intensity of 45 mm/h - 100 mm/h and the initial moisture content of 8%-17%. The interpolation analysis of volumetric moisture content and factor of safety Fs is carried out for locations S1 and S6. The main reason for selecting these two points is that S1 is one of the fastest responding monitoring points to the 5 stages classified in this study. While S6 is the last sensor to detect the rise of the groundwater table. The points P1 and P3, which are the fastest and slowest monitored pore water pressure rises, are also used for interpolation analysis. These two points are located on the same vertical line as S1 and S6, respectively.

5.3.1 Interpolation result on experimental data

3D surface plots can cover a wider range of parameter-changing information and facilitate the presentation of more conditions. **Fig 5.10** shows the 3D surface plots from interpolation analysis under different rainfall intensity. The abscissa records the rainfall elapsed time (0-140min) and rainfall intensity (45-100mm/h), and the ordinate records the moisture content, factor of safety F_s and pore water pressure respectively. **Fig 5.11** presents the 3D interpolation surface under different initial moisture content. The difference from Figure 10 is that the rainfall intensity on the abscissa is replaced by the initial moisture content (8%-17%). 3D results from interpolation analysis cover a wider area, which effectively solves the limitations of the case samples in the experimental method. However, it is very necessary to judge the accuracy of the interpolation results, so this study carried out verification work.

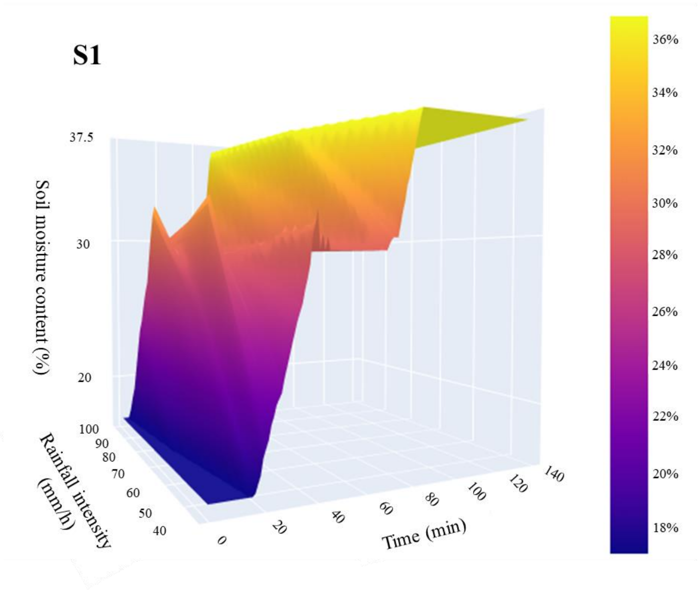
S1
Soil moisture content (%)
37.5
30
20
Rainfall intensity (mm/h)
100
90
80
70
60
50
40
0
20
40
60
80
100
120
140
Time (min)
36%
34%
32%
30%
28%
26%
24%
22%
20%
18%

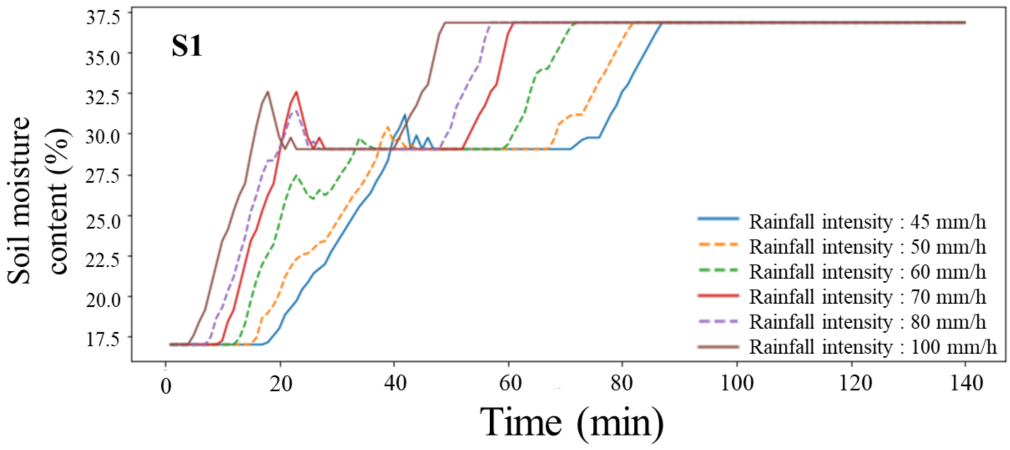
S1
Soil moisture content (%)
37.5
35.0
32.5
30.0
27.5
25.0
22.5
20.0
17.5
0
20
40
60
80
100
120
140
Time (min)
Rainfall intensity : 45 mm/h
Rainfall intensity : 50 mm/h
Rainfall intensity : 60 mm/h
Rainfall intensity : 70 mm/h
Rainfall intensity : 80 mm/h
Rainfall intensity : 100 mm/h

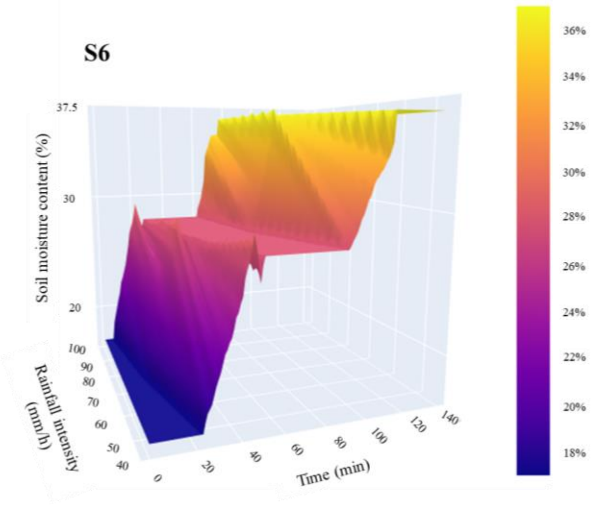
S6
Soil moisture content (%)
37.5
30
20
Rainfall intensity (mm/h)
100
90
80
70
60
50
40
0
20
40
60
80
100
120
140
Time (min)
36%
34%
32%
30%
28%
26%
24%
22%
20%
18%

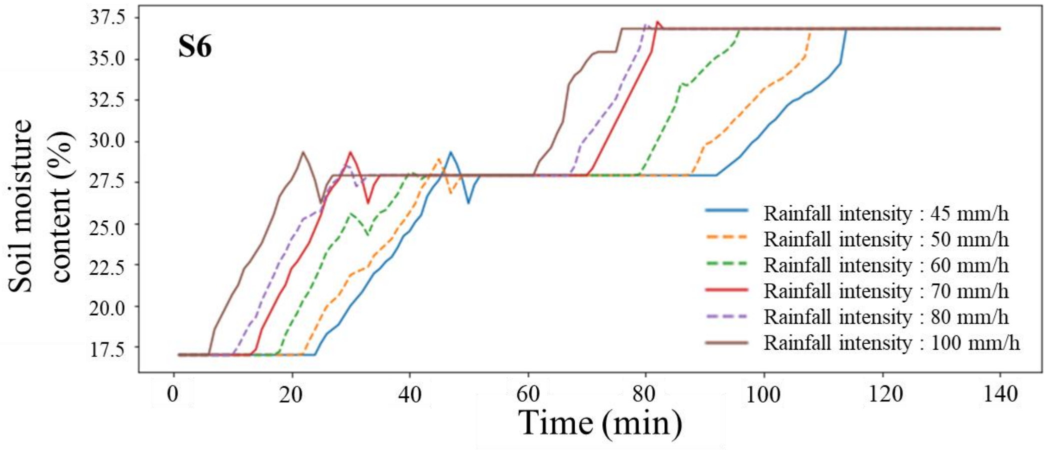

(a) Interpolation results in soil moisture content

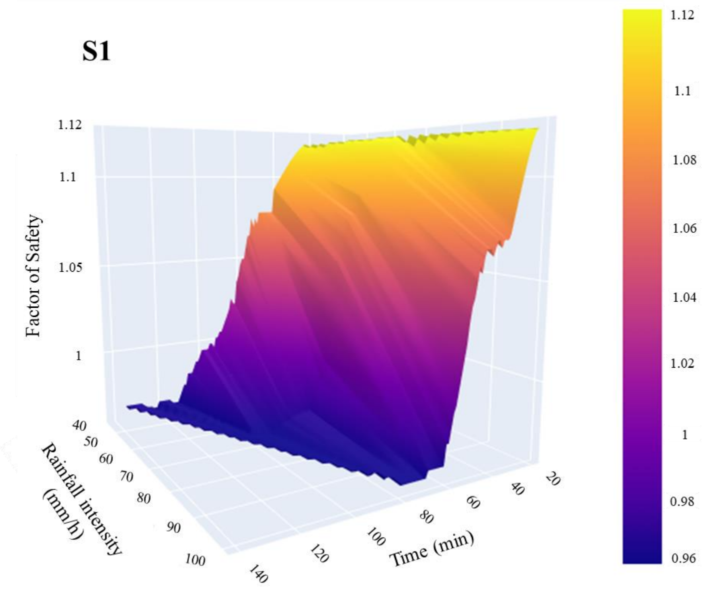

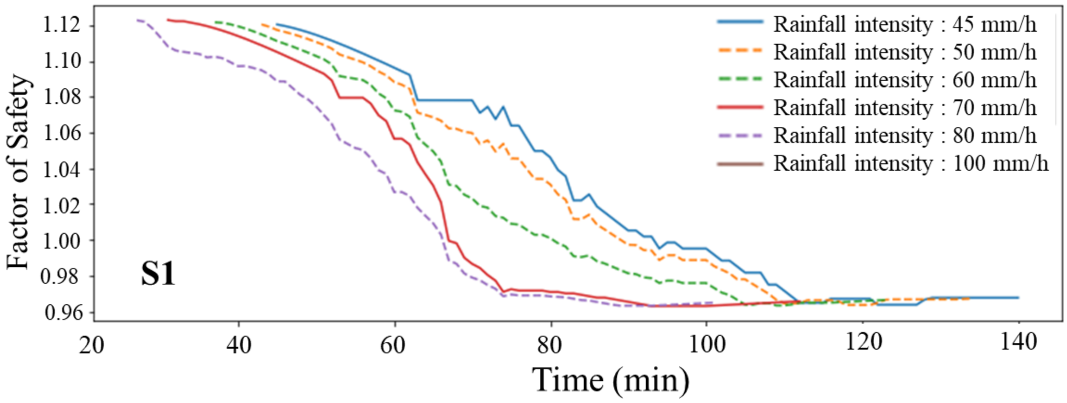

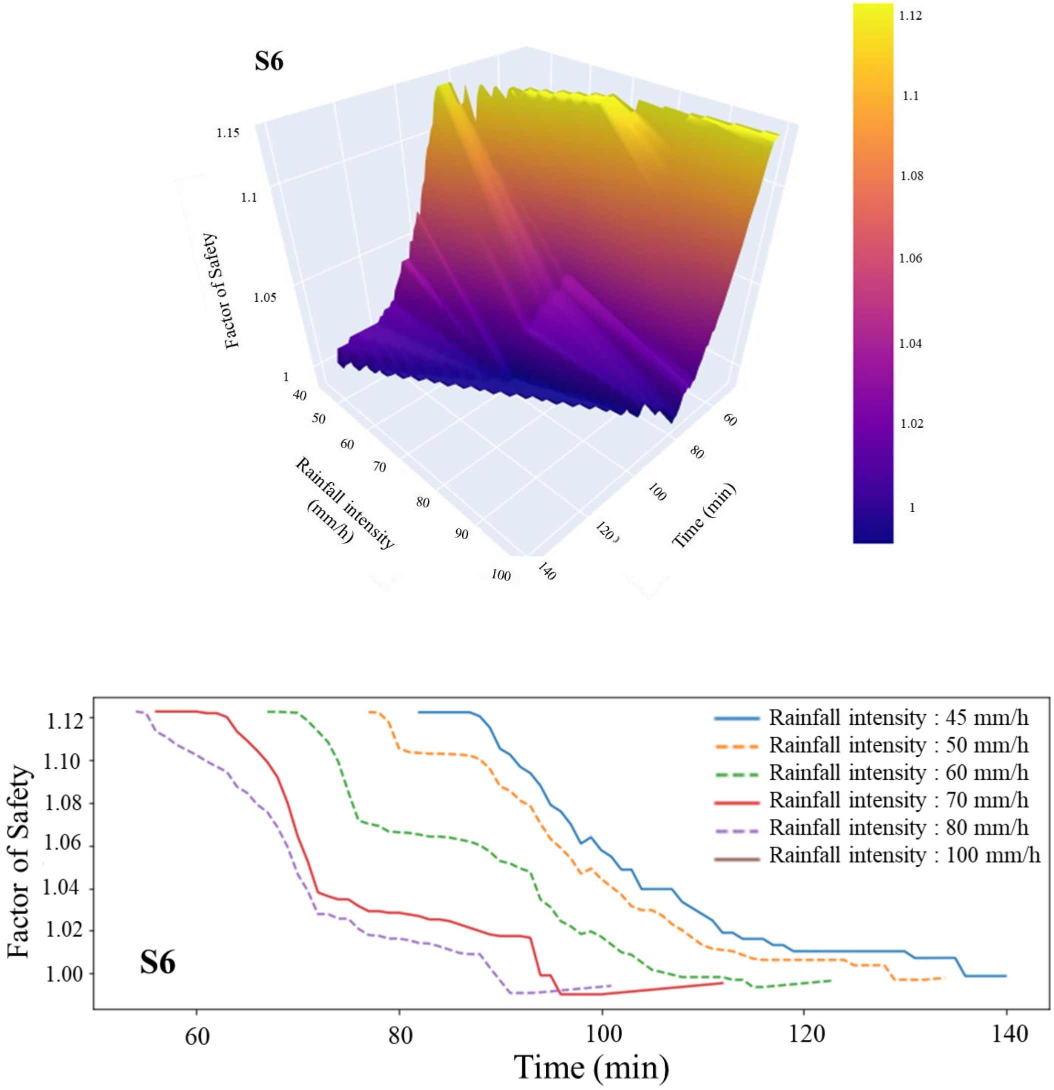

(b) Interpolation results in Factor of Safety

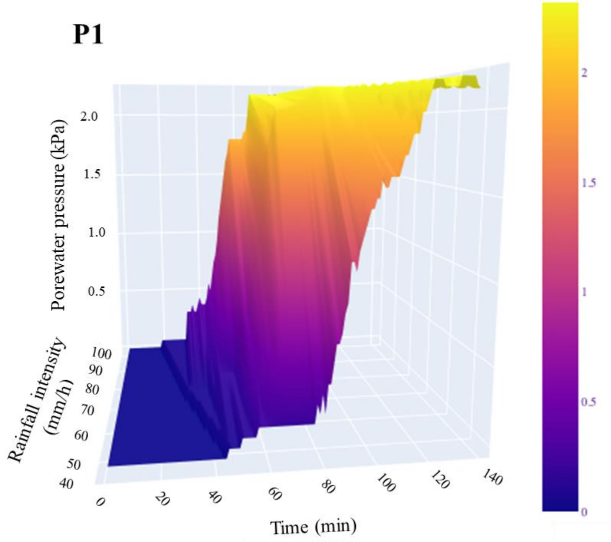

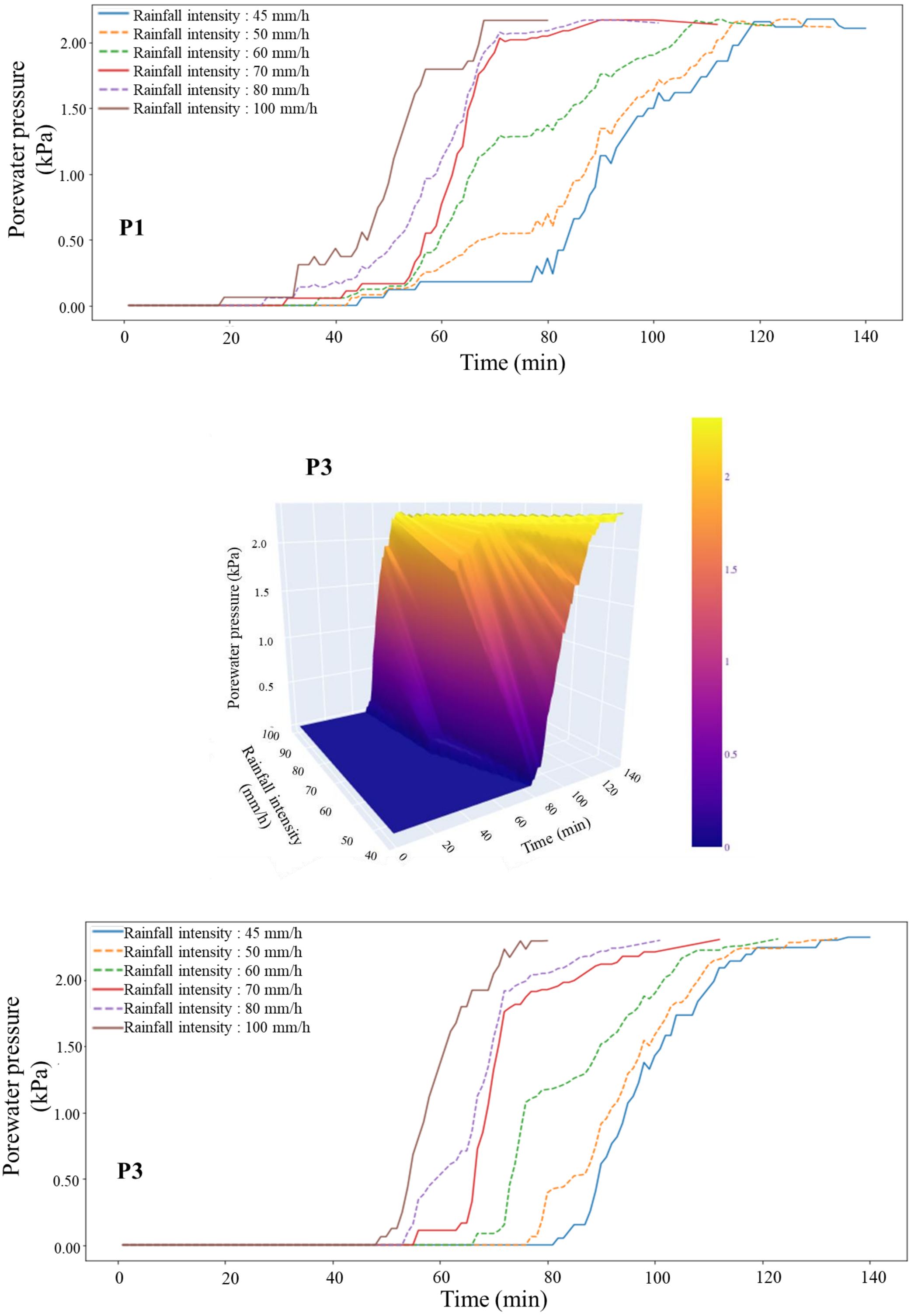

(c) Interpolation results in Pore water pressure

Fig 5.10 Interpolation results under different rainfall intensity: (a) Interpolation results in soil moisture content; (b) Interpolation results in Factor of Safety; (c) Interpolation results in Pore water pressure

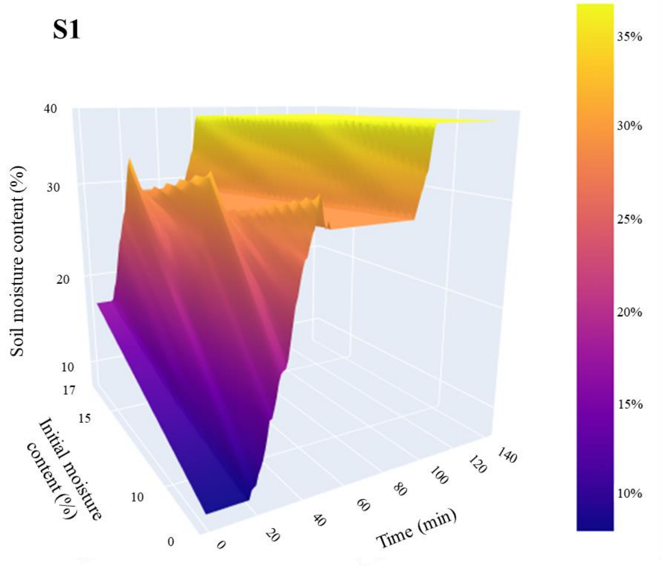
S1
Soil moisture content (%)
40
30
20
10
17
15
10
0
Initial moisture content (%)
0
20
40
60
80
100
120
140
Time (min)
35%
30%
25%
20%
15%
10%

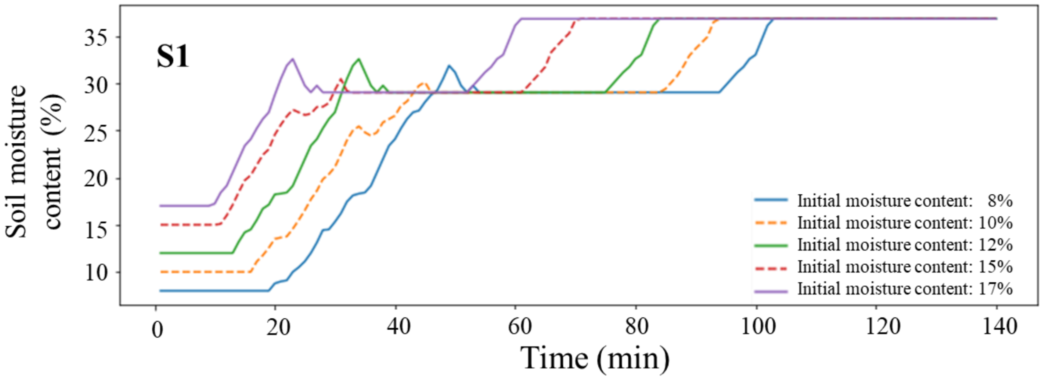
S1
Soil moisture content (%)
35
30
25
20
15
10
0
20
40
60
80
100
120
140
Time (min)
Initial moisture content: 8%
Initial moisture content: 10%
Initial moisture content: 12%
Initial moisture content: 15%
Initial moisture content: 17%

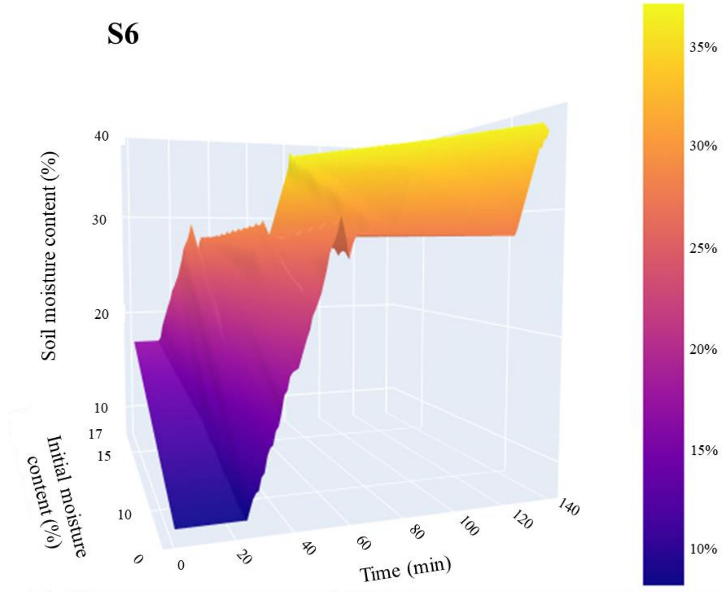
S6
Soil moisture content (%)
40
30
20
10
17
15
10
0
Initial moisture content (%)
0
20
40
60
80
100
120
140
Time (min)
35%
30%
25%
20%
15%
10%

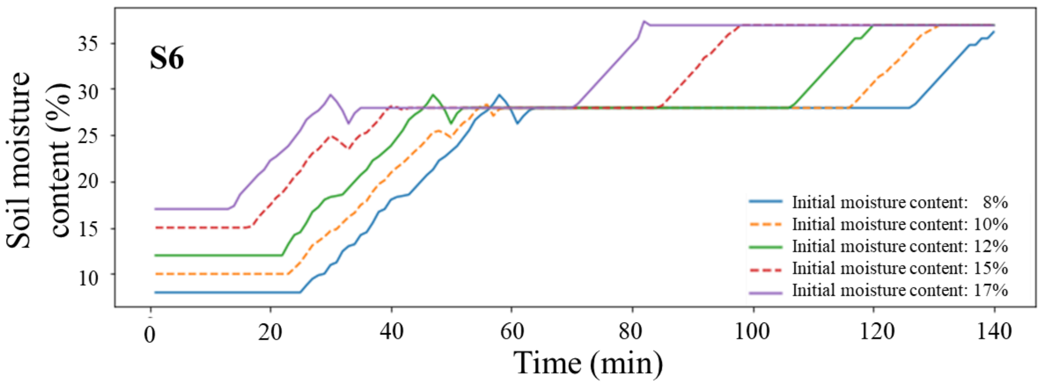

(a) Interpolation results in soil moisture content

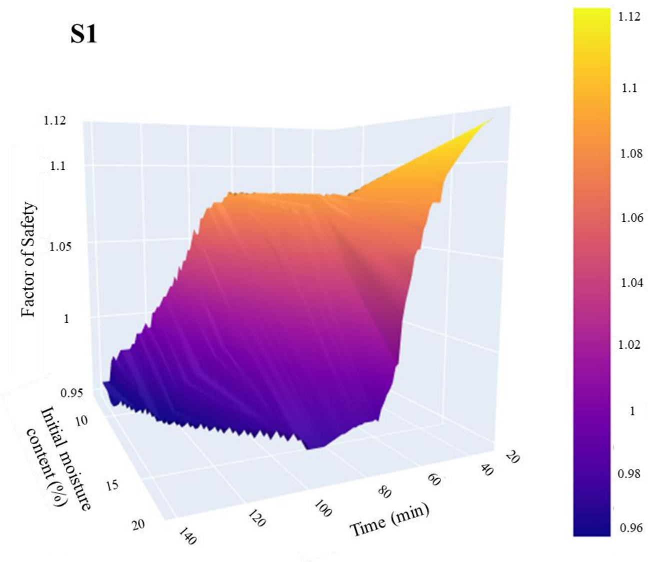

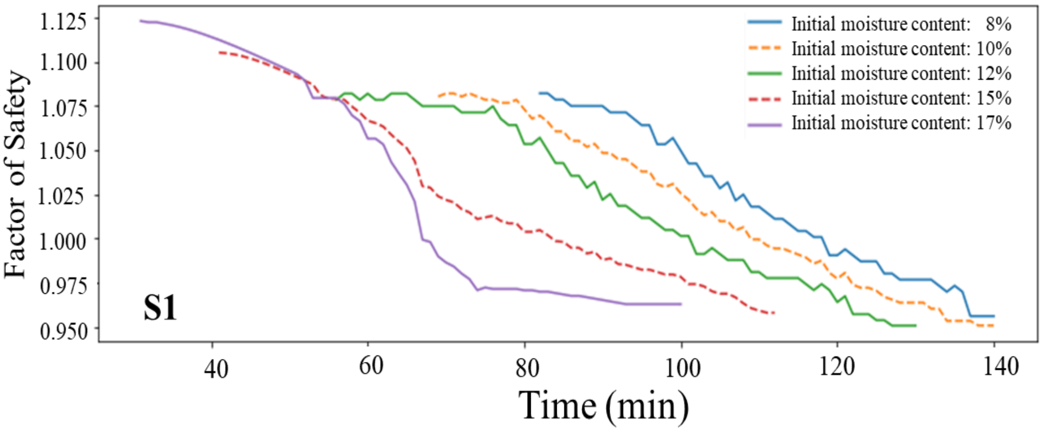

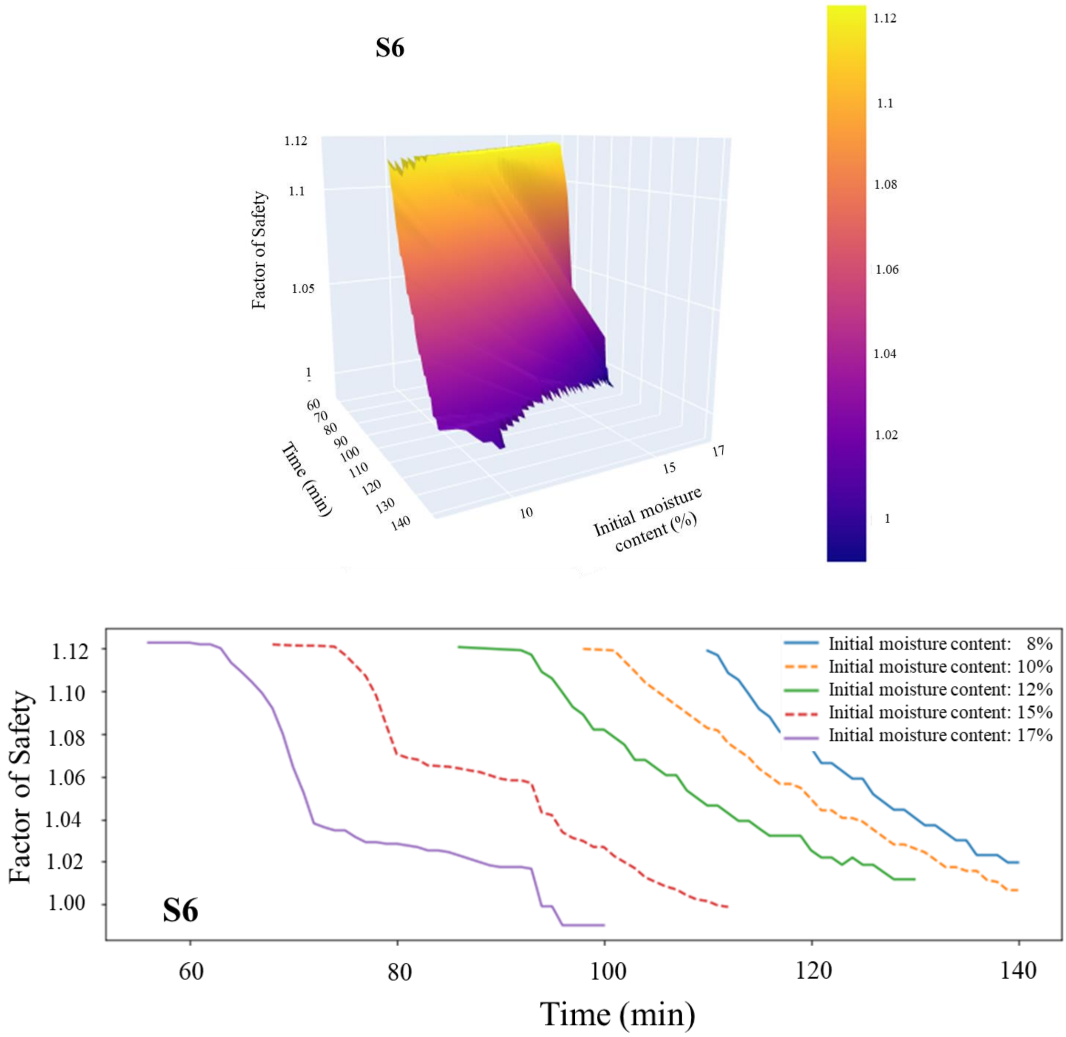

(b) Interpolation results in Factor of Safety

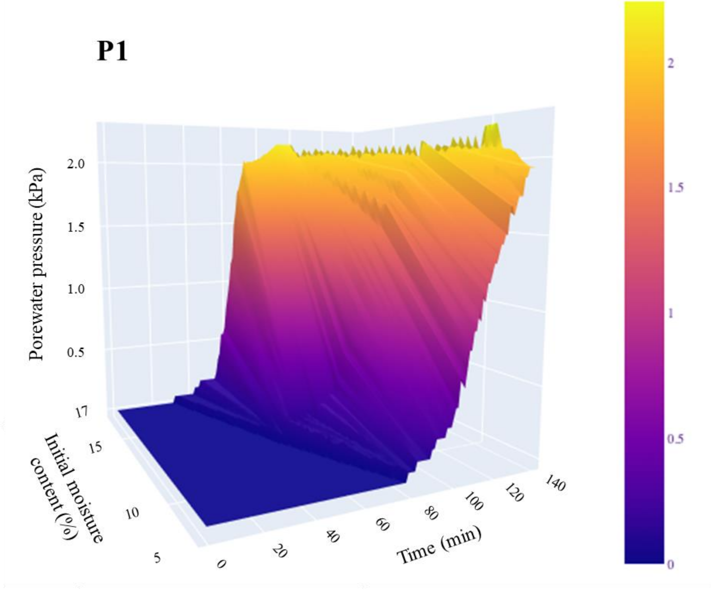

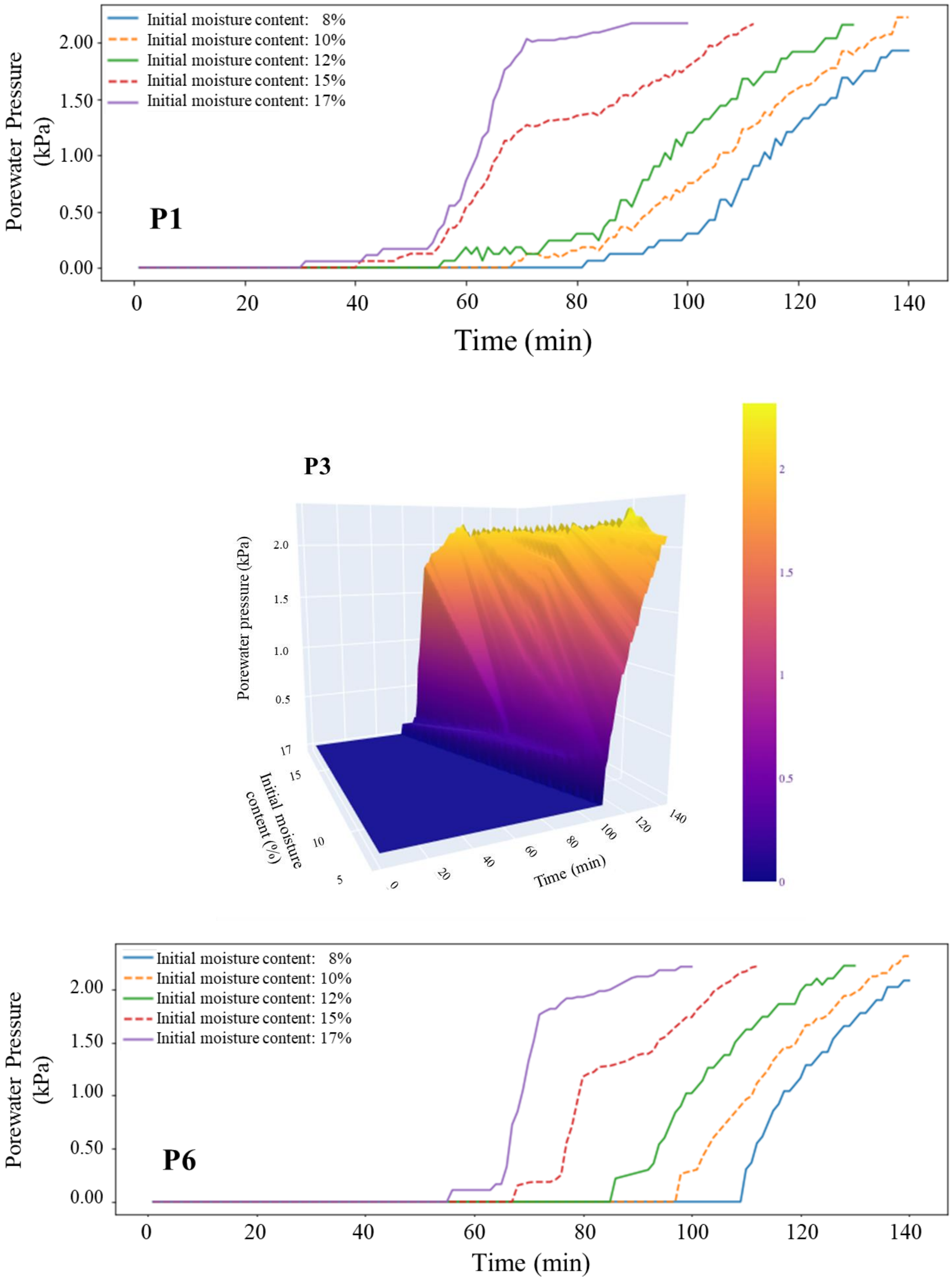

(c) Interpolation results in Pore water pressure

Fig 5.11 Interpolation results under different initial moisture content: (a) Interpolation results in soil moisture content; (b) Interpolation results in Factor of Safety; (c) Interpolation results in Pore water pressure

5.3.2 Verification of interpolation results

This study is supplemented by an additional case of Test F (60mm/h, 17% initial moisture content) in Table 3, and it is compared with the interpolation results. To quantify the deviation value, the relative error norm ε has been evaluated by the following formula:

$$\varepsilon = \sqrt{\frac{\sum_{j}^{N}(D_{mj} - D_{ij})^{2}}{\sum_{i}^{N} {D_{mj}}^{2}}} \tag{6}$$

where D_m is the measured data of verification points in the model test, and D_i is the interpolation result data of verification points. / D_m - D_i / is the deviation of monitoring and interpolation results. N is the number of the monitoring objects. **Fig 5.12** shows the volumetric moisture content and pore water pressure and compares the results with the interpolation results. Each set of images presents a graph of the data results on the left and the relative error norm ε on the right. It is obvious that most of the relative error norms are below 20%. Therefore, it can be concluded that the model proposed in this work can basically predict the distribution of moisture content and evolution of pore water pressure at different rainfall duration. Research summarizes the time information of the five stages under the interpolation results in **Table 5.1**. It can be found that the interpolation results also show an increasing trend, which is quite similar to the experimental results. Although the result obtained by interpolation takes less time to reach each state, which presents a more unfavorable value than experimental results, these values are within a reasonable range, and a lower value will provide an earlier warning, and it will avoid the problems such as lag in early warning work and untimely crowd evacuation.

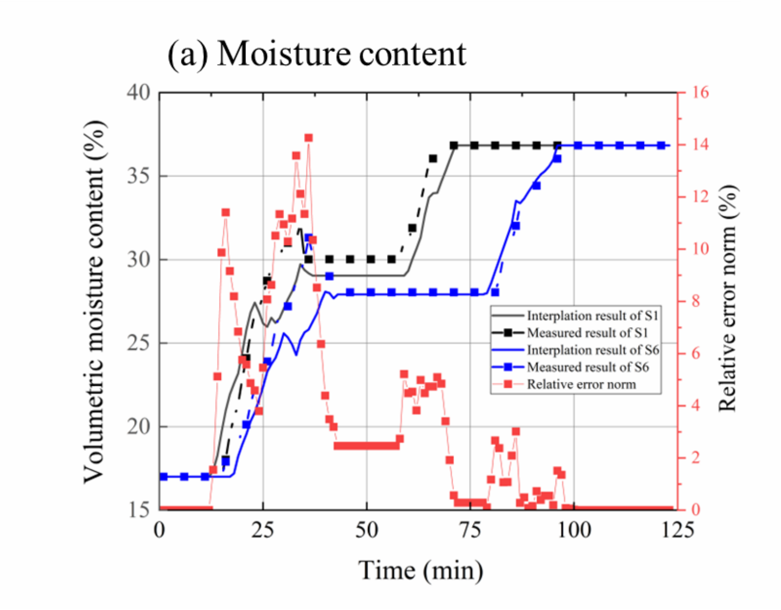

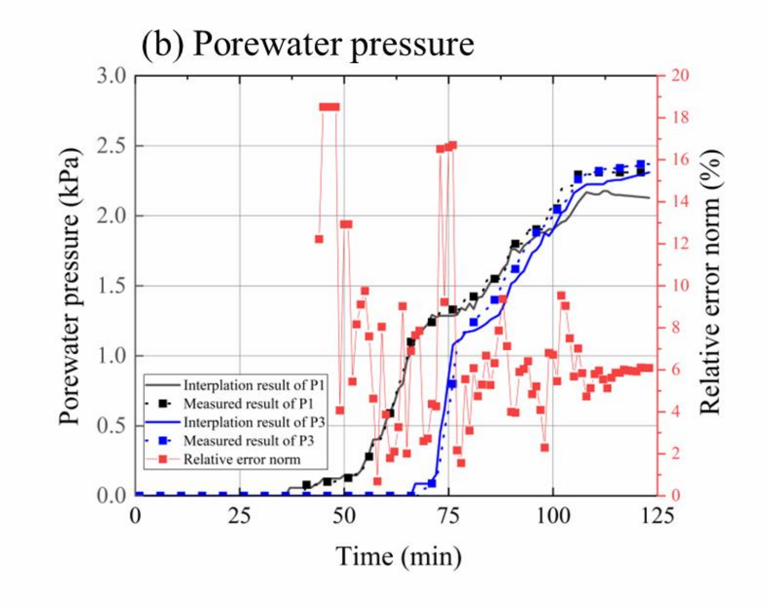

Fig 5. 12 Comparison of interpolation results and relative error norm under 60 mm/h: (a) Moisture content; (b) Porewater pressure

Table 5.1 Test and interpolation time of each Stage during rainfall

Data Sources	Sensor	Time of each Stage (min)				
		Stage I	Stage II	Stage III	Stage IV	Stage V
Model test	S1	40	46	77	94	92
	S6	49	69	103	116	---
Interpolation analysis	S1	37	45	72	85	92
	S6	42	67	96	107	---

As mentioned that the factor of safety ***F*s** is obtained from the monitoring result of moisture content and pore water pressure. The research proposes a cross-validation method: moisture content and pore water pressure obtained by interpolation are used to calculate the ***F*s** by Eq. (1), then calculated results of ***F*s** are compared with the ***F*s** obtained by the interpolation method to verify the accuracy of the interpolation results. Results in **Fig 5.13** show that most of the interpolated results are also lower than the actual calculated Fs because of the underestimation of the groundwater table and moisture content. Since the variation range of ***F*s** is very small, the relative error norm of the obtained ***F*s** is all less than 4%, which is much lower than the value of a single parameter.

It should be worth noting that the interpolation result was proposed based on the monitoring data of sandy soil, so it makes sense to predict the soil moisture distribution, groundwater table migration and local factor of safety level on the sandy slope. However, it has to be clarified that the data obtained by the interpolation method in this study can only be used as a reference for constant continuous rainfall.

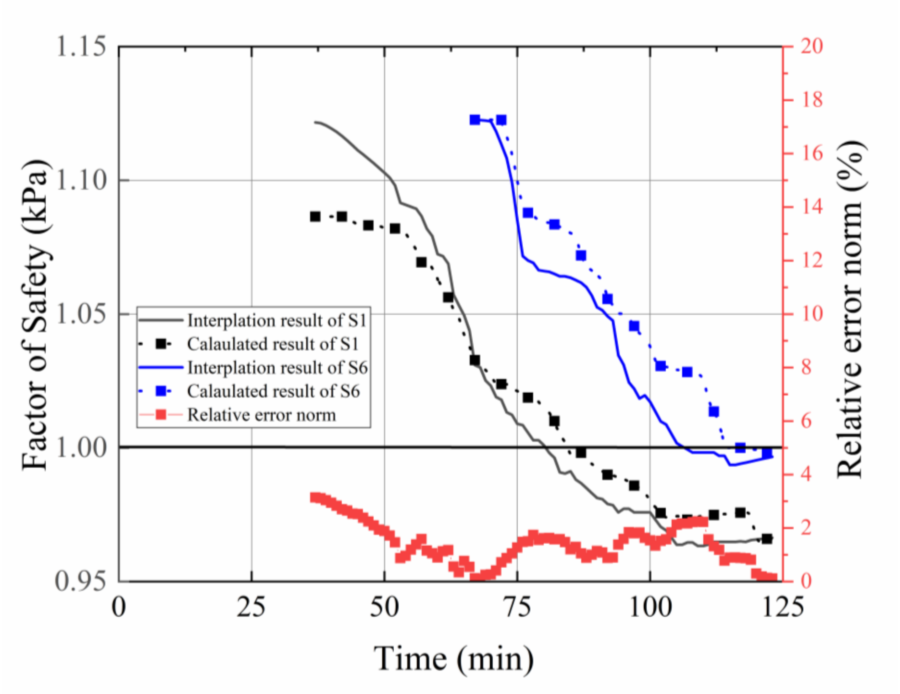

Fig 5.13 Result of cross-validation

5.3.3 Groundwater table migration by interpolation results

The previous analysis is mainly carried out on the limited experimental data monitored by sensors, but the sensor distribution is limited and cannot achieve global coverage. Therefore, it is necessary to perform interpolation analysis on monitoring blind spots. As **Fig 5.14** shows, research considers the interpolation analysis on porewater pressure. Research set the point P1 as the start point, and P3 as the end point, the distance of the interpolation range is 25cm. In this part, research choose Curved Interpolation, which has a better performance than the liner interpretation. **Fig 5.15** shows the 3D interpolation results of sensor position. The results only show the values between the interval of P1 to P3, and the values outside the interval can also be predicted through the existing interpolation results. This part of the work increases the predictability of the system.

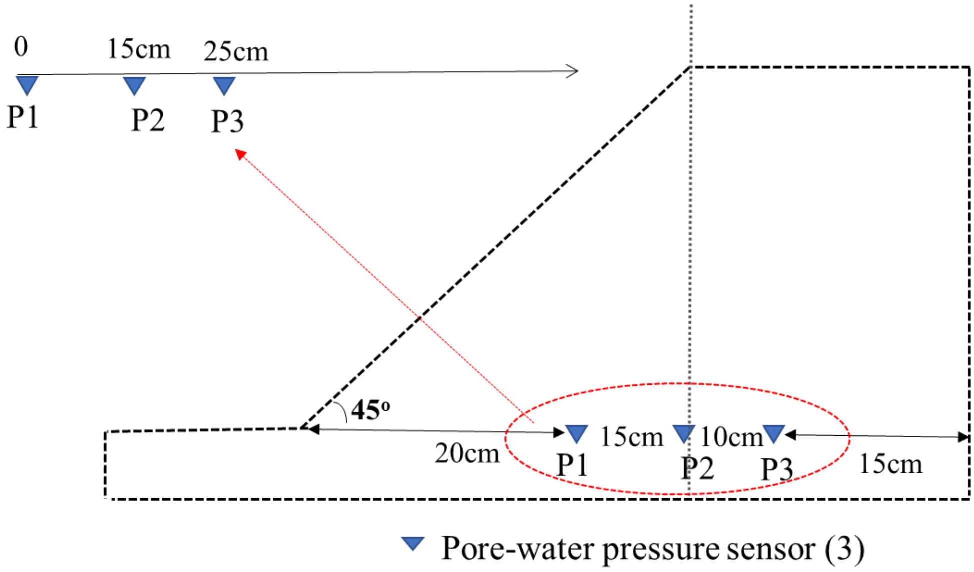

Fig 5.14 Sensor location of porewater pressure sensor

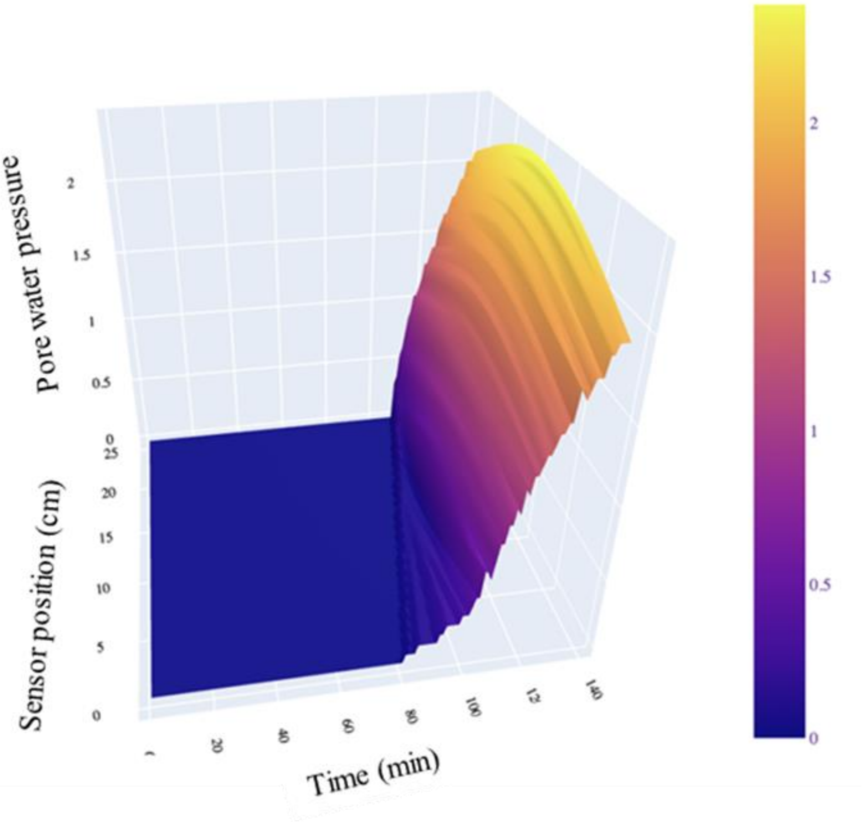

Fig 5.15 3D interpolation results of sensor position

Based on the interpolation results and analytical results mentioned in sections 3.1 and 3.2, this section discusses the migration of groundwater tables at different time duration. The progression of the groundwater table is a computed value based on the volumetric water content and pore water pressure. In addition, for each monitoring point, irrespective of the soil moisture content points or the pore water pressure points, real-time F_s analysis has been also performed. The results of typical time characteristics selected for each group of experiments are shown in **Fig 5.16** to **Fig 5.18**, the soil below the water table is in a saturated state. **Fig 5.18** also shows a schematic diagram of the first shallow landslide and the last deep landslide. Research found that when the slope is failure under bigger rainfall intensity, the elevation of the groundwater table sometimes is even lower than that at smaller rainfall intensity, which leads to a relatively higher safety factor. For example, for monitoring point S2, when the first landslide occurs, the pore water pressure is 2.29 kPa, 2.25 kPa, and 2.21 kPa respectively, while the corresponding safety factor is 0.967, 0.969, and 0.978. From the observations, it can be ascertained that this phenomenon is due to the higher impact of heavy rainfall on the slope surface which makes the condition more convenient for slope erosion, resulting in the triggering of landslides in a shorter time period. Another observation is that, all the shallow slip surfaces are located below the groundwater level, which also confirms that the groundwater level has a very significant triggering effect on shallow landslides. And larger rainfall intensities also produce significantly larger landslide volumes than low intensities.

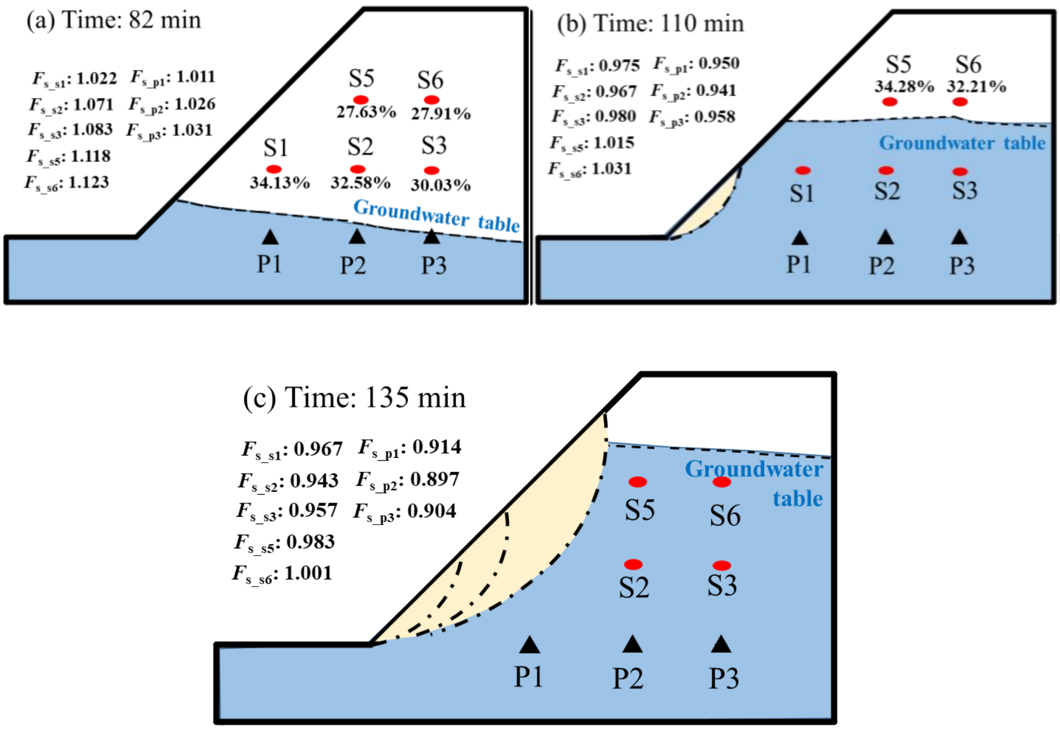

Fig 5.16 Moisture distribution and groundwater immigration of Test A：(a) 82min; (b) 110min; and (c) 135 min

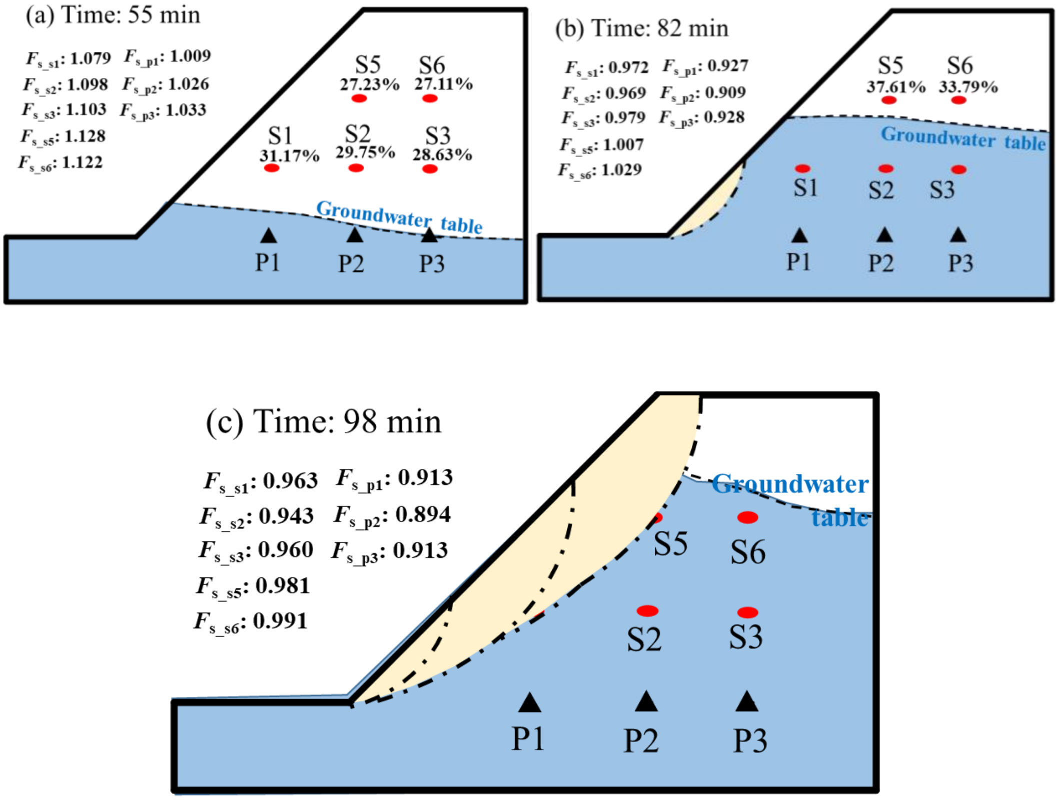

Fig 5.17 Moisture distribution and groundwater immigration of Test B: (a) 55min; (b) 82min; and (c) 98 min

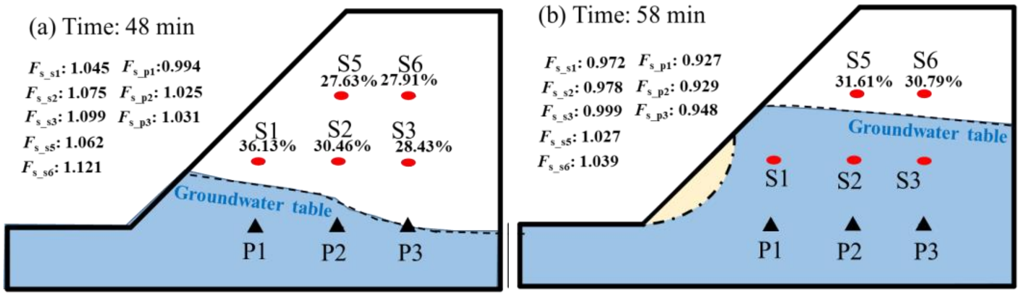

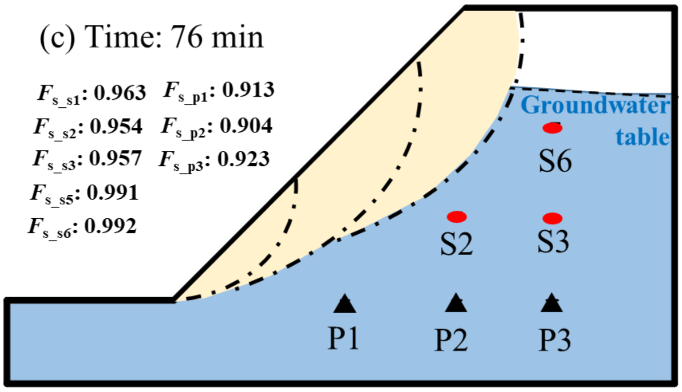

Fig 5.18 Moisture distribution and groundwater immigration of Test C：(a) 48min; (b) 58 min; and (c) 76 min

Fig 5.19 and **Fig 5.20** show the moisture distribution and groundwater immigration of Test D and Test E.

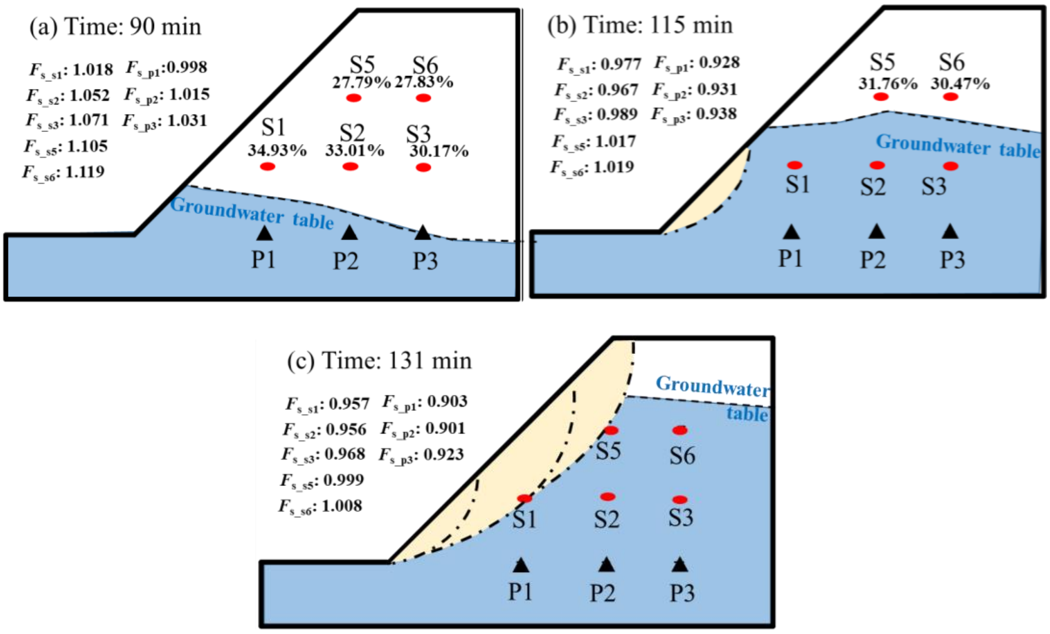

Fig 5.19 Moisture distribution and groundwater immigration of Test D：(a) 90 min; (b) 115 min; and (c) 131 min

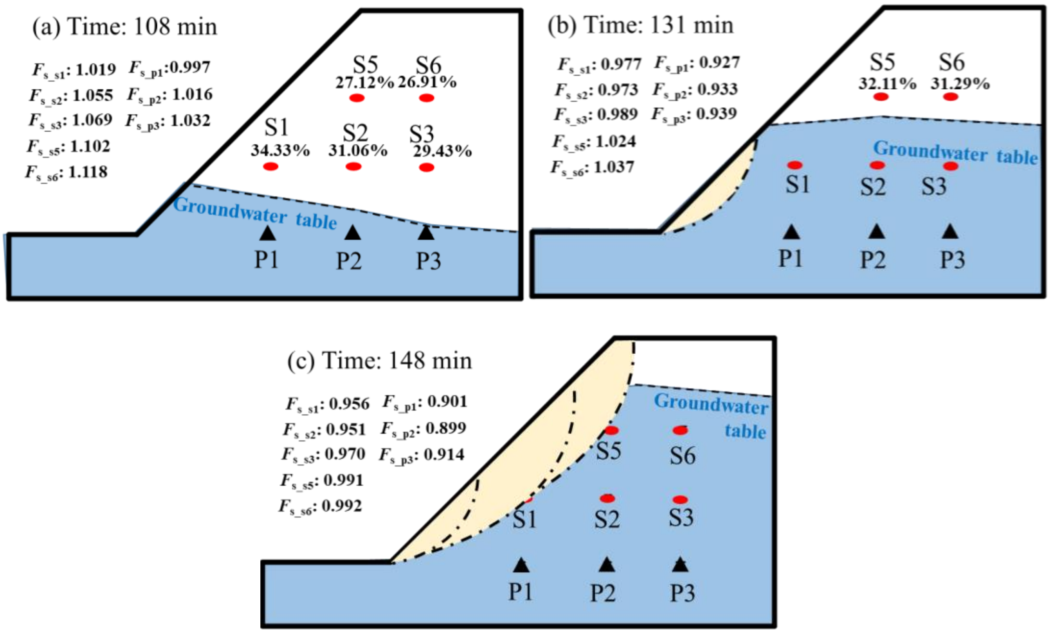

Fig 5.20 Moisture distribution and groundwater immigration of Test E：(a) 108 min; (b) 131 min; and (c) 148 min

5.4 Conclusion of this chapter

In this chapter, research used computer version-based image analysis to present the various precursor phenomena of slope failure. In addition, interpolation analysis was also carried out to provide global parameter distribution characteristics of slope under different rainfall intensities. The main conclusions are as follows:

(1) The time that motion analysis captures the extremely small displacement can be considered as the occurrence time of the landslide, which is much more accurate than observations. The various precursor phenomena of slope failure from motion analysis, such as sliding velocity, displacement and sliding volume, can provide the potential motion trajectory, movement characteristics and disaster range when a real landslide occurs. Motion analysis can be used as an alternate method to validate the prediction model of our EWS.

(2) 3D results from interpolation analysis can effectively predict the

intermediate data for training the EWS model for a wide range of meteorological conditions and monitoring areas. Additional validation experiments show that the relative error norm for a single rainfall condition is less than 20%, and for the calculated Fs is less than 5%. The accurate interpolation results can assist EWS in providing potential risk levels for wider ranges and more rainfall conditions..

Reference:

Brückl, E., Brunner, F. K., Lang, E., Mertl, S., Müller, M., & Stary, U. (2013). The Gradenbach Observatory—monitoring deep-seated gravitational slope deformation by geodetic, hydrological, and seismological methods. *Landslides*, *10*(6), 815-829.

Chueasamat, A., Hori, T., Saito, H., Sato, T., & Kohgo, Y. (2018). Experimental tests of slope failure due to rainfalls using 1g physical slope models. *Soils and Foundations*, *58*(2), 290-305.

Corsini, A., Pasuto, A., Soldati, M., & Zannoni, A. (2005). Field monitoring of the Corvara landslide (Dolomites, Italy) and its relevance for hazard assessment. *Geomorphology*, *66*(1-4), 149-165.

Dunnicliff, J. (1993). *Geotechnical instrumentation for monitoring field performance*. John Wiley & Sons.

Hogben, L. (Ed.). (2006). Handbook of linear algebra. CRC press.

Khuc, T., & Catbas, F. N. (2017). Computer vision-based displacement and vibration monitoring without using physical target on structures. *Structure and Infrastructure Engineering*, *13*(4), 505-516.

Lee, J. J., & Shinozuka, M. (2006). A vision-based system for remote sensing of bridge displacement. *Ndt & E International*, *39*(5), 425-431.

Lin, W., Shunsaku, N., Ichiro, S., Taro, U., Ikuo, T., & Jianping, Q. (2015). Case histories of slope failure and landslide disaster prevention by using a low cost tilt sensor monitoring system. In *Engineering Geology for Society and Territory-Volume 2* (pp. 631-635). Springer, Cham.

Malet, J. P., Maquaire, O., & Calais, E. (2002). The use of Global Positioning System techniques for the continuous monitoring of landslides: application to the Super-Sauze earthflow (Alpes-de-Haute-Provence, France). *Geomorphology*, *43*(1-2), 33-54.

Meng, D., & Ansari, F. (2013). Damped fiber optic low-frequency tiltmeter for real-time monitoring of structural displacements. *Measurement Science and Technology*, *24*(12), 125106.

MIURA, S., YAMAMOTO, T., KURONUMA, I., & IMAI, M. (2005). Vision metrology applied for configuration and displacement. *International Journal of the JCRM*, *1*(1), 1-6.

Saada, A. S., Liang, L., Figueroa, J. L., & Cope, C. T. (1999). Bifurcation and shear band propagation in sands. *Geotechnique*, *49*(3), 367-385.

Stanier, S. A., Blaber, J., Take, W. A., & White, D. J. (2016). Improved image-based deformation measurement for geotechnical applications. Canadian Geotechnical Journal, 53(5), 727-739.

Stark, N., McNinch, J., Wadman, H., Graber, H. C., Albatal, A., & Mallas, P. A. (2017). Friction angles at sandy beaches from remote imagery. *Géotechnique Letters*, *7*(4), 292-297.

Su, M. B., Chen, I. H., & Liao, C. H. (2009). Using TDR cables and GPS for landslide monitoring in high mountain area. *Journal of geotechnical and geoenvironmental engineering*, *135*(8), 1113-1121.

Tao, S., Uchimura, T., Fukuhara, M., Tang, J., Chen, Y., & Huang, D. (2019). Evaluation of soil moisture and shear deformation based on compression wave velocities in a shallow slope surface layer. *Sensors*, *19*(15), 3406.

Uchimura, T., Towhata, I., Lan Anh, T. T., Fukuda, J., Bautista, C. J., Wang, L., ... & Sakai, N. (2010). Simple monitoring method for precaution of landslides watching tilting and water contents on slopes surface. Landslides, 7(3), 351-357.

V Ramesh, M., & Vasudevan, N. (2012). The deployment of deep-earth sensor probes for landslide detection. *Landslides*, *9*(4), 457-474.

Xie J., Uchimura T., Chen P., (2019). A relationship between displacement and tilting angle of the slope surface in shallow landslides. *Landslides*, 16(6): 1243-1251.

CHAPTER 6

6. CONCLUSIONS AND FUTURE SCOPE

6.1 Conclusion of this study

The application of the Landslide Early Warning System (EWS) based on real-time rainfall data and geotechnical parameters of slopes is considered to be a practical approach to mitigate rainfall-induced landslide disasters. This study develops a low-cost and sustainable EWS that integrates the Internet of Things (IoT) and an off-the-grid solar energy-powered integrated sensor platform for data collection, monitoring, analysis, and alerting. A series of model tests performed on slopes allow us to identify the risk levels, send warning signals, and predict potential movement to issue alerts at an early stage with sufficient time for people to escape in the vicinity of danger zones and isolate the area.

The objective of this study is: (1) to reveal the failure mechanism and stability analysis of the slope under rainfall conditions; (2) to develop low-cost and sustainable early warning systems that can meet different geological conditions and network communication status; (3) to propose an effective evaluation index among various precursory phenomena of the landslide; (4) to introduce the application of EWS to the actual engineering projects, which can ensure the safety of the public as well as contribute greatly to disaster prevention, thereby protecting the lives and properties; (5) to present how IoT-based EWS can forge new paths for interdisciplinary study and generate a positive impact on SDGs.

Based on the experiment method, analytical calculation method, and software method, the main contributions of this study can be obtained as:

(1) By analytical calculation method for natural unsaturated slope with shallow failure mode under rainfall infiltration, factor of safety $\boldsymbol{F}_\mathbf{s}$ below the groundwater table decreases rapidly due to the influence of pore water pressure. The maximum value of the $\boldsymbol{F}_\mathbf{s}$ appears at a distance of 0.5-1.5m above the groundwater table, then a longer distance leads to a reduction of the factor of safety and eventually tends to a stable state. The maximum $\boldsymbol{F}_\mathbf{s}$ of fine sand is increased by about 20% compared with coarse sand and around 10% compared with medium sand in the unsaturated area.

(2) By analytical calculation method for natural unsaturated slope with deep failure mode under rainfall infiltration, clay presents the lowest $\boldsymbol{F}_\mathbf{s}$, while Loess and Silt show better stability. A larger internal friction angle will increase the stability of the slope, while a higher slope angle will lead to a lower $\boldsymbol{F}_\mathbf{s}$. In the initial stage, the $\boldsymbol{F}_\mathbf{s}$ gradually decreases from evaporation, no-flow to infiltration. However, with the continuous increase of rainfall infiltration, the influence of different infiltration states on $\boldsymbol{F}_\mathbf{s}$ gradually disappears.

(3) This study introduces IoT-based EWS with advantages of low-cost and low power consumption. In addition, This system can accommodate and be compatible with any sensor with an I2C output, thereby making it possible to be upgraded at any point of time for different application scenarios and monitoring requirements.

(4) This newly developed EWS can monitor the soil moisture content and pore water pressure, track the ground deformation and provide real-time F_s during the rainfall. The application of IoT and solar battery systems enables the proposed EWS to operate cost-effectively and sustainably.

(5) In terms of the experimental methods, under rainfall conditions, the sandy

slope model goes through five stages: the volumetric moisture content increases, the groundwater table rises, the slope gradually saturates, $F_s \leq 1.00$, and the landslide occurs. The sequence of these five stages can be used as an important reference for the landslide prediction model. According to the important monitoring indicators and F_s calculated in real-time, the whole early warning process is divided into three stages: Monitoring State, Alert State and Triggering State. In this study, factor of safety F_s, which is lower than the actual situation is used for risk assessment and landslide prediction. Research found that F_s has been significantly reduced under continuous rainfall, and it will drop below 1.00 just before the landslide.

(6) This system presents accurate predictions and three warning times are all before the occurrence of the landslide. The model test based on EWS can provide the distribution characteristics of rainwater, the evolution trend of the groundwater table, which verifies the feasibility of the EWS.

(7) 3D result from interpolation analysis effectively solves the limitations of the experimental method and expands the limited data to the global. Additional experiments are used for validation and cross-validation based on interpolation calculations to confirm the feasibility of the method. Result shows that the relative error norm for a single rainfall condition is less than 20%, and for the calculated Fs is less than 5%.

(8) In terms of software methods, The time that motion analysis captures the extremely small displacement of the slope can be considered as the occurrence time of the landslide, which is much more accurate than observations. The sliding velocity, displacement and sliding volume from motion analysis can provide the potential motion trajectory, movement characteristics and disaster range when a real landslide occurs. Motion analysis can be used as an alternate method to validate the prediction model of our EWS.

6.2 Future scope of this study

6.2.1 Application of LPWA

Low-power Wide-area (LPWA) is a wide approach for IoT devices communication at present. As introduced above, the current LPWA has a lot of standards, like LoRa, LoRaWAN and Sigfox. Since this research focus on the most cost-effective and susitainable method to to complete specialized communications infrastructure suitable for disaster prevention work, LoRa technology was used in this study. Communication devices was chosen by LoRa-modulated solutions to design and implement protocols to control related systems to provide timely and effective communications during disasters. The connection of LPWA has shown as below:

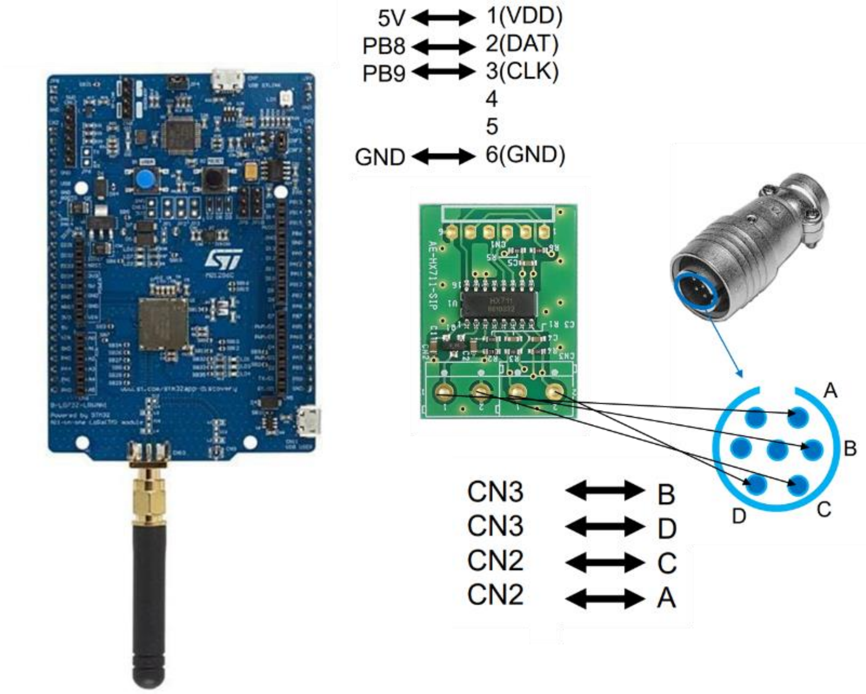

Fig 6.1 Diagram sensor conection by LoRa

Based on the analysis above, the advantages and disadvantages of the two transmission methods are shown in **Table 6.1.** It can be found that the biggest difference lies in the communication method. The WIFI system is more expensive, but it has faster transmission; although the LPWA system reduces the cost, the data transmission volume is very low and it can only support little amount of data transfer (15 bytes every time).

As a result, an EWS conbines both the two EWS could be much more effectively, that is That is to use LPWA in the data acquisition layer, but to set up a wifi system within its transmission data range (5KM), only one system can meet the conditions. In this way, the data can be effectively transmitted to the terminal, and it is also convenient for remote practice monitoring.

Table 6.1 Comparison of two EWS

	EWS with WIFI system	EWS with LPWA
Advantages	1. Remote data transferring, real-time data checking. 2. Communication speed is faster. 3. Large amount of data transfer.	1. Avoid network usage. 2. Less power consumption. 3. Long communication distance.
Disadvantages	1. Need stable network signal (Network Station). 2. Need to apply for Sim card. 3. High cost.	1. Little amount of data transfer (15 bytes every time) 2. Low speed of data

6.2.2 DNN-FL-IoT based EWS

Although the development, validation, and deploymet of early warning systems have been described in detail. Moreover, with the development of advanced sensor technology and a large number of landslides, monitoring data are becoming more extensive and comprehensive. Therefore, the development of a new integrated data-driven real-time monitoring and early warning system to deal with "instantaneous data" is crucial.

Most of the current landslide early warning models use rainfall duration and intensity as a parameter for triggering of the landslide, however it may provide false alarms as the site geology significantly influences the triggering time under various rainfall conditions. Furthermore, many systems currently installed around the world use high-precision professional equipment to provide more accurate data, but this makes it more complex and non-sustainable in terms of cost and it requires continuous monitoring by experts. Moreover, the transmission of data from the sensors through Wi-Fi or cellular network is not feasible in most of the remote mountainous regions around the world. In addition to it, analysis of accumulated data from the sensor network will create computational burden and load the network with unnecessary data at the fusion center or the cloud server.

In the following part, research will propose a low-cost, adaptable and dispersed landslide early warning system based on an Edge AI-Federated Learning (FL)-Internet of Things (IoT) architecture. First of all, the data received from the sensors will be transmitted to the Edge server with the help of a LoRa module which uses low-power wide-area (LPWA) network modulation technique. The grid of LoRa modules eliminates the need for costly, power intensive data loggers but also transmit the data in real time without any requirement of internet or cellular network. At each edge server, a Deep Neural Network (DNN) will be constructed using the data available at that edge device. The DNN will also filter and preprocess the data before training it for time series forecasting. The edge servers in the system will exchange the DNN model with each other, instead of exchanging the whole data. A Federated Learning (FL) method will be developed so that all the edge servers will come up with a common, robust model for prediction. The computation will be calculated at each edge server/device instead of sending all the data to a fusion center, which reduces the network loading and computational burden at the center when the data is collected constantly 24/7.

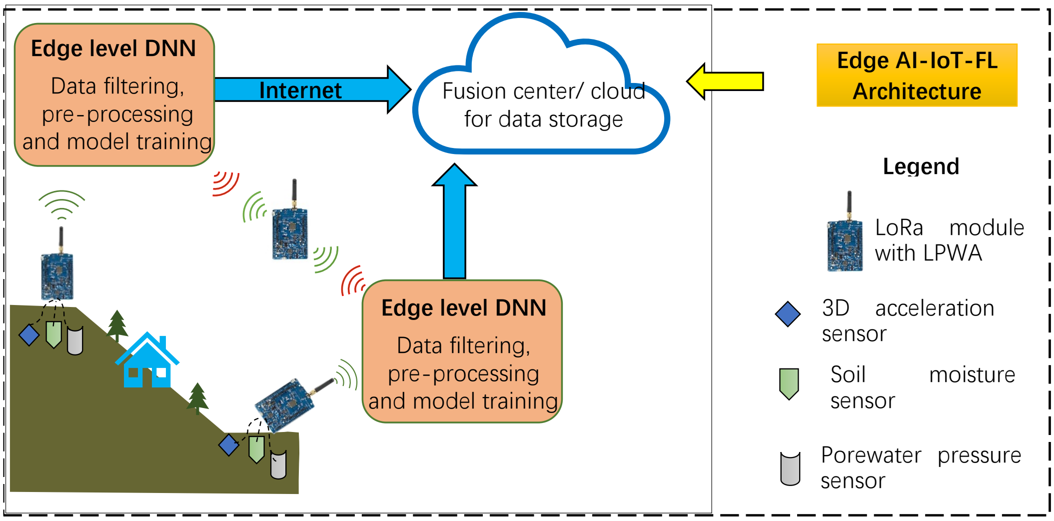

Fig 6.2 Architecture of the proposed landslide early warning system

6.2.3 More development functions and applicable scenarios

In the future, research will consider strain gauges, water table sensor, and rain gauges to add more function of the EWS.

In addition, different geology condition such as slope with crack, slope with different soil layers will also be considered to deploy EWS.

Appendix

A.1 Site geological investigation in Chikushino, Fukuoka

The survey project is being constructed in Chikushino City, Fukuoka Prefecture. **Fig A.1** shows the diagram of the cutting and embankment. The facility will have two modern warehouses. The construction work started in the year 2012. The construction area was hills originally, the construction site was prepared by a cutting and filling approach. The hills were excavated and cut to the desired elevation, while the valley part was filled with the cut material. The filling part of the site consists of an embankment whose depth varies from 5 m to 33 m. It was observed that the road constructed on the embankment towards the deeper side of the embankment experienced cracks and differential settlement.

On a detailed evaluation of the design, it was found that the length of geotextile provided for reinforcement in the deeper side of the embankment was not long enough to cover the slip surface of the embankment slope. This caused crack formation in the road, above the location where the length of geotextile is coming to be short as per the required design specifications. The consultant has therefore decided to excavate the affected area and place high-strength geogrid in the soil for reinforcement and further settlement mitigation.

Currently, the settlement of the ground is being monitored by an automated total station which monitors the change ground elevation at various locations in the site at specific time intervals from a reference point. Furthermore, boreholes are dug and sensors like strain gauge, groundwater level transducer as well as inflatable pressure meter are placed at various locations to monitor the underground soil conditions.

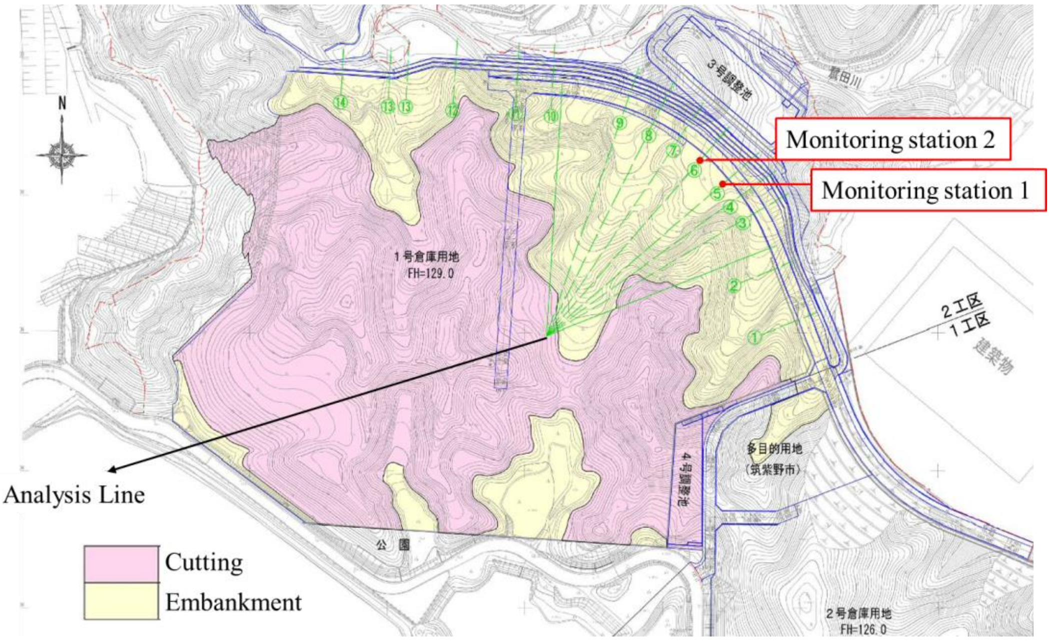

Fig A.1 Digram of Cutting and Embankment

There are already 2 boreholes in the site with a standard penetration test to check the soil properties and compaction of the embankment. Result in **Fig A.2** show the borehole survey and standard penettarion test. It can be found that from 0-13m or 14 m in the monitoring areas, the soil layers mainly contain layers of sandy and clayey soil, resulting in a loose state of the embankment. The average *N*-value of Boring No.1 from 0-14 m is 6, and *N*-value of Boring No.2 from 0-13 m is 9. While the average *N*-value of Boring No.1 from 14-33 m is 13, and *N*-value of Boring No.2 from 13-31 m is 13 as well, both of which are in medium state. The maximum *N*-value for Boring No.1 and Boring No.2 is 40 and 35 respectively, both are in a dense state. Through the test of PDCPT, the research carried out soil sample collection, and focus on the properties of soil layers.

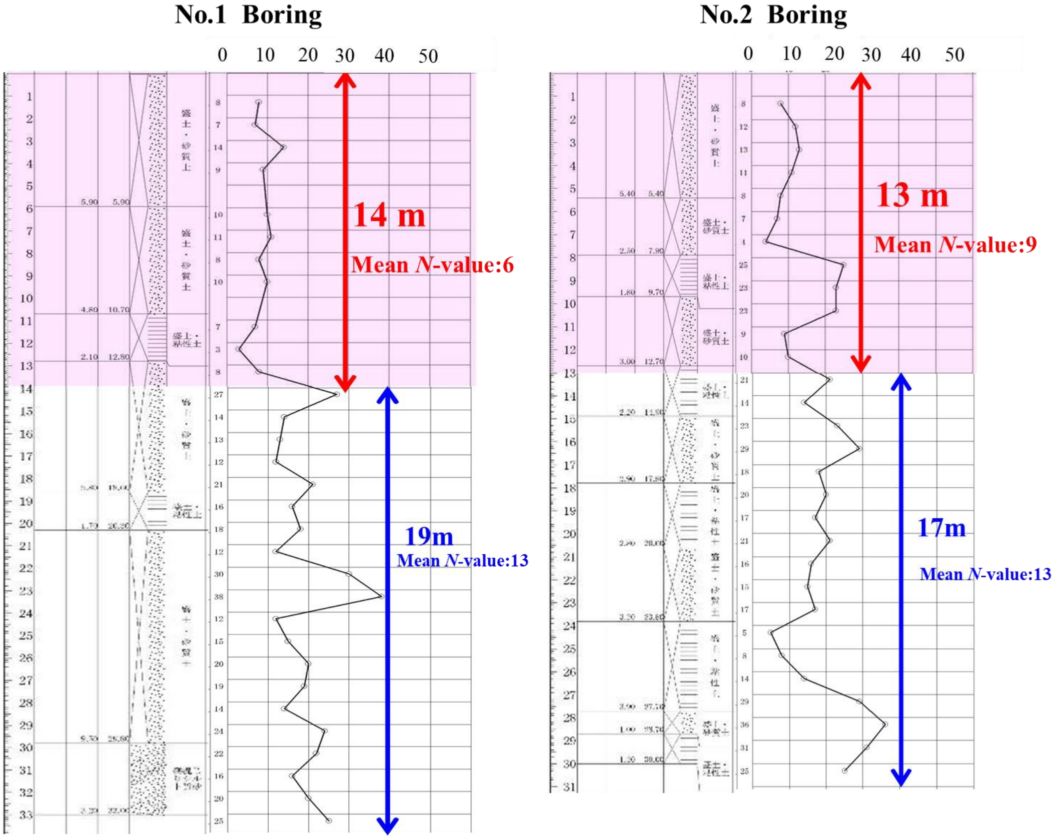

Fig A.2 Results of Standard Penetration Testing

In order to determine the physical properties and soil strength of the embankment material. Research conducted a lot of laboratory tests on the soil sample collection from Boring 1, and the first collection was carried out at 4.50-5.50 m below the ground surface, and the secondary collection was carried out at 9.50-10.50 m under the ground surface. **Fig A.3** shows the grain-size curve of the soil at the monitoring site. It is obvious that the particle size distributions of the soil under two different depths are quite similar. **Table A.1** presents the results of the laboratory soil tests, typical parameters such as density, specific gravity, void ratio as well as strength parameters cohesion c and internal friction angle φ are all shown in the table. Due to the soil layer information, particle size characteristics and soil parameters in the tests, this research can give some reference to the sensors deployment work and the determination of the threshold value in the EWS, so as to carry out effective early warning work. Similarly, the strength parameters *c* and *φ* of the soil can be used as an important reference when calculating the factor of safety F_s.

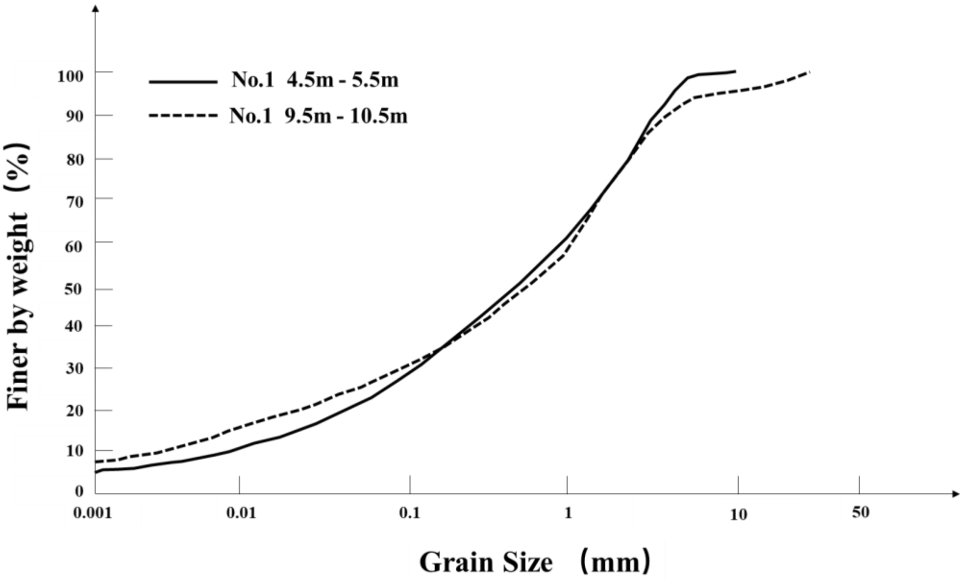

Fig A.3 Grain size curve of the soil

Table A.1 Results of laboratory soil test

Test No.	No.1 4.5m-5.5m	No.1 9.5m-10.5m
Wet density (g/cm^3)	1.957	1.774
Dry density (g/cm^3)	1.618	1.338
Specific Gravity G_s	2.676	2.641
Void ratio *e*	0.655	0.974
Saturation (%)	85.6	88.4
D_{50} (mm)	0.43	0.52
D_{10} (mm)	0.0072	0.0027
c (kN/m^2)	10.8	12.65
φ (°)	37.62	32.07

A.2 EWS deployment in Chikushino, Fukuoka

Since there are already two large-scale monitoring stations on-site, the monitoring results show that the obvious rise of the groundwater table and the deflection or deformation of the soil have not been detected for several months. Therefore, this study only considers the middle area of the two sites, **Fig A.4** shows EWS deployment in Chikushino. The purpose of putting the newly developed EWS in this area is to compare with the data of the existing monitoring sites and lay a solid foundation for the large-scale deployment in dangerous areas in the future.

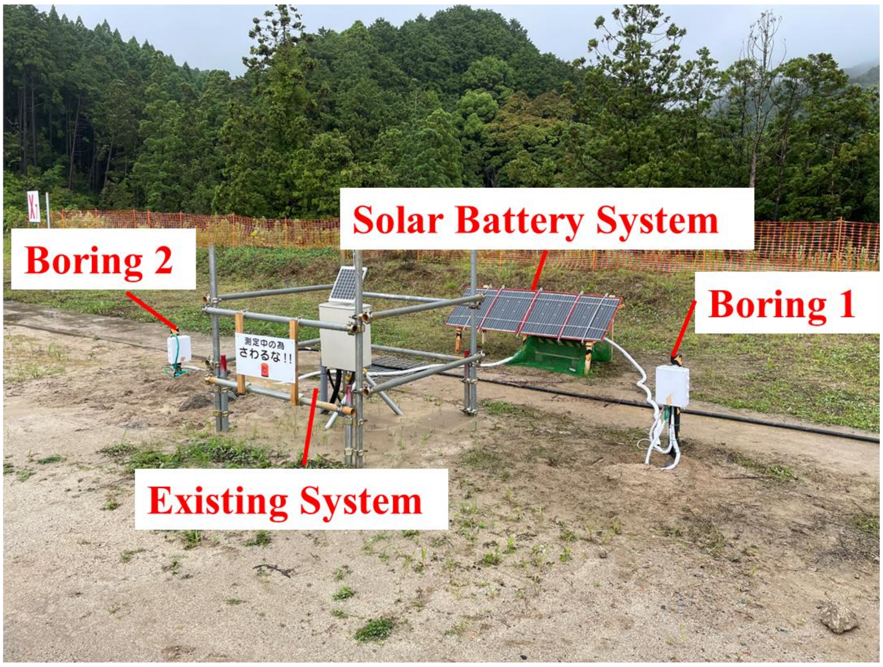

Fig A.4 EWS deployment in Chikushino

Result from the existing monitoring station shows that the groundwater table is around 15 meters below the ground surface, and there is no significant change within half a month of monitoring. For ground motion monitoring, as **Fig A.5** shows, the existing system installed a deformation sensor every one meter below the ground, accumulating more than 30 sensors per borehole. But there was also no movement was captured during the monitoring period. Due to low pore water pressure fluctuations in the monitoring, and the bottom of the whole embankment is compacted, which is more stable than the upper part. In order to reduce costs and make it easy to deploy, this study only considers the most vulnerable area with a depth of 2 meters under the ground surface and the current scheme does not deploy any pore water pressure sensors. The profile of the EWS deployment is shown in **Fig A.5**, and the middle part is the newly developed EWS. It can be found that every 0.25 meters, we set a soil moisture sensor and every 0.75 meters we set a 3D acceleration sensor. So there will be six soil moisture sensors and two 3D acceleration sensors totally in the design borehole, and one solar battery system with 200 Wh is enough for the whole operation.

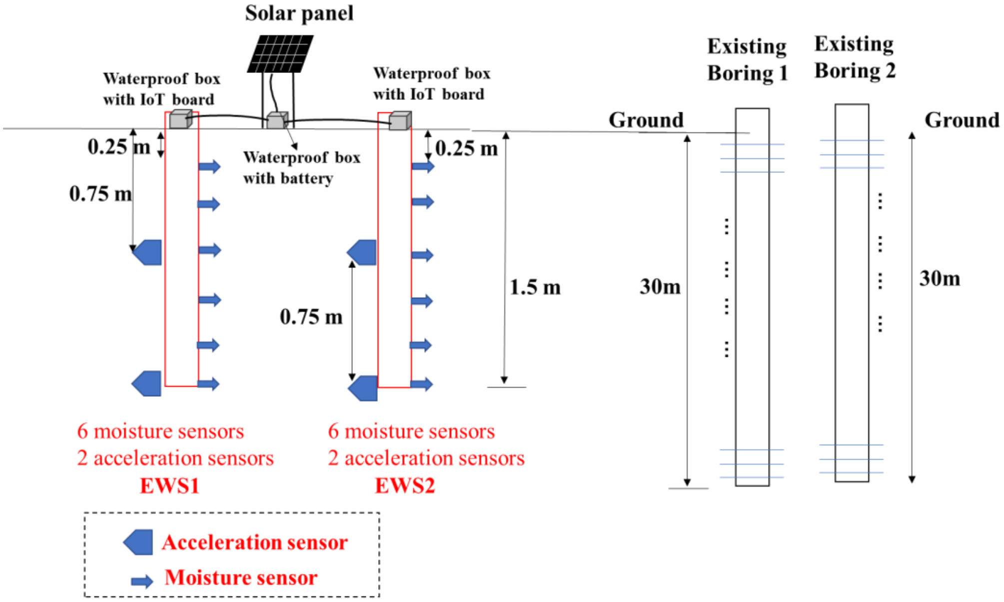

Fig A.5 Profile of the EWS deployment

It has been monitoring for two weeks, the moisture sensor data shows that the soil moisture content has decreased, it's easy to understand, because there is no heavy rainfall during these days, and the data of the acceleration sensor presents that a certain deflection angle is generated, but the difference is less than 1 degree than the data one week before, so the deformation is around 0.1 degree per day, which is a reasonable range. As a result, now the monitoring area is in a safe state.